Space Weather at Mars: 3-D studies using one-way coupling between the Multi-fluid MHD, M-GITM and M-AMPS models

by

Chuanfei Dong

A dissertation submitted in partial fulfillment
of the requirements for the degree of
Doctor of Philosophy
(Atmospheric, Oceanic and Space Sciences and Scientific Computing)
in The University of Michigan
2015

Doctoral Committee:

Research Professor Stephen W. Bougher, Chair
Professor Michael W. Liemohn
Associate Research Geophysicist Yingjuan Ma
Professor Kenneth Powell
Research Professor Gábor Tóth

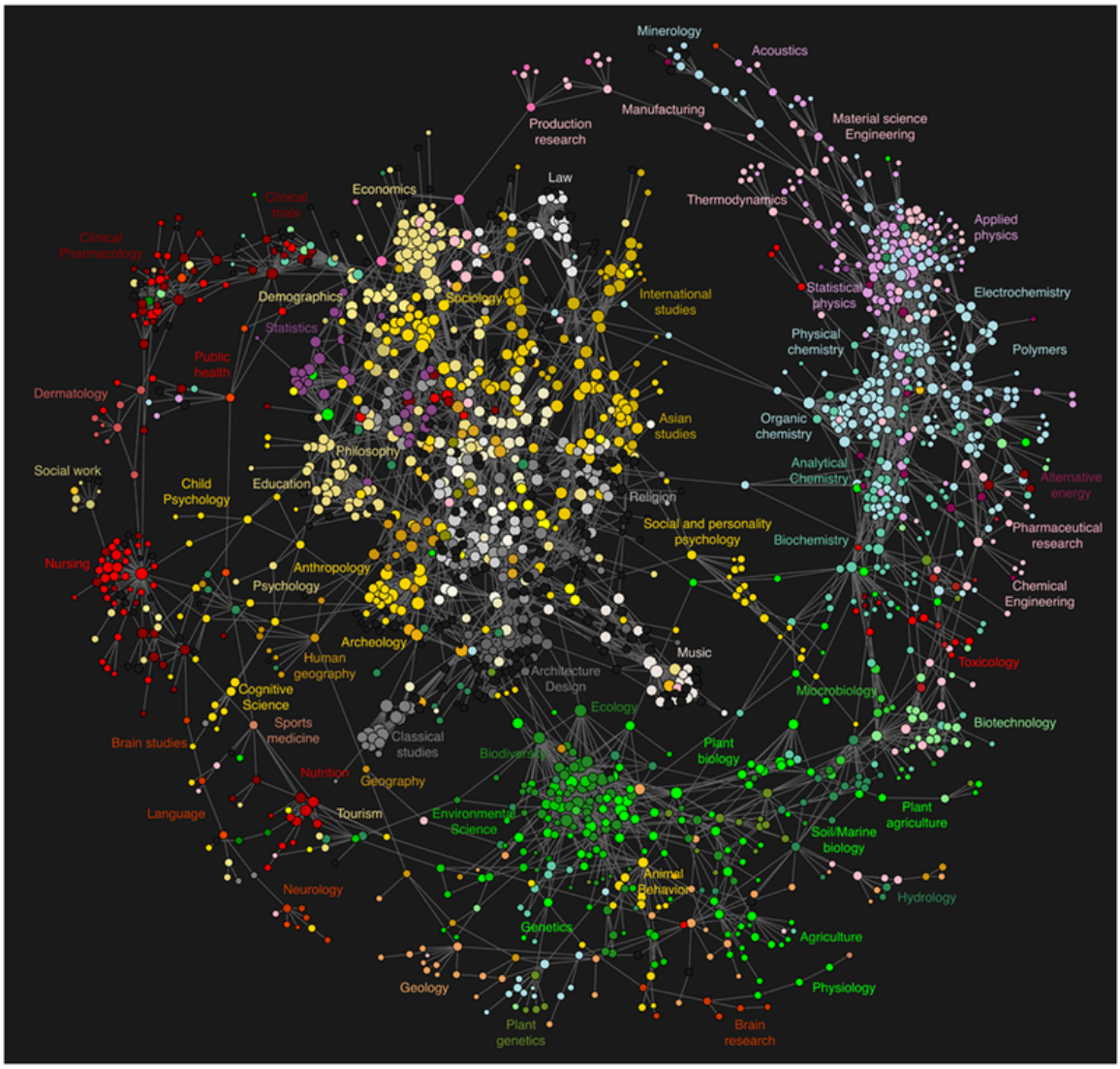

Map of Science (*Bollen et al.*, 2009).

To my dear grandmother, parents, sisters and significant other, for their love, support and guidance

ACKNOWLEDGEMENTS

First and foremost I must thank my Ph.D. advisor, Dr. Stephen Bougher, who brought me to the field of space and planetary sciences, and offered me the great opportunity to become an official team member of the MAVEN mission. Without him, none of this would have been possible. Before I was introduced to this research area, I always dreamed to be a theoretical physicist in the field of string theory. It was his guidance, support, advice, wisdom, patience, and mentorship that has made me grow into a planetary scientist that I am today and given me the tools to succeed in the future. I would certainly not be where I am without him and for that I am forever grateful. Next, I would like to thank Dr. Gábor Tóth, who greatly helped me on a lot of numerical issues I had during my research. Besides, it is his mentoring and encouragement that helped me become more and more familiar with coding and debugging in a huge code like BATS-R-US. He taught me numerous things that "you cannot find in textbooks". I would also like to thank Dr. Yingjuan Ma for her great patience in teaching me all the details of the Mars component of the BATS-R-US that she developed during her Ph.D. research. I would like to thank my other committee members: Dr. Michael Liemohn for his valuable advice and encouragement throughout my Ph.D. work and Dr. Kenneth Powell, for his gracious acceptance to be one of my dissertation committee members.

In addition, I would like to thank Dr. Andrew Nagy who has encyclopedic knowledge of planetary sciences. I knock on his door all the time when I have questions that I cannot find answers from books. He can always give me a quick answer from

his breadth of knowledge. Even if he could not answer my questions immediately, he would give me one of the books and tell me which chapters I should read. Besides, I would like to specially thank Dr. Valeriy Tenishev for teaching me how to use SPICE in C language. He also spent a lot of time teaching me how to write a DSMC code with greatly detailed techniques developed by himself. I would like to thank Dr. Bart van der Holst. He helps me on understanding the BATS-R-US code in depth, which is essential for me to implement the thermal conduction in the electron pressure equation. Moreover, I would like to thank Dr. Jim Slavin. It is his expertise in magnetospheric physics that helps his students have an enjoyable and wonderful class on this topic. I appreciate the valuable discussions with him after each class, from which I built a solid background in planetary magnetospheres.

Besides, I would like to thank Dr. Y.Y. Lau at the Nuclear Engineering department, who passed almost all of his knowledge in plasma physics onto me by answering my numerous questions after each class. Without him, I would not have a solid background in plasma physics as today. Furthermore, I would like to thank my LANL mentor Dr. Dan Winske, the master of hybrid codes, for teaching me all his knowledge on the hybrid simulation technique and the shock physics in the summer of 2013. Here I also must thank my previous advisor at Georgia Tech Dr. Carol Paty, who enrolled me in her program regardless of my poor English six years ago. Her great patience helped me to improve my English step by step. Meanwhile, I also learned a lot of magnetospheric physics and MHD basics from her, which increased the diversity of my learning sources. I appreciate insightful discussions on the theory of plasma kinetic instabilities with Dr. Xiangrong Fu, Dr. Misa Cowee and Dr. Peter Gary when I was at LANL. I also appreciate the useful discussions on the particle in cell (PIC) simulation method with Dr. Alexander Thomas (UM), Dr. Nagendra Singh (UAH), Dr. Igor Sokolov (UM), and Dr. Ouliang Chang (USC).

I would like to thank my friends, Dr. Zhenguang Huang, Dr. Meng Jin, Dr. Xing

Meng, and Yuxi Chen who helped me so much with my research (such as, how to use idl and Tecplot, how to write a shell script). Without their help, I would not make such great progress on my research. I also would like to thank Dr. Dan Welling for introducing me the Python programming language.

I would like to thank all my friends and teachers, Dmitry Borovikov, Dr. Iain Boyd, David Chen, Dr. Shannon Curry, Dr. R. Paul Drake, Dr. Gina DiBraccio, Dr. John Foster, Dr. Lennard A Fisk, John Haiducek, Dr. Xianglei Huang, Fei He, Dr. Jiaming Yu, Dr. Karl Krushelnick, Dr. Robert Krasny, Yuni Lee, Qingli Lei, Dr. Susan Lepri, Hui Li, Yang Li, Xianjing Liu, Xiaojian Liu, Yiming Lou, Chaoyi Jiao, Blake Johnson, Dr. Roxanne Katus, Dr. William R. Martin, Jonathan Nickerson, Kirk Olsen, Dr. Rona Oran, Doğacan Öztürk, Fang Pan, Dr. Justin Perket, Dr. Aaron Ridley, Dr. Philip Roe, Lois Sarno-Smith, Yinsi Shou, Peng Tian, Dr. Wei Tian, Dr. Chunpeng Wang, Dr. Jianping Xiao, Dr. Shaosui Xu, Xun Yang, Dr. Weiye Yao, Dr. Peng Zhang, Dr. Xiangyun Zhang, Dr. Liang Zhao, and Jie Zhu (alphabetical order), with whom I had a wonderful time during my Ph.D. life at AOSS and at the University of Michigan, Ann Arbor.

I am proud to be an official MAVEN team member to be involved in the entire spacecraft mission from its launching to the scientific data return during the primary mission phase. I would like to thank all the MAVEN team members for making it happen. I would like to thank administrative staff, especially Deborah Eddy for her great help during my graduate life at AOSS. I also would like to thank all the AOSS IT group, especially Darren Britten-Bozzone for his support on my desktop software maintenance.

Finally, I would like to acknowledge my family for having done so much for me. I also want to express my deepest appreciation for the love and support, both emotional and scientific, of Dr. Nan Liu.

TABLE OF CONTENTS

DEDICATION ii

ACKNOWLEDGEMENTS iii

LIST OF FIGURES ix

LIST OF TABLES xiv

ABSTRACT xv

CHAPTER

I. Introduction 1

1.1 The Mars upper atmosphere and its interaction with the solar wind 1
1.2 The drivers controlling atmospheric escape 7
1.3 The role of global models in constraining Mars atmospheric escape 7
1.3.1 Global models and their application to characterize atmospheric escape and its variation 8
1.3.2 Previous Global Plasma Modeling Studies of Mars . 11
1.4 Observations by previous missions to Mars 12
1.5 MAVEN mission and its primary scientific goals 14
1.6 Outline of the dissertation 17

II. Mars multi-fluid MHD equations 20

2.1 Transport Equations for Multi-fluid Plasma 20
2.1.1 Generalized transport equation 21
2.1.2 Collision Terms in Transport Equations for Multi-Fluid Plasma 23
2.1.3 Summary of the Transport Equation 32
2.1.4 Multi-Fluid MHD Equations 35

III. Solar wind interaction with Mars upper atmosphere during current and ancient times: Results from the one-way coupling between the multi-fluid MHD model and the M-TGCM model 37

3.1 Introduction . . . 37
3.2 Model Description . . . 38
3.3 Simulation Results and Discussions . . . 44
3.3.1 Ion escape at the current epoch . . . 44
3.3.2 Ion escape over Mars history . . . 52
3.3.3 Discussion . . . 53
3.4 Conclusions . . . 56

IV. Solar wind interaction with the Martian upper atmosphere: variable 3-D cold neutral thermosphere and hot oxygen corona 58

4.1 Introduction . . . 58
4.2 Model Description . . . 60
4.2.1 Mars Global Ionosphere Thermosphere Model (M-GITM) . . . 62
4.2.2 Mars Adaptive Mesh Particle Simulator (M-AMPS) model . . . 63
4.2.3 BATS-R-US Mars multi-fluid MHD (MF-MHD) model 66
4.2.4 One-way Coupling Approach . . . 67
4.3 Simulation Results and Discussions . . . 69
4.4 Conclusions . . . 82

V. Solar wind interaction with the Martian upper atmosphere: Crustal field orientation, solar cycle and seasonal variations 84

5.1 Introduction . . . 84
5.2 Model Descriptions and results . . . 86
5.2.1 Mars Global Ionosphere Thermosphere Model (M-GITM) . . . 86
5.2.2 Mars Adaptive Mesh Particle Simulator (M-AMPS) model . . . 86
5.3 Simulation Results and Discussions . . . 88
5.3.1 Effects of crustal field orientation . . . 89
5.3.2 Effects of seasonal variations . . . 94
5.3.3 Effects of solar cycle conditions . . . 96
5.3.4 Effects of mass differentiation . . . 98
5.4 Conclusions . . . 104

VI. Multi-fluid MHD study of the solar wind interaction with Mars' upper atmosphere during the 2015 March 8 ICME event and the MAVEN Deep Dip campaign 106

6.1 Introduction 106
6.2 Model and inputs 108
6.3 March 8th ICME event 109
6.3.1 Data-model comparison and model validation 109
6.3.2 Ion escape plume and ion loss rate 110
6.3.3 Variation of plasma boundaries at the subsolar region 115
6.4 Data-model comparison for the second MAVEN Deep Dip campaign 118
6.5 More discussion 120
6.6 Conclusion 120

VII. Preliminary results of electron temperature calculation, summary and future work 125

7.1 Preliminary results from the multi-fluid MHD model with separated ion and electron pressure equations 125
7.2 Summary: answers to the four main scientific questions . . . 127
7.3 Future work 128

BIBLIOGRAPHY 131

LIST OF FIGURES

Figure

1.1 The remnant crustal magnetic field magnitude at an altitude of 200 km, calculated using the 60 degree harmonic expansion of *Arkani-Hamed* (2001) in the geographic (GEO) coordinate system. 2

1.2 An example of the variation with altitude of 9 atomic and molecular species during a single MAVEN deep dip pass on orbit #1064 is shown. For the trace gas He gas scattering in the instrument at the lowest altitudes may distort the profile. N, O_2, O, and NO are derived from open source (neutrals and ions) measurements and the remaining gases from closed source (non-reactive neutrals) data (*Mahaffy et al.*, 2015). 3

1.3 Illustration of the global plasma interaction between Mars and the solar wind (*Lillis et al.*, 2015). It also depicts the major boundaries and regions in the meridional plane. 5

1.4 Interaction of the solar wind with the Earth's Magnetosphere (*Wang*, 2008). 6

1.5 Schematic diagram showing the coupling approach between the different components. The black solid lines represent completed coupling, via the variables colored black. The dashed blue lines represent future coupling via the variables colored blue (Adapted from *Dong et al.*, 2015a). 10

1.6 Artist's conception of the MAVEN spacecraft. High-gain antenna in the middle is 2 m diameter for scale. Articulated Payload Platform (APP) is visible at the top; SWEA boom at bottom center; one of the LPW booms is visible at lower right. The second panel of each solar-array wing is canted for increased aerodynamic stability (*Jakosky et al.*, 2015a) 15

1.7 Instrument accommodation. Diagram shows the locations of the science instruments on the body of the spacecraft and on the APP (*Jakosky et al.*, 2015a) 16

3.1 Neutral temperature T_n, cold neutral O and CO_2 densities at altitude of 100 km for Case 1 (also Epoch 1) from M-TGCM. Note that local time LT=12 is at longitude=180 instead of longitude=0. 40

3.2 A sketch (cartoon) of a one-way coupling approach between the M-TGCM and MF-MHD models. The notation T_n denotes neutral atmosphere temperatures, N_O, N_{CO_2} are the neutral O and CO_2 number densities, and I_O, I_{CO_2} are the photoionization frequencies. 41
3.3 Illustration of the grid system used in the MF-MHD calculation in MSO coordinate system. 43
3.4 Comparison of (a) multi-species MHD and (b) multi-fluid MHD O^+ ion escape distribution in a logarithmic scale. 46
3.5 Multi-species MHD electric and magnetic fields background calculations for test particles where the magnetic field magnitude is shown by color contour, vector field of the plasma velocity is represented by white arrow, and convection electric field is displayed by black arrow in the noon-midnight plane (*Fang et al.*, 2010). 47
3.6 The calculated (Cases 1, 2, 3) ion number densities (no friction) in cm^{-3} in the $X-Z$ plane for H^+, O_2^+, O^+, and CO_2^+ in a logarithmic scale. Noted that the logarithmic scales in different plots are different. 48
3.7 The calculated (Cases 1, 2, 3) ion number densities (with friction) in cm^{-3} in the $X-Z$ plane for H^+, O_2^+, O^+, and CO_2^+ in a logarithmic scale. Noted that the logarithmic scales in different plots are different. 50
3.8 A comparison of the 3-D M-AMPS hot oxygen number density (in cm^{-3}) for Epoch 1, 2, 3. Note the use of a logarithmic scale.. 53
3.9 The calculated (Epoch 1, 2, 3) ion number densities in cm^{-3} in the $X-Z$ plane for H^+, O_2^+, O^+, and CO_2^+ in a logarithmic scale. Noted that the logarithmic scales in different plots are different. 54
4.1 A sketch of a one-way coupling approach between M-GITM, M-AMPS and the MF-MHD model (after Figure 1 of *Dong et al.* (2015a)). The notation T_n denotes neutral atmosphere temperatures. [O], [CO_2], and [O_{hot}] are the neutral O, CO_2 and hot atomic oxygen number densities, respectively. Three photoionization processes are included. Here we focus on the one-way coupling indicated by the solid black line. We also test the coupling between MF-MHD and M-AMPS illustrated by the dashed black line. For the detailed study of the one-way coupling between M-GITM and M-AMPS (solid grey line), please refer to *Lee et al.* (2015). 61
4.2 The neutral CO_2 and O number densities shown on a sphere of altitude 220 km above the Martian surface from M-GITM for autumnal equinox minimum (AEQUMIN) conditions. Two coordinate systems are displayed in the plot: the Geographic (GEO) and the Mars-centered Solar Orbital (MSO) coordinate systems. The subsolar point is highlighted in each plot. 64

4.3 A comparison of the hot oxygen number density (in cm^{-3}) distribution from a 1-D spherically symmetric model (left) (*Kim et al.*, 1998) and the M-AMPS code (right) in the x-z plane in the MSO coordinate system. The upper panels show hot O distribution for the autumnal equinox solar minimum (AEQUMIN) conditions and bottom panels illustrate the hot O distribution for the autumnal solar maximum (AEQUMAX) conditions. Note the use of a logarithmic scale. . . . 66
4.4 An illustration of coordinate transformation from GEO to MSO system for autumnal equinox minimum (AEQUMIN) conditions. The frame of axes (upper right) is shown in $y - z$ plane in MSO coordinate system. The mesh and the rotation (z) axis are shown in GEO coordinate system. The contour shows the solar zenith angle (ZSA). 69
4.5 The ionospheric ion density profiles for O^+, O_2^+, and CO_2^+ at altitude 220 km for autumnal equinox minimum (AEQUMIN) conditions with subsolar longitude equal to 270° E. 72
4.6 The ionospheric ion density profiles for O^+, O_2^+, and CO_2^+ at altitude 220 km for autumnal equinox maximum (AEQUMAX) conditions with subsolar longitude equal to 270° E. 73
4.7 The ion density comparison between the MF-MHD simulations and the Viking observations for O_2^+, CO_2^+, and O^+ ions (*Hanson et al.*, 1977). 74
4.8 A comparison of O^+ ion escape plume in the $x - z$ plane for 1-D, 3-D and no hot atomic oxygen corona. Left: AEQUMAX with 1-D spherically symmetric hot oxygen corona from *Kim et al.* (1998) (Case 7); middle: AEQUMAX with 3-D M-AMPS hot oxygen corona (Case 10); right: AEQUMAX without hot oxygen corona (Case 13). Note the use of a logarithmic scale. 75
4.9 The comparison of different hot oxygen profiles. The dotted black and dashed red curves represent the hot oxygen profile at solar zenith angle (SZA) of 60 by taking MF-MHD ionosphere (SSL=180 and 60) as M-AMPS inputs. The dash-dotted blue curves display the hot oxygen profile at SZA of 60 by taking M-GITM ionosphere (SSL=0) as M-AMPS input. The solid yellow curves show the 1-D hot oxygen model from *Kim et al.* (1998). 76
4.10 The histograms of ion escape rate (in s^{-1}). Upper panel: cases with AEQUMIN conditions; bottom panel: cases with AEQUMAX conditions. Note that the scales in vertical axes (ion escape rate) in these two plots are different. SSL stands for subsolar longitude. 81

5.1 The neutral CO_2 and O number densities shown on a sphere at an altitude of 220 km above the Martian surface from M-GITM for perihelion solar maximum (PERMAX) and aphelion solar minimum (APHMIN) conditions. Two coordinate systems are indicated in each plot: the Geographic (GEO) and the Mars-centered Solar Orbital (MSO) coordinate systems. The spheric contour plots are shown in the $x-z$ plane (not a $x-z$ cut) of both coordinates. The subsolar point is highlighted in each plot. 87
5.2 A comparison of the M-AMPS output hot oxygen number density (in cm^{-3}) distribution between autumnal equinox solar minimum (AEQUMIN, case 7) and maximum (AEQUMAX, case 10) conditions (upper panel), and aphelion solar minimum (APHMIN, case 1) and perihelion solar maximum (PERMAX, case 16) conditions (bottom panel) in the $x-z$ plane in the MSO coordinate system. All the results are based on the subsolar longitude, SSL = 0. Note the use of a logarithmic scale. 88
5.3 The histograms of ion escape rates (in s^{-1}). Upper panel: cases with solar minimum conditions; middle panel: cases with solar maximum conditions; bottom panel: average cases. Noted that the ion escape rate scales in these three plots are different. 92
5.4 The calculated ion number densities in cm^{-3} in the $x-z$ plane for H^+, O_2^+, and O^+ in a logarithmic scale. Case 1 is shown in the upper panels and case 18 is shown in the bottom panels. Noted that the logarithmic scales in different plots are different. The direction of the solar wind is parallel to the x-axis and in the $-x$ direction. 99
5.5 Least squares polynomial linear fit of the simulation results based on cases 1-18. The calculated ion escape rates associated with solar minimum and solar maximum conditions are indicated by the red circle and blue square markers, respectively. The corresponding mean values are highlighted by the green markers with the same shape. . 101
5.6 Least squares polynomial linear fit of the simulation results based on cases 1-18. The calculated ion escape rate fractions (with respect to the net ion loss) associated with solar minimum and solar maximum conditions are indicated by the red circle and blue square markers, respectively. The corresponding mean values are highlighted by the green markers with the same shape. Although the perfect linear anti-correlation in Figure 5.6 (d) is mathematically to be expected, all the linear correlations indicated in Figure 5.6 can also be physically interpreted. 102
6.1 Data-model comparison of O_2^+ ion density, solar wind density and velocity, and magnetic field using the NGIMS, SWIA, and MAG data. 111
6.2 Data-model comparison of ionospheric ion density profiles by using NGIMS ion data. Case 1: black dotted curve, Case 2: solid green curve, Case 3: dashed magenta curve, and Case 4: dash-dotted cyan curve. 112

6.3 The isosurface of O_2^+ ion density with $n_{O_2^+}$=0.005 cm^{-3}, on which the contour of O_2^+ ion speed $U_{O_2^+}$ is presented. The meshed grid is the sphere with r=6R_M used to calculate the ion escape rate. The r=6R_M sphere in each plot is also used as a reference to know the relative size of the isosurface. The red curves are the MAVEN trajectories. . 116
6.4 (left) The calculated O_2^+ ion number densities in cm^{-3} in the $x-z$ plane in a logarithmic scale (see density colorbar). The black arrow represents the O_2^+ ion velocity vector (a reference vector of 500 km/s magnitude is displayed in the upper right corner). The selected solid red and dashed blue curves in the contour plot are the $\mathbf{U}_{O_2^+}$ streamlines at dayside escape plume and nightside plasma wake region, respectively. (right) The corresponding speed (with same line style) along the streamline. 117
6.5 Left: Pressure profiles along the Mars-Sun line (see top of the plot) on the dayside for Case 1 (pre-ICME phase), Case 3 (sheath phase), and Case 4 (ejecta phase). Different curves represent different pressures: the total magnetic pressure, $P_{B(Tot)}$ (dashed red), the total thermal pressure, $P_{th(Tot)}$ (dotted blue), the solar wind dynamic pressure, $P_{dyn(SW)}$ (dashed green), the crustal magnetic pressure, $P_{B(Crustal)}$ (dashed magenta), the solar wind thermal pressure, $P_{th(SW)}$ (solid cyan), the ionospheric thermal pressure, $P_{th(Iono)}$ (solid yellow), and the total pressure, P_{total} (solid black). Right: The solar wind proton density profiles (in cm^{-3}) at altitude of 800 km for Cases 1, 3, 4. . . 119
6.6 Data-model comparison between the NGIMS data and the MF-MHD simulation for orbit 1069 on 19-April-2015. Both the inbound and outbound comparisons are displayed. 121
6.7 Data-model comparison between the NGIMS data and the MF-MHD simulation for orbit 1085 on 22-April-2015. Both the inbound and outbound comparisons are displayed. 122
7.1 The temperatures of individual ion species, total ion and electron. . 126

LIST OF TABLES

Table

1.1	Solar and heliospheric factors affecting atmospheric escape.	7
1.2	Planetary factors affecting atmospheric escape.	8
2.1	Chemical reactions and associated rates in Mars multi-fluid MHD Code (most of the reaction rates are adopted from *Najib et al.* (2011))	28
3.1	Input parameters used for the different calculations.	44
3.2	Calculated ion escape rates (in s^{-1}).	51
3.3	Calculated ion escape rates (in s^{-1}).	53
4.1	Input parameters used for the different calculations.	70
4.2	Calculated ion escape fluxes (in $\times 10^{24}$ s^{-1}).	80
5.1	Input parameters used for different calculations.	90
5.2	Calculated ion escape rates (in $\times 10^{24}$ s^{-1}).	91
5.3	Maximum ($\mathcal{R}_{max}$) and minimum ($\mathcal{R}_{min}$) ion escape rates (in $\times 10^{24}$ s^{-1}), and the corresponding ratio ($\mathcal{R}_{max}/\mathcal{R}_{min}$) for different seasons.	95
5.4	Slope and intercept of the regression line shown in Figure 5.6, correlation coefficient (r-value), coefficient of determination (r-squared, R^2), two-sided p-value for a hypothesis test whose null hypothesis is that the slope is zero, standard error of the estimate (stderr).	102
6.1	Input parameters and calculated ion escape rates for different cases (in $\times 10^{24}$ s^{-1}).	109

ABSTRACT

Space Weather at Mars: 3-D studies using one-way coupling between the Multi-fluid MHD, M-GITM and M-AMPS models

by

Chuanfei Dong

Chair: Stephen W. Bougher

This dissertation presents numerical simulation results of the solar wind interaction with the Martian upper atmosphere by using three comprehensive 3-D models: the Mars Global Ionosphere Thermosphere Model (M-GITM), the Mars exosphere Monte Carlo model Adaptive Mesh Particle Simulator (M-AMPS), and the BATS-R-US Mars multi-fluid MHD (MF-MHD) model. The coupled framework has the potential to provide improved predictions for ion escape rates for comparison with future data to be returned by the MAVEN mission (2014–2016) and thereby improve our understanding of present day escape processes. Estimates of ion escape rates over Mars history must start from properly validated models that can be extrapolated into the past. This thesis aims to build a model library for the *NASA Mars Atmosphere and Volatile EvolutioN* (MAVEN) mission, which will thus enhance the science return from the MAVEN mission.

The University of Michigan 3-D BATS-R-US multi-fluid MHD (MF-MHD) model was initially developed for Earth and later it was extended for studies of Mars. The MF-MHD model solves separate continuity, momentum and energy equations for

the four ion fluids H^+, O^+, O_2^+, CO_2^+. Unlike the Earth version, the Mars MF-MHD model contains an ionosphere, and thus the lower boundary was extended to 100 km above the Martian surface. Detailed ionospheric chemistry, such as charge exchange, photoionization and electron impact ionization, are also included. Mars has no global intrinsic dipole magnetic field; instead, it has a crustal magnetic field, which was first discovered by the Mars Global Surveyor spacecraft. The crustal fields are implemented by the 60 degree harmonic expansion, which can well describe the observed fields at Mars. A nonuniform, spherical grid structure is used in the model, where the radial resolution varies from 5 km ($\sim$ 0.5 scale height) at the lower boundary ($\sim$ 100 km) to 1000 km at the outer boundary ($\sim$ 20 R_M). M-GITM is a 3-D whole atmosphere code that captures both the Mars lower atmosphere and its thermosphere-ionosphere structure. The M-AMPS code is developed within the framework of the Direct Simulation Monte Carlo (DSMC) method, which employs a stochastic solver for both the linear and nonlinear Boltzmann equations. It can self-consistently calculate the structure of the Martian exospheric hot oxygen corona.

In this thesis, we aim to address the following four main scientific questions by adopting the one-way coupled framework developed here: (1) What are the Martian ion escape rates at the current epoch and ancient times? (2) What controls the ion escape processes at the current epoch? How are the ion escape variations connected to the solar cycle, crustal field orientation and seasonal variations? (3) How do the variable 3-D cold neutral thermosphere and hot oxygen corona affect the solar wind-Mars interaction? (4) How does the Martian atmosphere respond to extreme variations (e.g., ICMEs) in the solar wind and its interplanetary environment?

These questions are closely related to the primary scientific goals of NASA's MAVEN mission and European Space Agency's Mars Express (MEX) mission. We reasonably answer all these four questions at the end of this thesis by employing the one-way coupled framework and comparing the simulation results with both MEX

and MAVEN observational data.

CHAPTER I

Introduction

1.1 The Mars upper atmosphere and its interaction with the solar wind

The Sun has a powerful influence on planetary atmospheres. This is especially true for planets lacking a global intrinsic magnetic field, because the solar wind can interact directly with the upper atmosphere. Mars has no global intrinsic dipole magnetic field; instead, it has a crustal magnetic field, which was first discovered by the Mars Global Surveyor spacecraft (MGS) (*Acuña et al.*, 1999). The crustal fields, B_c, are distributed on the surface of the planet in a very inhomogeneous manner (e.g., see Figure 1.1), which play an important role in the process of solar wind-Mars interaction. The strongest crustal sources are located at latitudes poleward of 30° S with longitudes between 120°-210° W (*Acuña et al.*, 1999).

The bulk atmosphere of Mars is primarily CO_2, with small amounts of Ar, O_2, O, N_2 and CO and several other trace species (see Figure 1.2). The thermosphere is the collisional part of the upper atmosphere and is bounded below by the homopause (115-130 km altitude), above which turbulent mixing is weak enough that the constituent species have separate scale heights (*Bougher et al.*, 2008) and above by the exobase (160-200 km), above which an escaping particle moving radially will undergo one

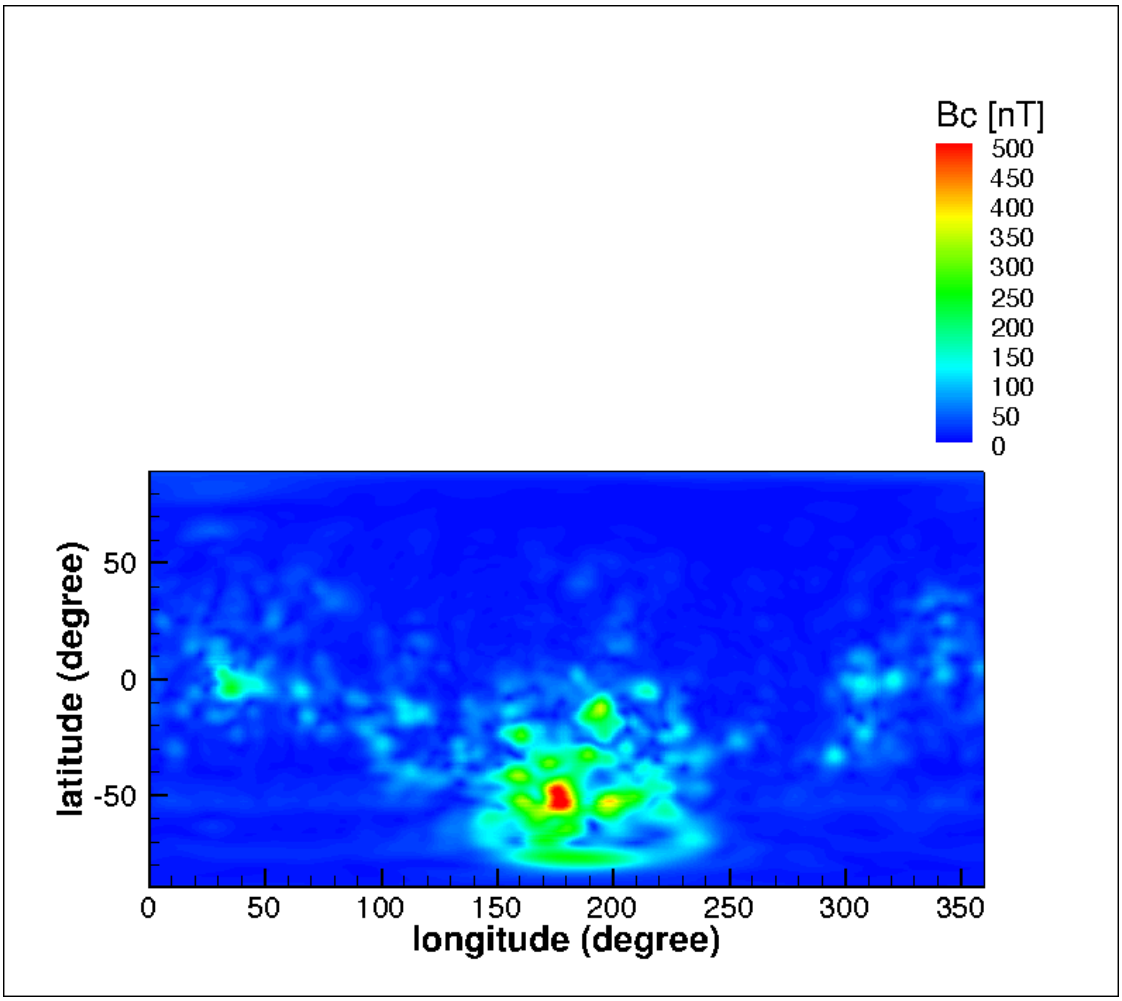

Figure 1.1: The remnant crustal magnetic field magnitude at an altitude of 200 km, calculated using the 60 degree harmonic expansion of *Arkani-Hamed* (2001) in the geographic (GEO) coordinate system.

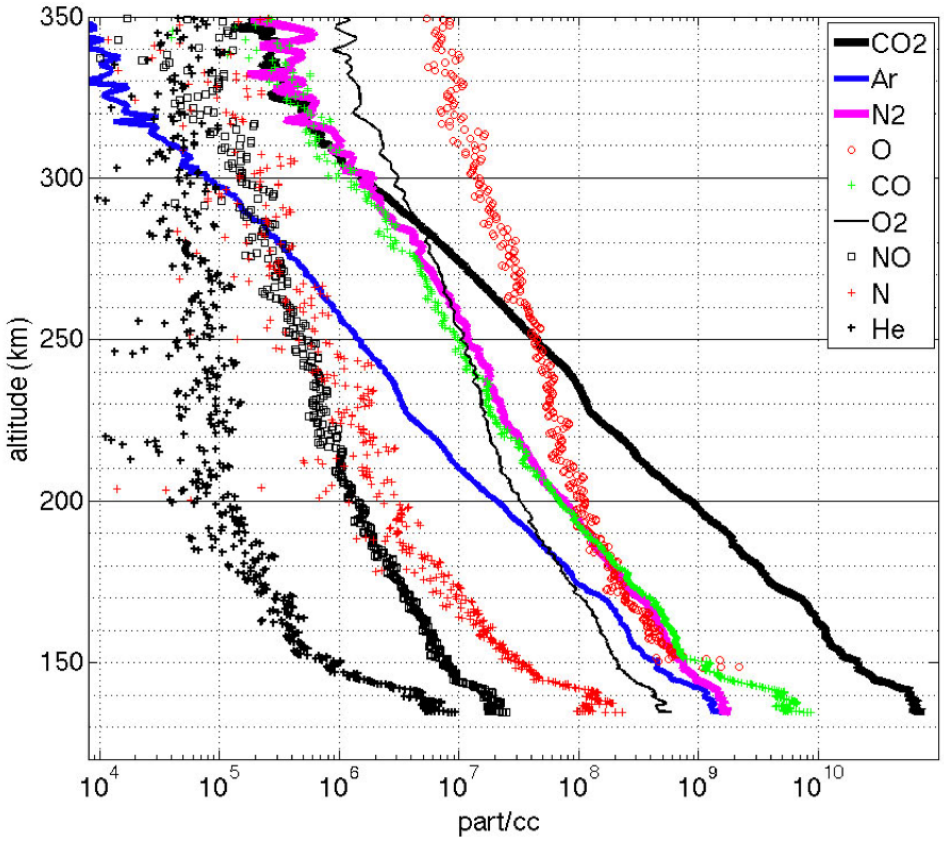

Figure 1.2: An example of the variation with altitude of 9 atomic and molecular species during a single MAVEN deep dip pass on orbit #1064 is shown. For the trace gas He gas scattering in the instrument at the lowest altitudes may distort the profile. N, O_2, O, and NO are derived from open source (neutrals and ions) measurements and the remaining gases from closed source (non-reactive neutrals) data (*Mahaffy et al.*, 2015).

collision on average (*Valeille et al.*, 2009). Thermospheric structure and dynamics are controlled primarily by solar UV and EUV heating, radiative and collisional cooling, gravity and planetary waves, thermal tides, dust activity and IR heating in the lower atmosphere, and charged particle precipitation (*Bougher et al.*, 2014).

The region above the exobase, where neutral particles collide rarely and hence move mostly ballistically, is called the exosphere and is dominated by atomic hydrogen and oxygen, with trace amounts of helium and carbon (*Lee et al.*, 2014a,b). Embedded in the upper atmosphere is the Martian ionosphere, whose ion component is primarily O_2^+. The major source of daytime ionization at Mars is solar EUV radiation. The photoionization rate peak is at an altitude of 130-140 km (*Bougher et al.*,

2008). The major neutral at this altitude is CO_2, which led most to believe that the the major ion would be CO_2^+ as a direct consequence of the photoionization of CO_2. However, CO_2^+ quickly reacts with neutral O to produce mostly O_2^+, which becomes the major ion near 130-140 km altitude. The O_2^+ ion peak density occurs where the EUV optical depth of CO_2 is unity ($\sim$120 - 130 km at the subsolar point). O_2^+ dissociatively recombines with thermal electrons, producing hot O atoms that populate the exosphere. The main chemical reactions are as follows:

$$\begin{aligned} CO_2 + h\nu &\rightarrow CO_2^+ + e^- && (1.1)\\ CO_2^+ + O &\rightarrow O_2^+ + CO && (1.2)\\ &\rightarrow O^+ + CO_2 && (1.3)\\ O + h\nu &\rightarrow O^+ + e^- && (1.4)\\ O^+ + CO_2 &\rightarrow O_2^+ + CO && (1.5)\\ O_2^+ + e^- &\rightarrow O + O + energy && (1.6) \end{aligned}$$

Unlike Earth and Venus, Mars with a weak gravity allows an extended corona of hot species (*Valeille et al.*, 2009).

All solar system objects that are impenetrable obstacles to the solar wind, either by having a sufficiently large intrinsic magnetic field or a dense enough ionosphere, form a bow shock (*Nagy et al.*, 2004). For Mars, the extended dayside ionosphere forms a conducting obstacle to the solar wind, which must slow down when it encounters the obstacle. The transition from supersonic to subsonic solar wind flow produces a bow shock. The bow shock stands off an effective obstacle at a distance that can be estimated from gasdynamic and/or magnetohydrodynamic approximations. The region between the shock and the obstacle is termed the magnetosheath (Figure 1.3). Significant mass-loading takes place within the magnetosheath, indicating the existence of an extended hydrogen/oxygen exosphere. A well-defined

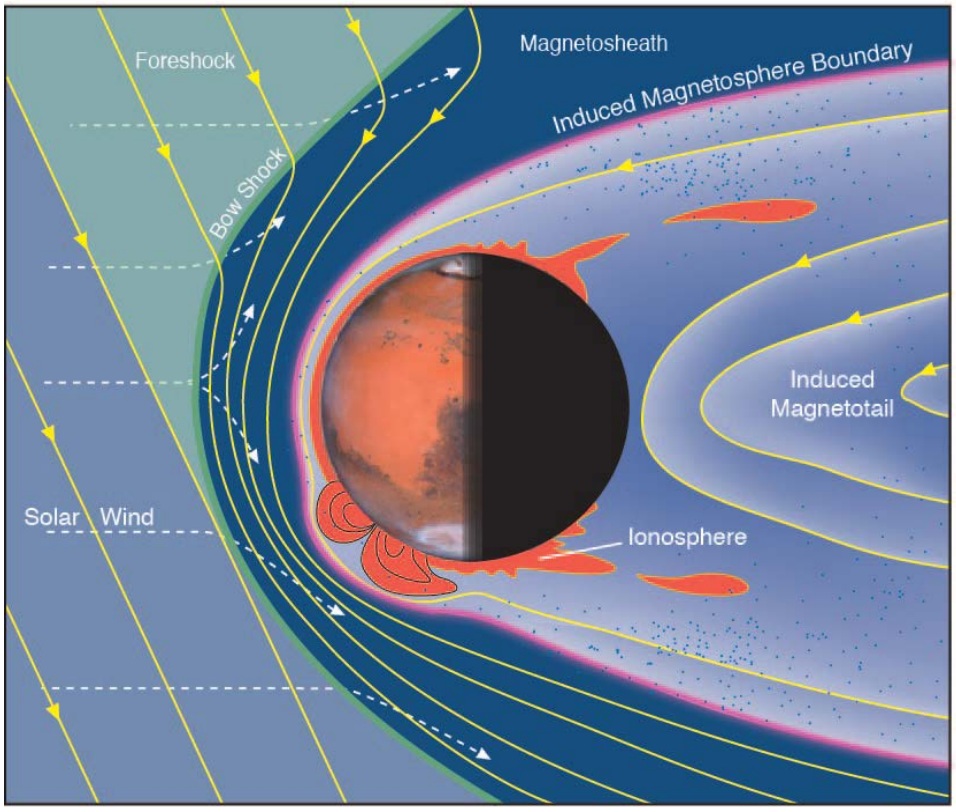

Figure 1.3: Illustration of the global plasma interaction between Mars and the solar wind (*Lillis et al.*, 2015). It also depicts the major boundaries and regions in the meridional plane.

boundary, the Magnetic Pileup Boundary (MPB) or Induced Magnetosphere Boundary (IMB), separates the planetary ion dominated Magnetic Pileup Region (MPR) from the magnetosheath. The MPB is a thin, sharp transition, where the solar wind proton density drops sharply, but sharp increase of electron density and increase of the solar wind magnetic field. In the case where the planet has an intrinsic magnetic field, like at the Earth, Mercury and the giant planets, the interaction between the supersonic, superalfvenic, magnetized solar wind and the intrinsic magnetic field of the planet results in the formation of a magnetosphere. The outer limits of the magnetosphere is called the magnetopause and the region between the magnetopause and the bow shock is referred to as the magnetosheath. Many complex wave and particle interaction processes take place in these regions. Figure 1.4 provides a representative illustration of these interaction regions.

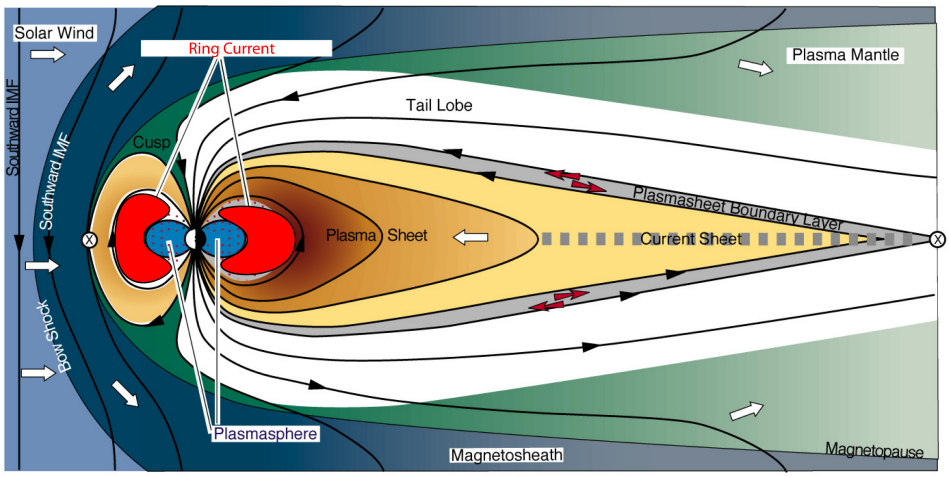

Figure 1.4: Interaction of the solar wind with the Earth's Magnetosphere (*Wang*, 2008).

It is generally believed that an induced magnetotail forms behind the planet with approximately sunward and anti-sunward-directed magnetic tail lobes. However, recent suprathermal electron and magnetic field observations in the near wake, sampled along its elliptical orbit during nominal solar wind conditions at altitudes ranging from its ∼150 km periapsis to the tail magnetosheath, instead reinforce a picture with magnetic fields rooted in the planet throughout much of the Martian magnetotail. A combination of in-situ plasma and field data and MHD models is used to illustrate this finding (*Luhmann et al.*, 2015). Therefore, the situation on Mars is different from that found at Venus, also unmagnetized and with a substantial atmosphere. Crustal remanent magnetic fields (spatially inhomogeneous and strongest in ∼1/3 of the southern hemisphere between 120 and 240° east longitude) rotate with the planet and modify the global Venus-like interaction, standing off the solar wind to distances of up to 1000 km (*Brain et al.*, 2003). The crustal fields and specifically the topology thereof, result in an inhomogeneous pattern of electron precipitation, particularly on the nightside, where the ionosphere is patchy and highly irregular (*Fillingim et al.*, 2007, 2010).

1.2 The drivers controlling atmospheric escape

Several factors are thought to control atmospheric escape rates from Mars. One of the hot research topics is to characterize the sensitivity of the different escape channels to these controlling factors. This is important both for the sake of characterizing the Martian upper atmospheric and near-space environment today and also to allow a confident extrapolation of these escape processes to conditions that existed over the last 4.5 Gyr. These factors fall into two broad categories: solar and planetary, which are respectively summarized in Table 1.1 and Table 1.2 (*Lillis et al.*, 2015).

Table 1.1: Solar and heliospheric factors affecting atmospheric escape.

Solar and Heliospheric factors	Atmospheric Escape Dependence
Solar EUV flux	Heats neutrals. Also, ionization of neutrals allows escape via solar wind pick up, sputtering and dissociative recombination.
Solar wind pressure	Determines plasma boundary locations, hence fraction of exosphere available for pickup ion loss and sputtering.
IMF direction and intensity	Determines global magnetic geometry and topology, hence: 1) pattern of impacting pickup ions for sputtering, 2) sizes/locations of escape channels for energized ions.
Solar energetic particle (SEP) flux	SEPs heat and ionize the atmosphere, allowing for greater escape.

1.3 The role of global models in constraining Mars atmospheric escape

In this section, we will discuss the role of global models in constraining Mars atmospheric escape and the also summarize the previous MHD modeling studies of Mars.

Table 1.2: Planetary factors affecting atmospheric escape.

Planetary factors	Atmospheric Escape Dependence
Subsolar longitude (i.e. Mars rotation phase) & subsolar latitude (determined by season and obliquity)	Longitude and latitude of the crustal fields with respect to the solar wind alters global plasma interaction and ion loss.
Heliocentric distance and eccentricity	Distance from the sun affects solar wind pressure and EUV flux.
Dust activity	Dust storms heat the lower atmosphere, increasing scale heights and neutral winds in the thermosphere.

1.3.1 Global models and their application to characterize atmospheric escape and its variation

As mentioned earlier, the upper atmosphere and near space environment of Mars is a vastly complex system involving a wide variety of physical processes and a wide range (many orders of magnitude) of particle densities. Computer simulations can improve understanding of such complex systems by helping to constrain which process or processes, and to what relative degree, may be responsible for features observed in the system, as well as providing a representation of aspects or regions of the system that may be inaccessible to measurements. While 1-D representations (with altitude as the spatial dimension) of the upper atmosphere system have been useful in elucidating some of the physics (atomic processes and particle transport are the broadest categories), most if not all characteristics of the system are not only spherically asymmetric but display strong horizontal gradients and flows. Therefore the system cannot be understood without considering it as a heterogeneous 3-D spherical shell around the planet, extending out to several to tens of Martian radii.

Over the last two decades (with heritage going back even further), various plasma models based on different assumptions, i.e., test particle model (*Fang et al.*, 2010; *Curry et al.*, 2013, 2014, 2015a), multi-species MHD model (*Ma et al.*, 2004; *Ma*

and Nagy, 2007a; *Ma et al.*, 2014), multi-fluid MHD model (*Harnett and Winglee*, 2006; *Najib et al.*, 2011; *Riousset et al.*, 2013, 2014; *Dong et al.*, 2014) and kinetic hybrid model (*Modolo et al.*, 2012; *Brecht and Ledvina*, 2014a) have been used to simulate the solar wind interaction with the Martian upper atmosphere and calculate the associated ion escape rates (*Brain et al.*, 2010, 2012). Besides the plasma models, a suite of thermosphere and exosphere models have also been developed to simulate subsets of this global system (e.g. *Bougher et al.*, 2006, 2015a; *Lee et al.*, 2015). Since no single model can accurately represent the motions of charged and neutral particles over 10 or more orders of magnitude in density, multiple separate models must be coupled together, as will be discussed in this section.

First, from the ground to just above the exobase, global ionosphere thermosphere model (GITM) simulates the atmosphere (including the thermosphere and ionosphere) in the fluid regime as it responds to topography, planetary rotation and solar heating and ionization (*Ridley et al.*, 2006; *Bougher et al.*, 2015a). Second, the Adaptive Mesh Particle Simulator (AMPS) is a Direct Simulation Monte Carlo (DSMC) model (*Tenishev and Combi*, 2008), which simulates the hot neutral atmosphere with macro-particles from a few scale heights below the exobase out to several Mars radii in order to capture the physics of the transition from the collisional regime (where fluid treatments are valid) to the collisionless regime (where kinetic treatments are required). AMPS takes inputs from GITM near its lower boundary and is not time-dependent. Last, global plasma models, as their name suggests, simulate the plasma physics of the interaction between the solar wind and the Martian ionosphere and exosphere, using either a magnetohydrodynamic (MHD) approach (*Ma et al.*, 2004; *Ma and Nagy*, 2007a; *Najib et al.*, 2011; *Ma et al.*, 2015; *Luhmann et al.*, 2015) or a hybrid approach (*Modolo et al.*, 2012; *Brecht and Ledvina*, 2014a) where ions are treated kinetically and electrons are simulated as a massless charge-balancing fluid. Global plasma models take exospheric inputs from DSMC models and thermospheric

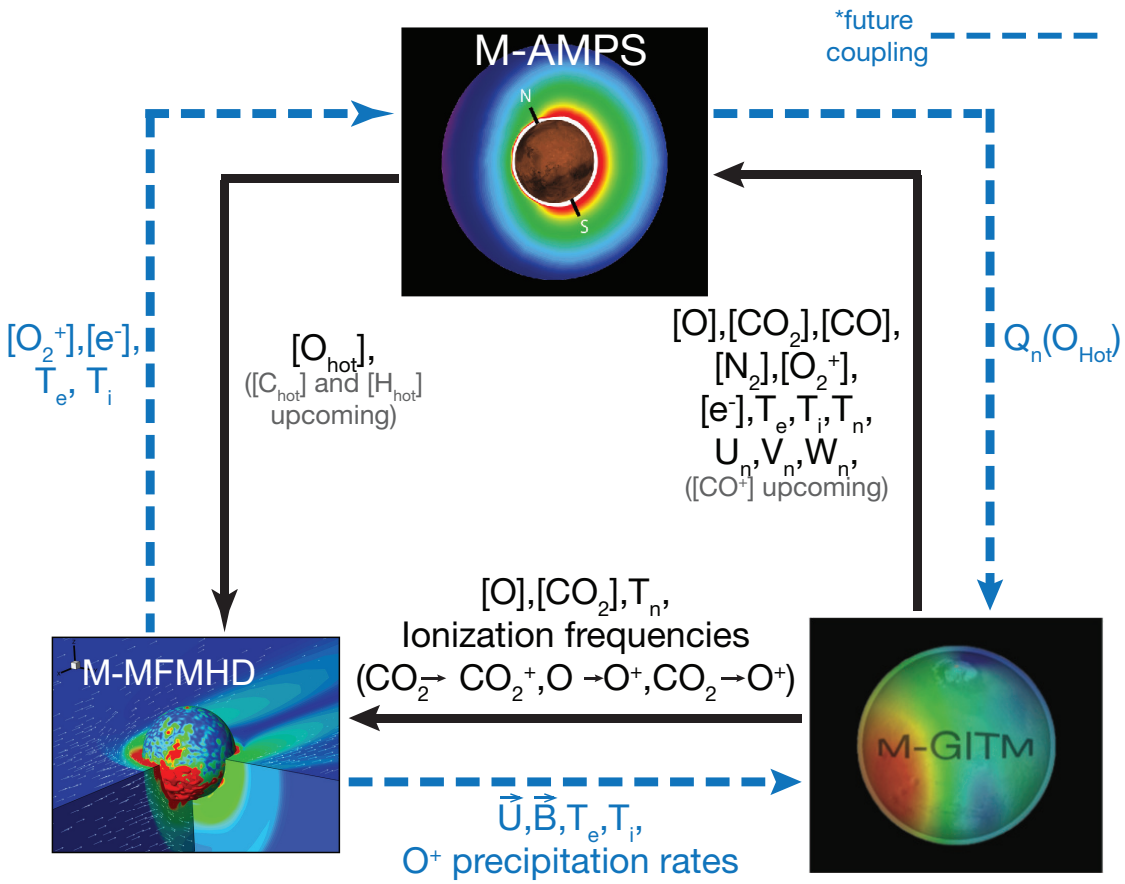

Figure 1.5: Schematic diagram showing the coupling approach between the different components. The black solid lines represent completed coupling, via the variables colored black. The dashed blue lines represent future coupling via the variables colored blue (Adapted from *Dong et al.*, 2015a).

inputs from GITM. These one-way couplings represent the current state-of-the-art; the models are not currently capable of simulating feedbacks between the space environment and ionosphere/thermosphere, although 2-way coupling is planned in the near future (Figure 1.5).

Global models of the Mars upper atmosphere and near space environment are an essential part of our strategy for determining global atmospheric escape rates at the current epoch and through time. In situ coverage is limited to single points in time and space along a spacecraft's precessing orbit, while remote-sensing data has greater coverage but requires more inversion and is not as comprehensive in terms of derived quantities. Therefore, global models are necessary to bridge the measurement 'gaps',

both spatially and with respect to the controlling drivers. As well as utilizing global models for spatial interpolation, we can also make use of them to estimate escape rates during some of the more extreme conditions that are believed to have prevailed over the history of the solar system.

1.3.2 Previous Global Plasma Modeling Studies of Mars

Since the focus of this thesis lies in the MHD modeling, we briefly discuss the previous MHD modeling studies of Mars related to this thesis work. *Shinagawa* (1999) developed a two-dimensional MHD model of some aspects of the solar wind interaction with Mars ionosphere. While this model described the ionospheric electron density profiles and magnetic fields reasonably well, it was not sufficient to account for the 3-D effects, such as the tension of the magnetic field and some important plasma transport effects. *Liu et al.* (1999) developed a 2-species, 3-D, MHD model of Mars by considering solar wind protons and heavy O_2^+ separately. *Liu et al.* (2001) added a third major ion species O^+ to their model and also added a surface dipole field in order to simulate the crustal field. This model gave reasonable agreement with available data with respect to the bow shock location and structure. *Harnett and Winglee* (2003) developed a 3-D, non-ideal single fluid model incorporating non-ideal MHD effects such as the Hall effect. However, there was no information about plasma composition, since the model did not include mass loading.

Next *Ma et al.* (2002, 2004) developed a multispecies MHD model for Mars using first a Cartesian (2002) and later a spherical grid (2004) structure. They were also able to have cell sizes as small as 10 km in the ionospheric region and therefore obtain a much improved description of this region. This model did a good job in reproducing the observed density and magnetic field observations. The addition of the Hall effect to the model allowed them to describe some kinetic effects that cannot be accounted for with ideal MHD. This model has been applied extensively to Mars

and Titan. However, the single fluid model is still limited by the single momentum and pressure/energy equations that fails to describe the individual dynamics and energetics of the individual ion species. The multi-fluid model by *Harnett and Winglee* (2006) showed asymmetries that the single fluid MHD model could not reproduce, however, it has limited ion composition capability and a very coarse resolution to describe the ionospheric processes appropriately. *Najib et al.* (2011) developed a new multi-fluid MHD model, which includes the important ionospheric chemistries and collisions between different particle species. The multi-fluid MHD code solves the separate mass, momentum and energy equations for the four ion fluids H^+, O^+, O_2^+, CO_2^+ (*Najib et al.*, 2011).

1.4 Observations by previous missions to Mars

A series of spacecraft with plasma instrumentation have been sent to Mars, (e.g., Phobos 2, Mars Global Surveyor (MGS), and Mars Express (MEX) missions) over the last 30 years. A number of papers reporting on the measurement of ion escape rates by the ASPERA-3 instrument on the Mars Express spacecraft have been published (e.g., *Barabash et al.*, 2007; *Lundin et al.*, 2008, 2009, 2013; *Nilsson et al.*, 2011). *Barabash et al.* (2007) first presented the results of their ion escape measurements (3.2×10^{23} s^{-1} for O^+, O_2^+ and CO_2^+), which was measured by the ASPERA-3 (Analyzer of Space Plasma and Energetic Atoms) instrument carried aboard the Mars Express spacecraft. Later, *Lundin et al.* (2008) found that the new energy settings introduced in May 2007 enabled the MEX ASPERA-3 ion mass analyzer (IMA) to accurately cover the low energy range (10-100 eV) for all ions, especially the cold ionospheric ions. Measurements with these new settings reveal in great detail the low-energy comet-like ion outflow, inferred from Phobos-2. They found that the low energy coverage greatly increased the observed Mars ion escape rates.*Lundin et al.* (2008) suggested that the total ion escape rate (O^+, O_2^+ and CO_2^+) is around 3×10^{24} s^{-1}

during solar cycle minimum conditions and it may achieve values more than 10^{25} s^{-1} during the solar cycle maximum condition. *Nilsson et al.* (2011) found that the net ion escape flux for solar cycle minimum conditions is around 2×10^{24} s^{-1}. Besides, *Nilsson et al.* (2011) pointed out that the average flux ratio of the molecular species (O_2^+ and CO_2^+) to O^+ ions is 0.9 ± 0.1 based on the statistics of MEX data from May 2007 to May 2011 for ion energies below 50 eV. In *Lundin et al.* (2013), they reported that the average heavy ion escape rate is increased by a factor of ~ 10, from $\sim 1{\times}10^{24}$ s^{-1} (solar minimum) to $\sim 1{\times}10^{25}$ s^{-1} (solar maximum). On the other hand, both *Verigin et al.* (1991) (by Phobos-2 observations) and *Nilsson et al.* (2011) suggested that high solar activity leads to ~ 2.5 times higher ion escape rate than the low solar activity result. The recent paper published by *Ramstad et al.* (2015) showed that the solar wind density and velocity can greatly affect the ratio of escape rate between low and high solar EUV conditions. They adopted more than seven years of ion flux measurements in the energy range 10 eV–15 keV from ASPERA-3/IMA instrument on board MEX.

A careful analysis of individual mass spectra in *Lundin et al.* (2009) shows that the CO_2^+ contribution to the low-energy (< 300 eV) heavy ion outflow is $\leq 10\%$. Moreover, *Lundin et al.* (2011) studied how the ionospheric O^+ outflow and escape are related to the crustal magnetic field regions by analyzing the ASPERA-3 data from MEX. They found that a large fraction of the energized O^+ ions remain magnetically trapped and are recycled within the mini-magnetospheres generated by the small-scale planetary crustal field regions at Mars. When the crustal field faces the sun, it has an effect to deviate the dayside ion flow and thus reducing the tailward transport and escape of ionospheric plasma.

1.5 MAVEN mission and its primary scientific goals

On November 18, 2013, NASA launched the Mars Atmosphere and Volatile EvolutioN (MAVEN) spacecraft, and it successfully went into orbit at Mars on September 21, 2014. The spacecraft is three-axis stabilized, with an Articulated Payload Platform (APP) that allows three instruments to be oriented in space independent of the spacecraft orientation (Figure 1.6). This configuration allows those instruments that need to be pointed relative to the Sun or to the solar wind to be oriented properly, while also allowing those instruments that need to be pointed at the planet to do so (*Jakosky et al.*, 2015a).

MAVEN mission is a NASA Mars Scout mission, selected primarily to determine the importance of the role of escape of volatiles to space on the planet's climatic evolution, i.e. its transition from an environment with sufficient atmospheric pressure and temperatures that liquid water was at least episodically stable, to the low-pressure, cold, arid climate of today. The three primary scientific goals of MAVEN are to 1) determine the structure, composition and dynamics of the Martian upper atmosphere, 2) determine rates of atmospheric escape through various processes at the current epoch and with these answers, 3) determine the integrated loss to space that has occurred through Martian history (*Bougher et al.*, 2014, 2015b; *Lillis et al.*, 2015; *Jakosky et al.*, 2015a). In total, there are nine instruments onboard MAVEN spacecraft (see Figure 1.7) to help understand how solar wind interacts with the Martian upper atmosphere. The Particles and Fields Package includes Solar Wind Electron Analyzer (SWEA) (*Mitchell et al.*, 2015), Solar Wind Ion Analyzer (SWIA) (*Halekas et al.*, 2015), Suprathermal and Thermal Ion Composition (STATIC) (*McFadden et al.*, 2015), Solar Energetic Particle (SEP) (*Larson et al.*, 2015), Langmuir Probe and Waves (LPW) (*Ergun et al.*, 2015), Extreme Ultraviolet Monitor (EUV), and Magnetometer (MAG) (*Connerney et al.*, 2015). These instruments can characterize the solar wind and the ionosphere of the planet. The Remote Sensing Package includes

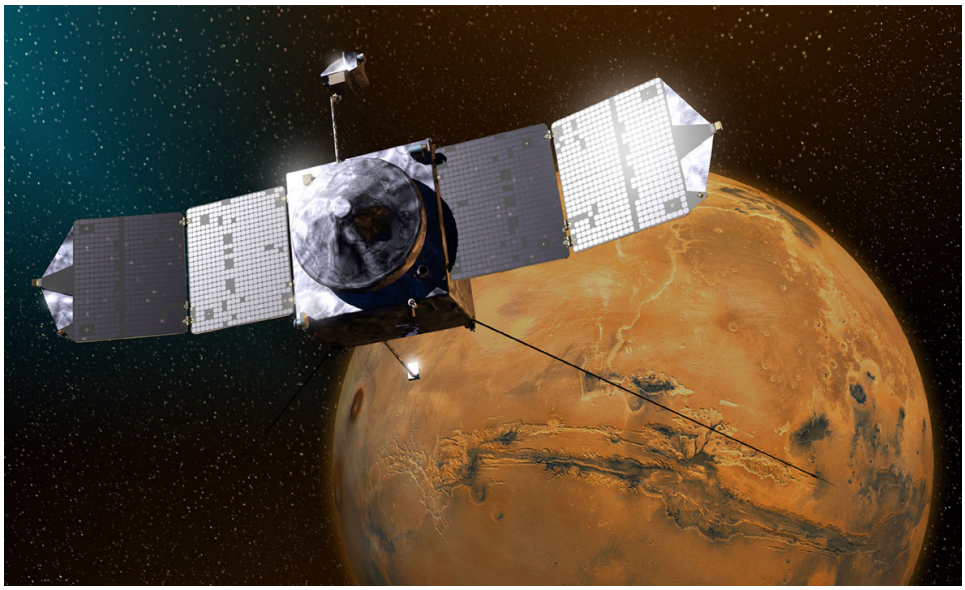

Figure 1.6: Artist's conception of the MAVEN spacecraft. High-gain antenna in the middle is 2 m diameter for scale. Articulated Payload Platform (APP) is visible at the top; SWEA boom at bottom center; one of the LPW booms is visible at lower right. The second panel of each solar-array wing is canted for increased aerodynamic stability (*Jakosky et al.*, 2015a)

the Imaging Ultraviolet Spectrograph (IUVS) (*McClintock et al.*, 2014), which determines global characteristics of the upper atmosphere and ionosphere via remote sensing. The one related to the ionospheric neutral and ion measurements is the Neutral Gas and Ion Mass Spectrometer (NGIMS) (*Mahaffy et al.*, 2014), which measures the composition and isotopes of neutral gas and ion species.

In this thesis, we will focus primarily on MAVEN science goal 2, i.e. to characterize the ion escape rates from the Martian atmosphere at the current epoch and how they vary spatially, with solar and heliospheric influences (e.g., solar EUV, solar wind pressure) as well as planetary parameters (e.g., season, subsolar longitude). We will also examine, in somewhat less detail, MAVEN Science goal 3 by studying the solar wind interaction with the Martian upper atmosphere at ancient times. In other words, with knowledge of how the controlling factors govern atmospheric loss processes today, how much Mars total atmosphere may have been lost since the earliest epochs of the solar system and how does this inform our view of Mars' climate evolution. Mars atmospheric escape (and the history thereof) is a challenging problem to investigate,

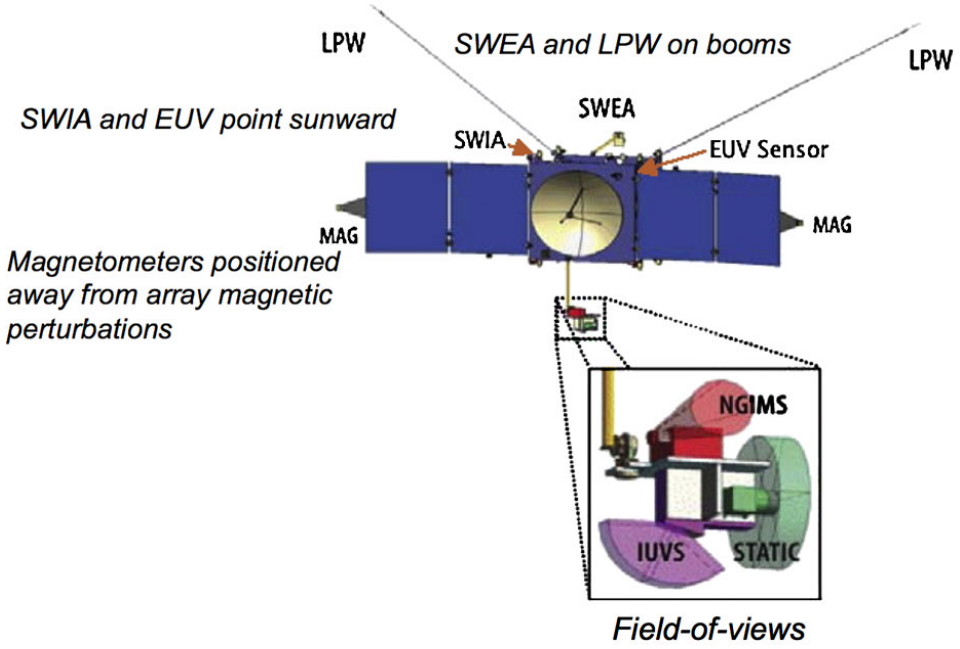

Figure 1.7: Instrument accommodation. Diagram shows the locations of the science instruments on the body of the spacecraft and on the APP (*Jakosky et al.*, 2015a)

with multiple interconnected physical processes, nonlinear relationships with internal and external drivers and spatially and temporally inhomogeneous patterns of escape. Despite the tightly focused suite of integrated investigations onboard the MAVEN spacecraft, in situ coverage is limited to single point in time and space along MAVEN's precessing orbit. Also, it is important to note that global ion escape rates are not directly measured. Lastly, MAVEN may not be fortunate enough to make escape measurements over the entire range of solar conditions thought to have been prevalent over solar system history.

In order to bridge these measurement 'gaps' (spatial, temporal and with respect to solar inputs and upper atmospheric processes and quantities), it is imperative to closely integrate several types of physics-based models with multi-instrument analysis of MAVEN data. Part of this thesis will discuss the strategy for determining, to the best of our ability using data and models, rates of ion escape from the Martian atmosphere, how they are connected, how they vary with solar inputs and how they may have changed over the history of our solar system. Unlike many planetary

orbiter or flyby missions with typically diverse sets of science goals and associated instrumentation, MAVEN is true to the NASA Mars Scout concept in that it is focused on understanding an as-yet insufficiently explored aspect of the Martian system, i.e., the structure and dynamics of the upper atmosphere and how escape of gases depends on solar and planetary drivers, both now and in the past.

1.6 Outline of the dissertation

The purpose of this thesis is to continue the previous efforts to improve a self-consistent three-dimensional multi-fluid MHD model in order to study the solar wind interaction with the Martian upper atmosphere and build a model library for the NASA MAVEN mission (2014-2016). In this thesis, we aim to address the following four main scientific questions that are closely related to the primary scientific goals of the MAVEN mission:

1) What are the Martian ion escape rates at the current epoch and ancient times?

2) What controls the ion escape processes at the current epoch? How are the ion escape variations connected to the solar cycle, crustal field orientation and seasonal variations?

3) How do the variable 3-D cold neutral thermosphere and hot oxygen corona affect the solar wind-Mars interaction?

4) How does the Martian atmosphere respond to extreme variations (e.g., ICMEs) in the solar wind and its interplanetary environment?

In order to properly address these questions, we invest considerable effort to improve the multi-fluid MHD model. The most significant improvements include:

1) We built a one-way coupling framework between three comprehensive models: the 3-D Mars multi-fluid Block Adaptive Tree Solar-wind Roe Upwind Scheme (BATS-R-US) MHD code (MF-MHD), the 3-D Mars Global Ionosphere Thermosphere Model (M-GITM) and the Mars exosphere Monte Carlo model Adaptive Mesh

Particle Simulator (M-AMPS). This allows the MF-MHD code to use a more realistic 3-D cold neutral atmosphere from the M-GITM model and 3-D hot oxygen corona from the M-AMPS code.

2) The Space Weather Modeling Framework (SWMF) is coupled with the NASA JPL SPICE code, which allows us to investigate the effects of crustal field orientations, seasonal variations and a real solar wind event on solar wind-Mars interaction accurately. Given the high orbital eccentricity of Mars, the SPICE code can help to calculate, for example, the exact length of a synodic day and the exact subsolar longitude and latitude based on a specific universal time (UT).

3) Some important physical process such as ion-ion collisions are added into the model. We also added collisional resistivity (*Luhmann*, 1991; *Terada et al.*, 2009) in the code which allows physics-based collisional magnetic reconnection to occur in the Martian ionosphere. We also added a command called "MULTIIONSTATE" which allows multi-fluid MHD code to output single ion velocities and single ion temperatures by averaging the multi-fluid calculations. The effect of friction between different ion species is also studied.

4) In addition, we implemented the separated ion and electron pressure equations into the multi-fluid MHD code which allows us to calculate the electron temperature self-consistently. The electron temperature can be different from ion and neutral temperatures in the collisionless region.

This thesis is organized as follows. Chapter II introduces the governing equations of the multi-fluid MHD model. Chapter III discusses the work done by one-way coupling between MF-MHD and M-TGCM, which includes several case studies at both current epoch and ancient Mars. Chapter IV discusses the effects of 3-D cold neutral atmosphere and hot corona on the solar wind interaction with Mars upper atmosphere. Chapter V discusses the effects of crustal field orientation, solar cycle and seasonal variations on solar wind-Mars interaction, which builds a model library

of ion escape rates for the MAVEN mission. In Chapter VI, we study the Martian response during the 2015 March 8th ICME event by using the multi-fluid code. In Chapter VII, we present the preliminary results by separating the electron and ion pressure equations in the multi-fluid MHD model. We also discuss future work that is planned making use of the MF-MHD code in conjunction with MAVEN data analysis activities in Chapter VII.

CHAPTER II

Mars multi-fluid MHD equations

2.1 Transport Equations for Multi-fluid Plasma

Plasmas can be treated by employing a particle-in-cell (PIC) method (*Lapenta*, 2012), test-particle approach (*Curry et al.*, 2013), hybrid-PIC code with kinetic ions and electron fluid (*Winske and Omidi*, 1993; *Winske et al.*, 2003; *Dong et al.*, 2013), and hybrid Vlasov-Maxwell (HVM) or hybrid Vlasov-Poisson (HVP) solver (*Valentini et al.*, 2007), but they can also be considered as a conducting fluid (one fluid theory) without specifying its various individual species. In this case, each macroscopic variable is formed by adding the contributions of the various particle species in the plasma. Using simplified forms of the transport equations (i.e., conservation of mass, momentum, and energy) and additional electrodynamic equations (Maxwell curl equations, conservation of electric charge, and generalized Ohm's law) the magnetohydrodynamic (MHD) theory is created. In recent years, the extended MHD (XMHD) formulations (e.g., the multi-species MHD (*Ma et al.*, 2004; *Ma and Nagy*, 2007a), Hall MHD (*Ma et al.*, 2007b), multi-fluid MHD (*Najib et al.*, 2011; *Dong et al.*, 2014), and anisotropic pressure MHD (*Ohia et al.*, 2012; *Meng et al.*, 2013)) are becoming more and more popular since they can capture more kinetic ion/electron physics than a single fluid code. For example, the recent study by *Ohia et al.* (2012) shows that including anisotropic electron pressure in a MHD code by adopting an

appropriate fluid closure can capture the effects of the asymmetric structure of the current layer in magnetic reconnections, and thus be able to match the current layer of the fully kinetic simulations in the strong guide-field limit.

In this chapter, we will focus on the multi-fluid MHD approach which solves separate continuity, momentum and energy equations for each ion species (*Glocer et al.*, 2009; *Najib et al.*, 2011; *Tóth et al.*, 2012; *Dong et al.*, 2014). As will be shown later, the treatment of the electron fluid momentum equation in a multi-fluid MHD code (*Dong et al.*, 2014) and in a hybrid-PIC code (*Dong et al.*, 2013) is essentially the same. The closure of the generalized Ohm's law is crucial to capturing more kinetic physics in a fluid code.

2.1.1 Generalized transport equation

In the kinetic theory it is necessary to know the distribution function for the system of particles. The distribution function for a specific particle species s, $F_s\left(\mathbf{r_s}, \mathbf{v_s}, t\right)$, is defined as the number of the particles in 6-D phase space. Here the vectors $\mathbf{r_s}$ and $\mathbf{v_s}$ are the position and velocity, respectively, of the phase space. The time evolution of a phase space distribution function $F_s\left(\mathbf{r_s}, \mathbf{v}_s, t\right)$ can be described by the Boltzmann equation:

$$\frac{\partial F_s\left(\mathbf{r_s}, \mathbf{v}_s, t\right)}{\partial t} + v_s \cdot \nabla_r F_s\left(\mathbf{r_s}, \mathbf{v}_s, t\right) + a_s\left(\mathbf{r_s}, \mathbf{v}_s, t\right) \cdot \nabla_{v_s} F_s\left(\mathbf{r_s}, \mathbf{v}_s, t\right) = \left(\frac{\delta F_s\left(\mathbf{r_s}, \mathbf{v}_s, t\right)}{\delta t}\right)_{coll} \tag{2.1}$$

where the subsrcipt s refers to the given ion species or to the electrons. Time, t, location $\mathbf{r_s}$ and species velocity $\mathbf{v_s}$ are independent variables. The acceleration term, $\mathbf{a_s}$, is caused by the external forces acting on the changed particles. In space plasma physics, it usually refers to the electromagnetic Lorentz and gravitational forces.

$$\mathrm{a_s} = \mathbf{G} + \frac{q_s}{m_s}\left(\mathbf{E} + \mathbf{v_s} \times \mathbf{B}\right) \tag{2.2}$$

The right hand-side term in Equation (2.1) represents the changing rate of the phase-space distribution function due to both elastic and non-elastic collisions.

The bulk gas flow or average drift velocity can be defined as $\mathbf{u_s} = \langle \mathbf{v_s} \rangle$, where

$$\langle \mathbf{v_s} \rangle = \iiint_{\infty} \mathbf{v_s} f_s \left(\mathbf{r_s}, \mathbf{v}_s \right) d^3 v \tag{2.3}$$

The Boltzmann equation can also be expressed in terms of the random velocity $\mathbf{c_s}$, which is the velocity of the particle with respect to $\mathbf{u_s}$, at time t and location $\mathbf{r_s}$.

$$\mathbf{c_s} = \mathbf{v_s} - \mathbf{u_s} \left(\mathbf{r_s}, t \right) \tag{2.4}$$

Multiplying Equation (2.1) by m_s, $m_s \mathbf{c_s}$ and $m_s c_s^2/2$ and integrating over the entire velocity space, we obtain the zeroth, first, and second velocity moments of the Boltzmann equations,

$$m_s \frac{\partial n_s}{\partial t} + m_s \nabla \cdot \left(n_s \mathbf{u}_s \right) = m_s \frac{\delta n_s}{\delta t} \tag{2.5}$$

$$m_s n_s \frac{\partial \mathbf{u}_s}{\partial t} + m_s n_s \left(\mathbf{u_s} \cdot \nabla \right) \mathbf{u}_s + \nabla \cdot \vec{P}_s - n_s m_s G - n_s q_s \left(\mathbf{E} + \mathbf{u}_s \times \mathbf{B} \right) = \frac{\delta M_s}{\delta t} \tag{2.6}$$

$$\frac{1}{\gamma - 1} \frac{\partial p_s}{\partial t} + \frac{1}{\gamma - 1} \left(\mathbf{u}_s \cdot \nabla \right) p_s + \frac{\gamma}{\gamma - 1} p_s \left(\nabla \cdot \mathbf{u}_s \right) + \left(\nabla \cdot \mathbf{h_s} \right) = \frac{\delta E_s}{\delta t} \tag{2.7}$$

where γ=(n+2)/n=5/3 is the specific heat ratio and n=3 is the degree of freedom. In the energy equation, the heat flux $\mathbf{h_s}$ is defined as $\mathbf{h_s} = \frac{1}{2} m_s n_s \langle c_s^2 \mathbf{v_s} \rangle$. This term can be approximated by $\mathbf{h_s} = -\kappa \nabla T_s$ when collisions are frequent. $\vec{P}_s$ is the pressure tensor, which is defined as,

$$P_{i,j} \left(\mathbf{r}, t \right) = m \iiint_{\infty} c_i c_j F \left(\mathbf{r}, \mathbf{c}, t \right) d^3 c \tag{2.8}$$

After integration, $\vec{\vec{P}}_s = m_s n_s \langle \mathbf{c_s c_s} \rangle$ and can be expressed by a scalar pressure $p_s = \frac{1}{3} m_s n_s \langle c_s^2 \rangle$ and stress tensor τ_s,

$$\vec{\vec{P}}_s = p_s \mathbf{I} + \tau_s \tag{2.9}$$

The stress sensor τ_s can be neglected when collisions are important. We assume it is the case in our work. So plasma is isotropic and $\vec{\vec{P}}_s = p_s \vec{\vec{I}}$.

2.1.2 Collision Terms in Transport Equations for Multi-Fluid Plasma

The collision term in the right hand side of the transport Equation (2.1) describes the rate of change of the phase space distribution function, due to collisions. We will consider two types of collisions: 1) elastic collisions; and 2) inelastic collisions.

2.1.2.1 Elastic collisions

The total momentum and energy are conserved during an elastic collision. In elastic collisions, the particle also does not change its identity. The rate of change of the phase-space distribution function due to elastic collisions was derived by Boltzmann (the derivation can be found in (*Gombosi*, 1994; *Schunk and Nagy*, 2009) and is called the "Boltzmann collision integral"). The simplest and most widely used one is the relaxation time approximation (BGK) (*Gombosi*, 1994). The BGK method assumes the phase-space distribution function F_s gradually relaxes towards an equilibrium (Maxwellian) distribution function F_0, with a time constant τ_{st},

$$\left(\frac{\delta F_s \left(\mathbf{r}, \mathbf{v}_s, t \right)}{\delta t} \right)_{elastic} = - \sum_{t=all} \frac{F_s \left(\mathbf{r}, \mathbf{v_s}, t \right) - F_{0s(st)} \left(\mathbf{r}, \mathbf{v_s}, t \right)}{\tau_{BGK}} \tag{2.10}$$

where the subscript t refers to all species present in the gas mixture (note that species s is also included). τ_{st} is the velocity-independent average collision time between particles s and t. τ_{st} is the characterized time scale which describes how the distribution

function of particles s, F_s asymptotically approaches $F_{0s(st)}$ due to collisions between species s and t. It is important to note that the distribution function, $F_{0s(st)}$, depends on both particle species s and t, therefore $F_{0s(st)}$ evolves with both species s and t as the time increases. The parameters of $F_{0s(st)}$ can be obtained by requiring that the total mass, momentum and energy of gas species s and t to be conserved (*Gombosi*, 1994):

$$F_{0s(st)} = n_s \left(\frac{m_s}{2\pi k T_{s(st)}} \right)^{3/2} \exp \left[-\frac{m_s}{2kT_{s(st)}} \left(\mathbf{v}_s - \mathbf{u}_{st} \right)^2 \right] \tag{2.11}$$

where

$$\mathbf{u}_{st} = \frac{m_t \mathbf{u}_t + m_s \mathbf{u}_s}{m_s + m_t} \tag{2.12}$$

$$T_{s(st)} = T_s + \frac{m_s m_t}{\left(m_s + m_t \right)^2} \left[2 \left(T_t - T_s \right) + \frac{m_t}{3k} \left(\mathbf{u}_t - \mathbf{u_s} \right)^2 \right] \tag{2.13}$$

In order to evaluate the effect of elastic collision on the mass, momentum and energy equations, we repeat what we did before for integrating Equation (2.1). We obtain the zeroth, first and second velocity moments of Equation (2.10) by multiplying it with m_s, $m_s \mathbf{c_s}$ and $m_s c_s^2/2$ and integrating over the entire velocity space. The transfer integrals for elastic collisions can be written as follows:

$$\left(\frac{\delta n_s}{\delta t} \right)_{elastic} = 0 \tag{2.14}$$

$$\left(\frac{\delta M_s}{\delta t} \right)_{elastic} = m_s n_s \sum_{t=all} \nu_{st} (\mathbf{u_t} - \mathbf{u_s}) \tag{2.15}$$

$$\left(\frac{\delta E_s}{\delta t} \right)_{elastic} = \sum_{t=all} \frac{m_s n_s \nu_{st}}{m_s + m_t} \left[3k \left(T_t - T_s \right) + m_t \left(u_t - u_s \right)^2 \right] \tag{2.16}$$

where ν_{st} denotes the non-resonant momentum transfer collision frequency and can be expressed as,

$$\nu_{st} = \frac{m_t}{m_s + m_t} \frac{1}{\tau_{st}} \tag{2.17}$$

In the multi-fluid MHD code, we include several types of collisions: ion-neutral,

ion-ion, electron-neutral, and electron-ion collisions. We summarize those collisions that can play an important role in the Martian (or Venusian) ionosphere as follows.

- Ion-neutral collisions

  The ion-neutral collision frequency, ν_{in}, can be approximated as (*Schunk and Nagy*, 2009).

$$\nu_{in} = 2.21\pi \frac{n_n m_n}{m_i + m_n} \left(\frac{\gamma_n e^2}{\mu_{in}} \right) \tag{2.18}$$

  where γ_n denotes the neutral polarizability and is given by,

$$\gamma_n = \alpha_n \times 10^{-24} cm^3 \tag{2.19}$$

  and μ_{in} represents the reduced mass and is defined as

$$\mu_{in} = \frac{m_i m_n}{m_i + m_n} \tag{2.20}$$

  Plugging Equations (2.19) and (2.20) into Equation (2.18), we obtain

$$\nu_{in} = 2.7 \times 10^{-9} \frac{n_n \left(\alpha_n \mu_{in} \right)^{1/2}}{m_i} s^{-1} \tag{2.21}$$

  We can reformat ν_{in} in a relatively simple form,

$$\nu_{in} = C_n n_n \tag{2.22}$$

  and the value of C_n can be found in *Schunk and Nagy* (2009).

- Ion-ion collisions

  Ion-ion collisions are very important in the Martian lower ionosphere where the collisions between different ion species are frequent. The ion-ion collision

frequency can be written as:

$$\nu_{st} = B_{st}\frac{n_t}{T_t^{3/2}} \tag{2.23}$$

where B_{st} is a numerical coefficient and the values are given in *Schunk and Nagy* (2009).

- Electron-neutral collisions

  The momentum transfer cross section, Q_{en}, for elastic electron-neutral collisions are velocity-dependent which can be found in (*Schunk and Nagy*, 2009).

- Electron-ion collisions

  Electron-ion collisions frequency ν_{ei} is expressed as (*Schunk and Nagy*, 2009):

$$\nu_{ei} = 54.5\frac{n_i Z_i^2}{T_e^{3/2}} \tag{2.24}$$

  where the density n_i is in cm^{-3}, electron temperature T_e is in Kelvin and Z_i is the particle charge number.

2.1.2.2 Inelastic collisions

Inelastic collisions can change the identity of the particle and are very important in the Martian ionosphere. The inelastic collisions play an imperative role in the process of solar wind non-magnetized planet interaction. They are closely related to the chemical processes that occur in Martian ionosphere, thermosphere and exosphere. We assume that all inelastic collisions change the identity of a particle which leads to the chemical reaction. The major chemical reactions in the ionosphere can be classified into three categories: ionization, charge exchange and recombination. Let us start with ionization, which is one of the most important mass loading process.

- **Photochemical Reactions**

  Both photoionization by solar radiation and electron impact ionization by suprathermal electron are very important for formation of the Martian ionosphere and the source of the dayside ionosphere. These two processes are the starting points of all the consequent chemical reactions, such as charge exchange and recombination. Photoionization and impact ionization can be written as:

$$S + h\nu \longrightarrow S^+ + e^- \tag{2.25}$$

$$S + M\,(e, ion, neutral) \longrightarrow S^+ + e^- + M\,(e, ion, neutral) \tag{2.26}$$

  These processes create an S^+ ion from the neutral species, S. Since now we have both neutrals and ions, it is natural that charge exchange between species S^+ and M can happen

$$S^+ + M \longrightarrow S + M^+ \tag{2.27}$$

$$AB^+ + C \longrightarrow AC^+ + B \tag{2.28}$$

  Reaction 2.28 is called ion-atom interchange reaction where both reactants (the ion AB^+ and the atom C) change.

  On the other hand, ions and electrons can also recombine to produce neutrals via inelastic collisions. The recombination is very important to achieve photochemical equilibrium. The first type of recombination is the radiative recombination:

$$S^+ + e^- \longrightarrow S^* + h\nu \tag{2.29}$$

  where S^* indicates that the neutral product may be in an excited state. Another type of recombination is dissociative recombination, which is the dominant

Table 2.1: Chemical reactions and associated rates in Mars multi-fluid MHD Code (most of the reaction rates are adopted from *Najib et al.* (2011))

Chemical Reaction	Rate (s^{-1})
Primary Photolysis and Particle Impact	
$CO_2 + h\nu \rightarrow CO_2^+ + e^-$	1.67×10^{-6} $s^{-1}(solarmax)$
	5.52×10^{-7} $s^{-1}(solarmin)$
$CO_2 + h\nu \rightarrow CO + O^+ + e^-$	1.50×10^{-7} $s^{-1}(solarmax)$
	4.72×10^{-8} $s^{-1}(solarmin)$
$O + h\nu \rightarrow O^+ + e^-$	3.11×10^{-7} $s^{-1}(solarmax)$
	9.41×10^{-8} $s^{-1}(solarmin)$
$H + h\nu \rightarrow H^+ + e^-$	8.59×10^{-8} $s^{-1}(solarmax)$
	5.58×10^{-8} $s^{-1}(solarmin)$
Ion-Neutral Chemistry	Rate (cm^3 s^{-1})
$CO_2^+ + O \rightarrow O_2^+ + CO$	1.64×10^{-10}
$CO_2^+ + O \rightarrow O^+ + CO_2$	9.60×10^{-11}
$O^+ + CO_2 \rightarrow O_2^+ + CO$	1.1×10^{-9} $(800/T_i)^{0.39}$
$O^+ + H \rightarrow H^+ + O$	6.4×10^{-10}
$H^+ + O \rightarrow O^+ + H$	5.08×10^{-10}
Electron Recombination Chemistry	Rate ($cm^3 s^{-1}$)
$O_2^+ + e^- \rightarrow O + O$	7.38×10^{-8} $(1200/T_e)^{0.56}$
$CO_2^+ + e^- \rightarrow CO + O$	3.10×10^{-7} $(300/T_e)^{0.5}$

ionospheric chemical loss process for planets like Mars and Venus.

$$S^+ + e^- \longrightarrow A + B \tag{2.30}$$

where the products A and B may be in an excited state because the excess energy from an exothermic reaction can contribute to the kinetic energy of the products. A typical example is the dissociative recombination of O_2^+ that produces hot atomic oxygen and helps to form a hot corona around Mars.

Table 2.1 summarizes the chemical reactions and the associated rates for inelastic collisions used in our multi-fluid MHD calculations.

- **Inelastic collisions for ion species**

  Both photoionization and electron impact ionization can contribute to the source of an ion species s, whereas the recombination has the opposite effect to

reduce the amount of ion species s. As for charge exchange, it will be either a loss or source term for species s depending on whether the species is a reactant or a product. These three effects can be formalized as follows:

$$\left(\frac{\delta F_s\left(\mathbf{r_s},\mathbf{v_s},t\right)}{\delta t}\right)_{ionization} = \left(\nu_{ph,s'}+\nu_{imp,s'}\right) n_{s'} f_{s'}\left(\mathbf{r_s},\mathbf{v_s},t\right) \quad (2.31)$$

$$\left(\frac{\delta F_s\left(\mathbf{r_s},\mathbf{v_s},t\right)}{\delta t}\right)_{recombination} = -\alpha_{R,s}\, n_e F_s\left(\mathbf{r_s},\mathbf{v_s},t\right) \quad (2.32)$$

$$\begin{aligned}\left(\frac{\delta F_s\left(\mathbf{r_s},\mathbf{v}_s,t\right)}{\delta t}\right)_{charge-exchange} &= -\sum_{t'=neutrals} k_{st'} n_{t'} n_s f_s\left(\mathbf{r_s},\mathbf{v}_s,t\right) \\ &+ \sum_{i=ions} k_{is'} n_i n_{s'} f_{s'}\left(\mathbf{r_s},\mathbf{v}_s,t\right) \quad (2.33)\end{aligned}$$

where $\nu_{ph,s}$ and $\nu_{imp,s}$ are the photoionization and the impact ionization frequencies, respectively. $n_{s'}$ and $f_{s'}\left(\mathbf{r_s},\mathbf{v_s},t\right) = F_{s'}\left(\mathbf{r_s},\mathbf{v_s},t\right)/n_{s'}$ denote the density and the normalized distribution function of the neutral species s'. $\alpha_{[R,s]}$ represents the recombination rate based upon the total electron density n_e. $k_{st'}$ and $k_{is'}$ are charge exchange rates. The first and the second term in Equation (2.33) corresponds to loss of species s due to charge exchange between ion species s and neutral species t' and creation of new s species by charge exchange between s' and ion species i, respectively.

Combining all the inelastic collision terms in Equations (2.31-2.33), we get,

$$\begin{aligned}\left(\frac{\delta F_s\left(\mathbf{r_s},\mathbf{v}_s,t\right)}{\delta t}\right)_{inelastic} &= \left(\frac{\delta F_s\left(\mathbf{r},\mathbf{v}_s,t\right)}{\delta t}\right)_{ionization} + \left(\frac{\delta F_s\left(\mathbf{r},\mathbf{v}_s,t\right)}{\delta t}\right)_{recombination} \\ &+ \left(\frac{\delta F_s\left(\mathbf{r},\mathbf{v}_s,t\right)}{\delta t}\right)_{charge-exchange} \\ &= \left(\nu_{ph,s'}+\nu_{imp,s'}+\sum_{i=ions} k_{is'} n_i\right) n_{s'} f_{s'}\left(\mathbf{r},\mathbf{v}_s,t\right) \\ &- \left(\alpha_{R,s} n_e + \sum_{t'=neutrals} k_{st'} n_{t'}\right) n_s f_s\left(\mathbf{r},\mathbf{v}_s,t\right) \quad (2.34)\end{aligned}$$

Before we go to inelastic collisions for electron species, let us summarize the

corresponding transfer integrals for inelastic collisions:

$$
\begin{aligned}
m_s\left(\frac{\delta n_s}{\delta t}\right)_{inelastic} &= m_s n_{s'}\left(\nu_{ph,s'}+\nu_{imp,s'}+\sum_{i=ions}k_{is'}n_i\right) \\
&- m_s n_s\left(\alpha_{R,s}n_e+\sum_{t'=neutrals}k_{st'}n_{t\prime}\right) \qquad (2.35)\\
\left(\frac{\delta M_s}{\delta t}\right)_{inelastic} &= m_s n_{s'}\left(\nu_{ph,s'}+\nu_{imp,s'}+\sum_{i=ions}k_{is'}n_i\right)(\mathbf{u_{s0}}-\mathbf{u_s}) \qquad (2.36)\\
\left(\frac{\delta E_s}{\delta t}\right)_{inelastic} &= \frac{1}{\gamma-1}n_{s'}kT_{s0}\left(\nu_{ph,s'}+\nu_{imp,s'}+\sum_{i=ions}k_{is'}n_i\right) \\
&+ \frac{1}{2}m_s n_{s'}\left(\nu_{ph,s'}+\nu_{imp,s'}+\sum_{i=ions}k_{is'}n_i\right)(\mathbf{u_{s0}}-\mathbf{u_s})^2 \\
&- \frac{1}{\gamma-1}n_s kT_s\left(\alpha_{R,s}n_e+\sum_{t'=neutrals}k_{st'}n_{t\prime}\right) \qquad (2.37)
\end{aligned}
$$

where T_{s0} and $\mathbf{u_{s0}}$ are respectively the temperature and bulk velocity of neutral species s'. In the current version of the model, we assume $\mathbf{u_{s0}}$=0, indicating we ignore the neutral wind effect. The recent study by *Brecht and Ledvina* (2014b) shows the neutral winds play an important role in the ion escape process. We plan to study the neutral wind effects in the near future. For conciseness, we write the production and loss rates of ion species s as $\mathcal{S}_s$ and $\mathcal{L}_s$:

$$
\begin{aligned}
\mathcal{S}_s &= m_s n_{s'}\left(\nu_{ph,s'}+v_{imp,s'}+\sum_{i=ions}k_{is'}n_i\right) \qquad (2.38)\\
\mathcal{L}_s &= m_s n_s\left(\alpha_{R,s}n_e+\sum_{t'=neutrals}k_{st'}n_{t\prime}\right) \qquad (2.39)
\end{aligned}
$$

which leads to:

$$m_s \left(\frac{\delta n_s}{\delta t}\right)_{inelastic} = \mathcal{S}_s - \mathcal{L}_s \tag{2.40}$$

$$\left(\frac{\delta M_s}{\delta t}\right)_{inelastic} = \mathcal{S}_s \left(\mathbf{u_{s0}} - \mathbf{u_s}\right) \tag{2.41}$$

$$\left(\frac{\delta E_s}{\delta t}\right)_{inelastic} = \frac{k}{\gamma - 1}\frac{\mathcal{S}_s T_n - \mathcal{S}_L T_s}{m_s} + \frac{1}{2}\mathcal{S}_s \left(\mathbf{u_{s0}} - \mathbf{u_s}\right)^2 \tag{2.42}$$

- **Inelastic collisions for electron species**

  With a similar procedure, we can investigate the effect of inelastic collisions on the distribution function of electrons. Except for the charge exchange reactions, all the ionization and recombination reactions contribute to the evolution of the electron distribution function. Therefore, we are left with

$$\left(\frac{\delta F_e\left(\mathbf{r}, \mathbf{v}_e, t\right)}{\delta t}\right)_{inelastic} = \left(\frac{\delta F_e\left(\mathbf{r}, \mathbf{v}_e, t\right)}{\delta t}\right)_{ionization} + \left(\frac{\delta F_e\left(\mathbf{r}, \mathbf{v}_e, t\right)}{\delta t}\right)_{recombination} \tag{2.43}$$

$$= \sum_{s'} \left(\nu_{ph,s'} + \nu_{imp,s'}\right) n_{s'} f_{s'}\left(\mathbf{r}, \mathbf{v}_e, t\right) \tag{2.44}$$

$$- \sum_{s=ions} \alpha_{R,s} n_e n_s f_e\left(\mathbf{r}, \mathbf{v}_e, t\right) \tag{2.45}$$

  Finally, by writing the production and loss rates of the electrons, $\mathcal{S}_e$ and $\mathcal{L}_e$, as:

$$\mathcal{S}_e = m_e \sum_{s'} \left(\nu_{ph,s'} + \nu_{imp,s'}\right) n_{s'} \tag{2.46}$$

$$\mathcal{L}_e = m_e n_e \sum_{s'=ions} \alpha_{R,s} n_s \tag{2.47}$$

we get the concise form of the integrals for inelastic collisions of electrons:

$$m_e \left(\frac{\delta n_s}{\delta t}\right)_{inelastic} = \mathcal{S}_e - \mathcal{L}_e \tag{2.48}$$

$$\left(\frac{\delta M_s}{\delta t}\right)_{inelastic} = \mathcal{S}_e \left(\mathbf{u_{s0}} - \mathbf{u_e}\right) \tag{2.49}$$

$$\left(\frac{\delta E_s}{\delta t}\right)_{inelastic} = \frac{k}{\gamma - 1}\frac{\mathcal{S}_e T_{s0} - \mathcal{L}_e T_e}{m_e} + \frac{1}{2}\mathcal{S}_e \left(\mathbf{u_{s0}} - \mathbf{u_e}\right)^2 \tag{2.50}$$

2.1.3 Summary of the Transport Equation

Combining the terms from both elastic and inelastic collisions, we obtain the complete form of the transport equations for both ions and electrons:

- **Transport equations for ion species**

  The ion transport equations for species s can be summarized as follows:

$$\frac{\partial \rho_s}{\partial t} + \nabla \cdot \left(\rho_s \mathbf{u_s}\right) = \mathcal{S}_s - \mathcal{L}_s \tag{2.51}$$

$$\begin{aligned} \rho_s \frac{\partial \mathbf{u_s}}{\partial t} + \rho_s \left(\mathbf{u_s} \cdot \nabla\right) \mathbf{u_s} + \nabla p_s - \rho_s \mathbf{G} - n_s q_s \left(\mathbf{E} + \mathbf{u_s} \times \mathbf{B}\right) = \\ \rho_s \sum_{t=all} \nu_{st} \left(\mathbf{u_t} - \mathbf{u_s}\right) + \mathcal{S}_s \left(\mathbf{u_{s0}} - \mathbf{u_s}\right) \end{aligned} \tag{2.52}$$

$$\begin{aligned} \frac{1}{\gamma - 1}\frac{\partial p_s}{\partial t} + \frac{1}{\gamma - 1}\left(\mathbf{u_s} \cdot \nabla\right) p_s + \frac{\gamma}{\gamma - 1} p_s \left(\nabla \cdot \mathbf{u_s}\right) + \left(\nabla \cdot \mathbf{h_s}\right) = \\ \sum_{t=all} \frac{\rho_s \nu_{st}}{m_s + m_t}\left[3k\left(T_t - T_s\right) + m_t \left(\mathbf{u_t} - \mathbf{u_s}\right)^2\right] + \\ \frac{k}{\gamma - 1}\frac{\mathcal{S}_s T_{s0} - \mathcal{L}_s T_s}{m_s} + \frac{1}{2} S_s \left(\mathbf{u_{s0}} - \mathbf{u_s}\right)^2 \end{aligned} \tag{2.53}$$

where $\rho_s = m_s n_s$. Assuming that neutral velocity and temperature are the same for all enutral species, i.e., $T_{s0} = T_n$ and $\mathbf{u_{s0}} = \mathbf{u_n}$, we are left with:

$$\frac{\partial \rho_s}{\partial t} + \nabla \cdot (\rho_s \mathbf{u_s}) = \mathcal{S}_s - \mathcal{L}_s \tag{2.54}$$

$$\begin{aligned} \rho_s \frac{\partial \mathbf{u_s}}{\partial t} + \rho_s (\mathbf{u_s} \cdot \nabla) \mathbf{u_s} + \nabla p_s - \rho_s \mathbf{G} - n_s q_s (\mathbf{E} + \mathbf{u_s} \times \mathbf{B}) = \\ \rho_s \sum_{t=all} \nu_{st} (\mathbf{u_t} - \mathbf{u_s}) + \mathcal{S}_s (\mathbf{u_n} - \mathbf{u_s}) \end{aligned} \tag{2.55}$$

$$\begin{aligned} \frac{1}{\gamma - 1} \frac{\partial p_s}{\partial t} + \frac{1}{\gamma - 1} (\mathbf{u_s} \cdot \nabla) p_s + \frac{\gamma}{\gamma - 1} p_s (\nabla \cdot \mathbf{u_s}) + (\nabla \cdot \mathbf{h_s}) = \\ \sum_{t=ion} \frac{\rho_s \nu_{st}}{m_s + m_t} \left[3k (T_t - T_s) + m_t (\mathbf{u_t} - \mathbf{u_s})^2 \right] + \\ \frac{\rho_s \nu_{sn}}{m_s + m_n} \left[3k (T_n - T_s) + m_n (\mathbf{u_n} - \mathbf{u_s})^2 \right] + \\ \frac{k}{\gamma - 1} \frac{\mathcal{S}_s T_n - \mathcal{L}_s T_s}{m_s} + \frac{1}{2} S_s (\mathbf{u_n} - \mathbf{u_s})^2 \end{aligned} \tag{2.56}$$

- **Transport equations for electron species**

  Similarly, we summarize the transport equations for electrons as follows:

$$\frac{\partial \rho_e}{\partial t} + \nabla \cdot (\rho_e \mathbf{u_e}) = \mathcal{S}_e - \mathcal{L}_e \tag{2.57}$$

$$\begin{aligned} \rho_e \frac{\partial \mathbf{u_e}}{\partial t} + \rho_e (\mathbf{u_e} \cdot \nabla) \mathbf{u_e} + \nabla p_e - \rho_e \mathbf{G} + e n_e (\mathbf{E} + \mathbf{u_e} \times \mathbf{B}) = \\ \rho_e \sum_{t=all} \nu_{et} (\mathbf{u_t} - \mathbf{u_e}) + \mathcal{S}_e (\mathbf{u_n} - \mathbf{u_e}) \end{aligned} \tag{2.58}$$

$$\begin{aligned} \frac{1}{\gamma - 1} \frac{\partial p_e}{\partial t} + \frac{1}{\gamma - 1} (\mathbf{u_e} \cdot \nabla) p_e + \frac{\gamma}{\gamma - 1} p_e (\nabla \cdot \mathbf{u_e}) + (\nabla \cdot \mathbf{h_e}) = \\ \sum_{t=all} \frac{\rho_e \nu_{et}}{m_e + m_t} \left[3k (T_t - T_e) + m_t (\mathbf{u_t} - \mathbf{u_e})^2 \right] + \\ \frac{k}{\gamma - 1} \frac{\mathcal{S}_e T_n - \mathcal{L}_e T_e}{m_e} + \frac{1}{2} S_e (\mathbf{u_n} - \mathbf{u_e})^2 \end{aligned} \tag{2.59}$$

Given the commonly used quasi-neutrality assumption in a plasma, the electron

fluid continuity equation can be simply replaced by

$$n_e = \sum_{s=ions} Z_s n_s \tag{2.60}$$

From the current, $\mathbf{j}$, expression, we can get the electron fluid velocity

$$\mathbf{u_e} = \mathbf{u}_+ - \frac{\mathbf{J}}{en_e} \tag{2.61}$$

where $\mathbf{u}_+$ is the charge averaged velocity,

$$\mathbf{u}_+ = \sum_{s=ions} \frac{q_s n_s u_s}{en_e} \tag{2.62}$$

Therefore, we only need to solve the electron pressure equation:

$$\begin{aligned} \frac{1}{\gamma-1}\frac{\partial p_e}{\partial t} + \frac{1}{\gamma-1}\left(\mathbf{u_e}\cdot\nabla\right)p_e + \frac{\gamma}{\gamma-1}p_e\left(\nabla\cdot\mathbf{u_e}\right) + \left(\nabla\cdot\mathbf{h_e}\right) = \\ \sum_{t=all}\frac{\rho_e\nu_{et}}{m_e+m_t}\left[3k\left(T_t-T_e\right)+m_t\left(\mathbf{u_t}-\mathbf{u_e}\right)^2\right] + \\ \frac{k}{\gamma-1}\frac{\mathcal{S}_e T_n - \mathcal{L}_e T_s}{m_e} + \frac{1}{2}S_e\left(\mathbf{u_n}-\mathbf{u_e}\right)^2 \end{aligned} \tag{2.63}$$

If we assume $m_e \approx 0$, the contributions of electron-ion and electron-neutral collisions in the electron momentum and pressure transport equations are negligible with respect to the other terms. So we will ignore the term $\propto \ m_e\left(\mathbf{u_i}-\mathbf{u_e}\right)^2$ in our calculation. In most of this thesis (except in Chapter VII), we assume $p_e = \sum_s p_s$ and ignore the heat conduction. It is also interesting to mention that by assuming $m_e \approx 0$, the electron momentum equation can be simplified as:

$$\nabla p_e + en_e\left(\mathbf{E}+\mathbf{u_e}\times\mathbf{B}\right) = 0 \tag{2.64}$$

The same electron massless treatment that leads to Equation (2.64) gives Equa-

tion (3) in *Winske et al.* (2003) for a hybrid code.

2.1.4 Multi-Fluid MHD Equations

In the rest of this chapter, we derive the multi-fluid MHD equations we used in our calculation. Equation (2.64) can be rearranged as

$$\mathbf{E} = -\frac{\nabla p_e}{en_e} - \mathbf{u_e} \times \mathbf{B} \tag{2.65}$$

Substituting $\mathbf{u_e} = \mathbf{u}_+ - \frac{\mathbf{J}}{en_e}$ into Equation (2.65), we get

$$\mathbf{E} = -\frac{\nabla p_e}{en_e} - (\mathbf{u}_+ - \frac{\mathbf{J}}{en_e}) \times \mathbf{B} \tag{2.66}$$

In order to eliminate the electric field, $\mathbf{E}$, in the ion momentum equation, we substitute Equation (2.66) into Equation (2.55), which leads to

$$\frac{\partial p_s \mathbf{u_s}}{\partial t} + \nabla \cdot (\rho_s \mathbf{u_s} \mathbf{u_s} + I p_s) = n_s q_s (\mathbf{u_s} - \mathbf{u}_+) \times \mathbf{B} + \frac{q_s n_s}{en_e} (\mathbf{J} \times \mathbf{B} - \nabla p_e) + \mathcal{S}_{p_s \mathbf{u_s}} \tag{2.67}$$

where $\mathcal{S}_{p_s \mathbf{u_s}}$ is the source term related to collisions. Due to the existence of $\frac{q_s n_s}{en_e}(\mathbf{J} \times \mathbf{B} - \nabla p_e)$, the multi-fluid equation cannot be written in conservative form (*Tóth et al.*, 2012).

By substituting Equation (2.65) into Faraday's law

$$\frac{\partial \mathbf{B}}{\partial t} = -(\nabla \times \mathbf{E}) \tag{2.68}$$

we obtain

$$\frac{\partial \mathbf{B}}{\partial t} - \nabla \times (\mathbf{u_e} \times \mathbf{B} + \frac{\nabla p_e}{n_e}) = 0 \tag{2.69}$$

By neglecting the electron pressure gradient and Hall term $\frac{J}{en_e}$ with appropriate as-

sumptions, Equation (2.69) is reduced to

$$\frac{\partial \mathbf{B}}{\partial t} - \nabla \times (\mathbf{u}_+ \times \mathbf{B}) = 0 \tag{2.70}$$

It is noteworthy that for most of this thesis, the electron pressure source terms will be accounted for in the individual ion energy equations. We finally summarize the multi-fluid equation as follows (similar to those shown in *Najib et al.* (2011)):

$$\begin{aligned}
\frac{\partial \rho_s}{\partial t} + \nabla \cdot (\rho_s \mathbf{u_s}) &= \mathcal{S}_s - \mathcal{L}_s & (2.71)\\
\frac{\partial \rho_s \mathbf{u_s}}{\partial t} + \nabla \cdot (\rho_s \mathbf{u_s} \mathbf{u_s} + p_s \vec{\vec{I}}) &= n_s q_s (\mathbf{u_s} - \mathbf{u}_+) \times \mathbf{B} + \frac{q_s n_s}{e n_e} (\frac{\nabla \times \mathbf{B}}{\mu_\mathbf{0}} \times \mathbf{B} - \nabla p_e) + \rho_s \mathbf{G} \\
&+ \rho_s \sum_{t=all} \nu_{st} (\mathbf{u_t} - \mathbf{u_s}) + \mathcal{S}_s \times \mathbf{u_n} - \mathcal{L}_s \times \mathbf{u_s} & (2.72)\\
\frac{1}{\gamma - 1} \frac{\partial p_s}{\partial t} + \frac{1}{\gamma - 1} (\mathbf{u_s} \cdot \nabla) p_s &= -\frac{\gamma}{\gamma - 1} p_s (\nabla \cdot \mathbf{u_s}) \\
&+ \sum_{t=ion} \frac{\rho_s \nu_{st}}{m_s + m_t} \left[3k (T_t - T_s) + m_t (\mathbf{u_t} - \mathbf{u_s})^2 \right] \\
&+ \frac{\rho_s \nu_{sn}}{m_s + m_n} \left[3k (T_n - T_s) + m_n (\mathbf{u_n} - \mathbf{u_s})^2 \right] \\
&+ \frac{k}{\gamma - 1} \frac{\mathcal{S}_s T_n - \mathcal{L}_s T_s}{m_s} + \frac{1}{2} S_s (\mathbf{u_n} - \mathbf{u_s})^2 \\
&+ \frac{n_s}{n_e} \frac{k}{\gamma - 1} \frac{\mathcal{S}_e T_n - \mathcal{L}_e T_e}{m_e} \\
\frac{\partial \mathbf{B}}{\partial t} &= \nabla \times (\mathbf{u}_+ \times \mathbf{B}) & (2.73)
\end{aligned}$$

with

$$\begin{aligned}
\mathcal{S}_s &= m_s n_{s'} \left(\nu_{ph,s'} + \nu_{imp,s'} + \sum_{i=ions} k_{is'} n_i \right) & (2.74)\\
\mathcal{L}_s &= m_s n_s \left(\alpha_{R,s} n_e + \sum_{t'=neutrals} k_{st'} n_{t'} \right) & (2.75)\\
\mathcal{S}_e &= m_e \sum_{s'} (\nu_{ph,s'} + \nu_{imp,s'}) n_{s'} & (2.76)\\
\mathcal{L}_e &= m_e n_e \sum_{s=ions} \alpha_{R,s} n_s & (2.77)
\end{aligned}$$

CHAPTER III

Solar wind interaction with Mars upper atmosphere during current and ancient times: Results from the one-way coupling between the multi-fluid MHD model and the M-TGCM model

3.1 Introduction

The 3-D multi-fluid BATS-R-US MHD code (MF-MHD) is coupled with the 3-D Mars Thermospheric General Circulation Model (M-TGCM). The ion escape rates from the Martian upper atmosphere during current and ancient times are investigated by using a one-way coupling approach, i.e., the MF-MHD model incorporates the 3-D neutral atmosphere profiles from the M-TGCM model. The calculations are carried out for three cases with different solar cycle conditions for the current epoch. The calculated total ion escape rate (the sum of three major ionospheric species, O^+, O_2^+ and CO_2^+) for solar cycle maximum conditions (6.6×10^{24} s^{-1}) is about 2.6 times larger than that of solar cycle minimum conditions (2.5×10^{24} s^{-1}). Our simulation results show good agreement with recent observations of $2 \sim 3 \times 10^{24}$ s^{-1} (O^+, O_2^+ and CO_2^+) measured near solar cycle minimum conditions by Mars Express (MEX). We also simulate an extremely high solar wind condition that aims to mimic the

condition of Interplanetary coronal mass ejections (ICMEs) or corotating interaction regions (CIRs) passing Mars. Simulation results show that it can lead to a significant value of the escape rate as large as 4.3×10^{25} s^{-1}. For the ancient Mars studies, we investigate three cases that correspond to: present day (denoted by Epoch 1), 2.7 billion years (Gyr) ago (Epoch 2), and 3.5 $\pm$ 0.1 Gyr ago (Epoch 3). The net ion escape rate at Epoch 3 can reach 1.2×10^{26} s^{-1} that is two orders of magnitude larger than that of current solar minimum conditions.

The study of the solar wind-Mars interaction and the resulting ion loss has received a great deal of attention during the last decade due to its potential impact on the long-term evolution of Mars atmosphere (e.g., loss of water) over its history. In this chapter, we adopt the 3-D Mars neutral atmosphere profiles (i.e., neutral atmosphere temperatures T_n, neutral densities N_O, N_{CO_2}, photoionization frequencies I_O, I_{CO_2} as shown in Fig. 3.2) from the M-TGCM model and one-way couple it with the MF-MHD model that solves separate momentum and energy equations for each ion species (*Powell et al.*, 1999; *Glocer et al.*, 2009; *Najib et al.*, 2011; *Tóth et al.*, 2012). It is noteworthy that we use 1-D hot O profiles from *Kim et al.* (1998) for the current epoch studies while adopting 3-D hot O from *Lee et al.* (2014c) for the ancient Mars studies. We compare the simulation results with the currently available observational data for the current epoch studies.

3.2 Model Description

The M-TGCM model is a finite difference primitive equation model that self-consistently solves for time-dependent neutral temperatures, neutral-ion densities, and three component neutral winds over the Mars globe [e.g., *Bougher et al.*, 2000, 2006, 2008, 2009]. The modern M-TGCM code contains prognostic equations for the major neutral species (CO_2, CO, N_2, and O), selected minor neutral species (Ar, NO, $N(^4S)$, O_2), and several photochemically produced ions (O_2^+, CO_2^+, O^+, CO^+,

and NO^+). The latitude-longitude resolution is $5 \times 5°$. The vertical coordinate is log pressure with a resolution equaling to 0.5 scale heights (which is about 5 km in the Martian lower thermosphere). All fields are calculated on 33 pressure levels above 1.32 μbar, corresponding to altitudes from roughly 70 to 300 km (at solar maximum conditions). The M-TGCM model is thermally and dynamically coupled with the NASA Ames Mars General Circulation Model ($5° \times 5°$ grid) (*McDunn et al.*, 2010). The E10.7 or F10.7-cm index (solar EUV/UV flux variation), the heliocentric distance and solar declination corresponding to Mars seasons are the key adjustable parameters in the model that can be varied for investigating different M-TGCM cases. A fast non-local thermodynamic equilibrium (N-LTE) 15-μm cooling scheme is implemented in the M-TGCM, dynamically dependent upon simulated atomic O abundances, along with corresponding near-IR heating rates *Bougher et al.* (2006). The model is constrained by observations from MGS (Mars Global Surveyor), Mars Odyssey and MRO (Mars Reconnaissance Orbiter) [see *Bougher et al.*, 2008]. Figure 3.1 shows the neutral temperature T_n, cold neutral O and CO_2 number densities at altitude of 100 km for Case 1 (also Epoch 1 later) from M-TGCM. Compared with O density distribution, CO_2 densities are larger on the dayside because CO_2 is mainly controlled by the temperature structure (instead of large scale dynamics) due to the relatively large CO_2 mass. Note in Figure 3.1, local time LT=12 is at longitude=180 instead of longitude=0. We will describe the 3-D M-AMPS (Mars Adaptive Mesh Particle Simulator) in Chapter IV when we discuss the one-way coupling work with both M-AMPS and M-GITM (Mars Global Ionosphere Thermosphere Model).

In order to one-way couple the M-TGCM model with the MF-MHD model, we initialize the latter (from 100 km to 5 R_M, where R_M is the radius of Mars $\sim$ 3396 km) with the 3-D neutral profiles (i.e., T_n, N_O, N_{CO_2}, I_O, I_{CO_2}). The equinox season (Ls = 180°) for both solar minimum (F10.7 = 70) and solar maximum (F10.7 = 200) conditions is considered. Since both models are built on spherical coordinates,

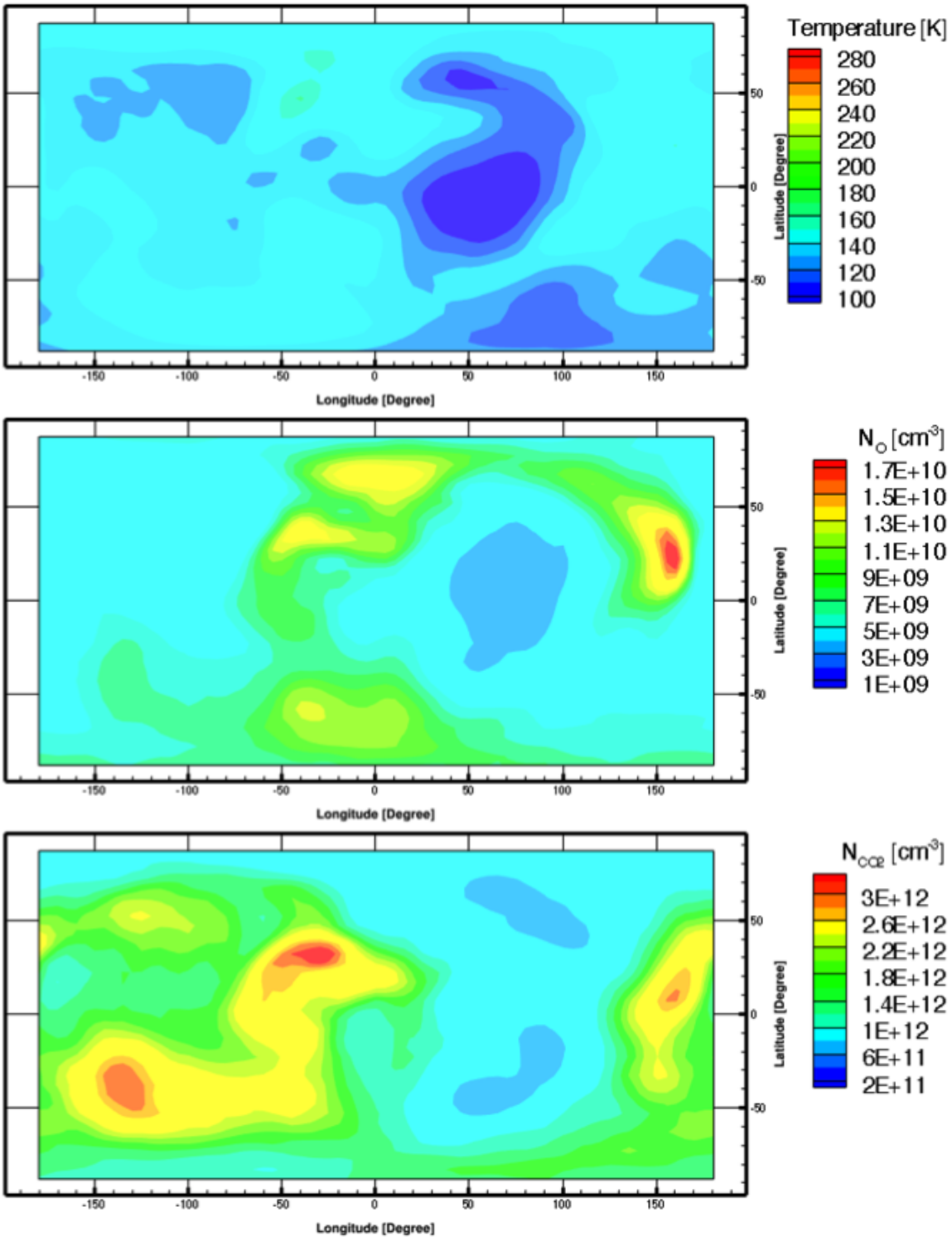

Figure 3.1: Neutral temperature T_n, cold neutral O and CO_2 densities at altitude of 100 km for Case 1 (also Epoch 1) from M-TGCM. Note that local time LT=12 is at longitude=180 instead of longitude=0.

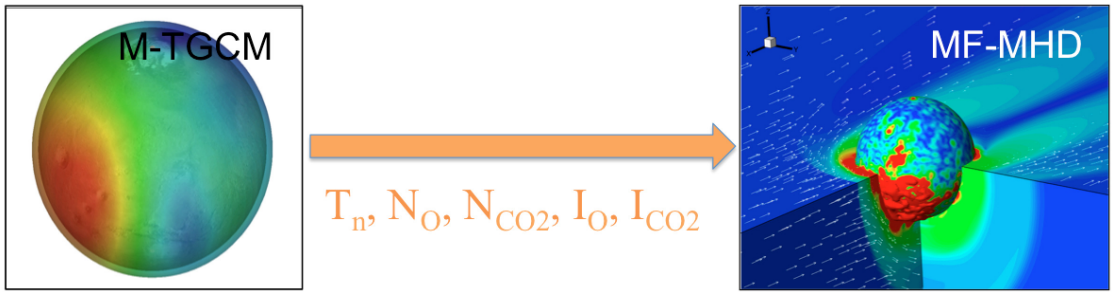

Figure 3.2: A sketch (cartoon) of a one-way coupling approach between the M-TGCM and MF-MHD models. The notation T_n denotes neutral atmosphere temperatures, N_O, N_{CO_2} are the neutral O and CO_2 number densities, and I_O, I_{CO_2} are the photoionization frequencies.

we can linearly interpolate the cell value from one to the other in the overlapping domains of each model (100 km - 250 km). From 250 km to 5 R_M, we assume constant neutral temperature and photoionization frequencies based on the M-TGCM upper boundary values since these values are almost constant when approaching the M-TGCM outer boundary. For the neutral atmosphere densities, however, we use an extrapolation based upon the hydrostatic assumption which assumes the neutral atmosphere densities decrease exponentially with altitude, i.e., $n=n_0 \exp(-dz/H_s)$, where dz is the altitude change and H_s is the scale height (which depends on the gravity, neutral temperature and neutral species mass). The hot atom densities are taken from *Kim et al.* (1998) that are assumed to be spherically symmetric. We also adopted more realistic collision frequencies between species (*Schunk and Nagy*, 2009). In order to make the code run more efficiently, we use large super cells in the polar regions (*Tóth et al.*, 2012), which can accelerate the speed of model convergence, and allows larger time steps for time accurate simulations. This approach will enable us to investigate the effects of some dynamic events (such as CMEs and dust storms) on the ion escape rate in the future. Unless mentioned otherwise the other parameters are the same as those in *Najib et al.* (2011).

The MF-MHD model was described in detail in the previous paper (*Najib et al.*, 2011), thus we only briefly summarize the model. The newly developed 3-D MF-MHD (*Najib et al.*, 2011; *Dong et al.*, 2014) can better simulate the interplay between

Martian upper atmosphere and solar wind by considering the dynamics of individual ion species. In the multi-fluid formulation, we have separate continuity, momentum and energy equations for the four ion fluids H^+, O^+, O_2^+, CO_2^+. The lower boundary is set at 100 km above the Martian surface, where the O^+, O_2^+, CO_2^+ densities are taken to be the photochemical equilibrium values. Given the solar wind proton can penetrate into the ionosphere to some extent, the H^+ density at the inner boundary is set to be approximately 30% of the solar wind density, $0.3N_{sw}$. The model adopts a nonuniform, spherical grid structure with a radial resolution varying from 5 km at the lower boundary to 1000 km at the outer boundary ($\sim$ 20 Mars Radii) and with angular resolution varying from 1.5° to 3° (Figure 3.3). We choose the smallest vertical resolution as 5 km since we want to capture all the vertical structure of the neutral profiles from the M-TGCM model. The x axis in the coordinate system points from Mars toward the Sun, the rotation axis is in the $x - z$ plane, and the y axis completes the right-hand system. The computational domain is defined by -24 R_M $\leq$ X $\leq$ 8 R_M; -16 R_M $\leq$ Y,Z $\leq$ 16 R_M. A reflective inner boundary condition for the velocity $\mathbf{u}$ is used, which results in near zero velocity at the inner boundary as expected. The plasma temperature, T_p=T_i+T_e, at the inner boundary is set to be twice the value of the neutral temperature, T_n, because at that low altitude, both ions (T_i) and electrons (T_e) have roughly the same temperature as neutrals.

The upstream solar wind plasma temperatures were set to 3.5 $\times$ 10^5 K, and the interplanetary magnetic field (IMF) was assumed to be a Parker spiral in the $X - Y$ plane with an angle of 56° for the first two cases. We use the 60 degree harmonic expansion for the crustal magnetic field developed by *Arkani-Hamed* (2001) to describe the observed fields at Mars (*Acuña et al.*, 1999). The chemical reaction calculations include charge exchange, photoionization and electron impact ionization; in order to calculate the latter the model assumes that the electron temperature is half of the calculated plasma temperature and uses the ionization rates given by *Cravens*

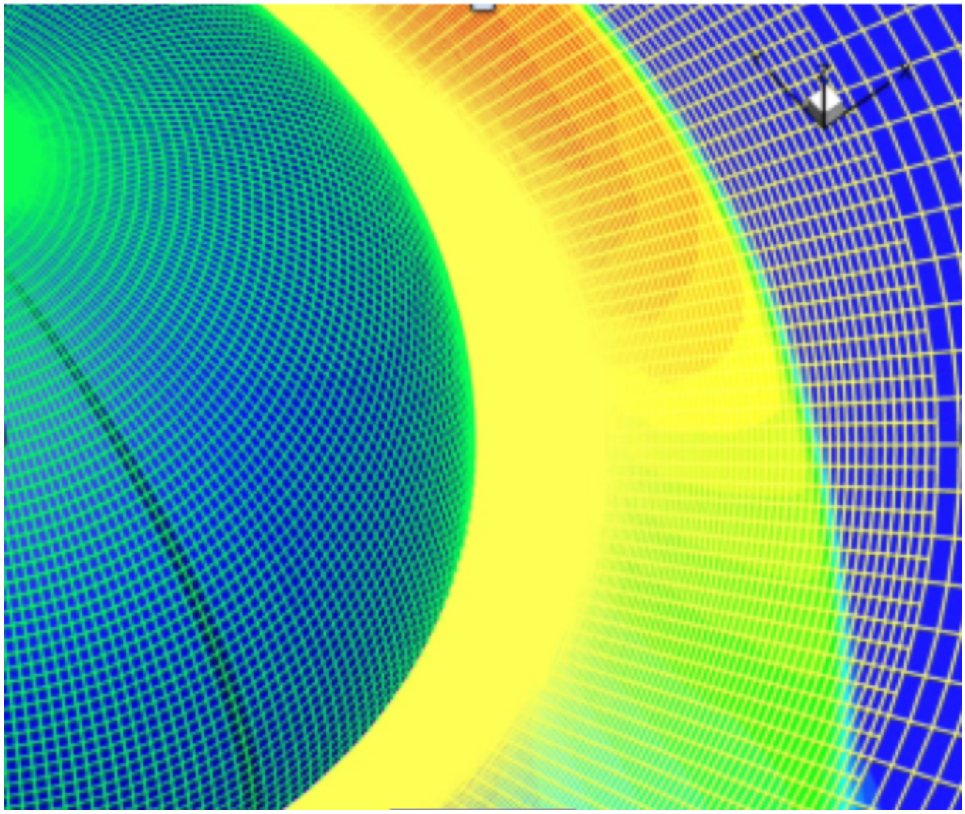

Figure 3.3: Illustration of the grid system used in the MF-MHD calculation in MSO coordinate system.

et al. (1987). We adopt the same chemical reaction schemes as *Ma and Nagy* (2007a) and *Najib et al.* (2011) in order to allow direct comparison with the multi-species model results.

3.3 Simulation Results and Discussions

3.3.1 Ion escape at the current epoch

In order to evaluate the effects of different solar radiation, interplanetary field magnitudes, solar wind density and velocity on the Mars upper atmosphere ion escape rates at the current epoch, we first study two standard cases for solar cycle minimum and solar cycle maximum conditions. A case for solar cycle maximum conditions with extremely high solar wind parameters (i.e., high solar wind velocity, strong upstream magnetic field, and large solar wind density) is also investigated to estimate the level of the enhanced ion escape rate for such an extreme space environment. Table 3.1 summarizes the parameters used for the three different cases.

Table 3.1: Input parameters used for the different calculations.

Simulation Cases	Solar Condition	Solar Wind, Density cm^{-3}	Upstream B Field	Solar Wind Velocity, km/sec	Subsolar Position‡
Case 1	Solar Minimum	4	3nT Parker Spiral	400	$180°W$ $0°N$
Case 2	Solar Maximum	4	3nT Parker Spiral	400	$180°W$ $0°N$
Case 3	Solar Maximum	20	B_y=20 nT, B_x=B_z=0	1000	$180°W$ $0°N$

‡ The crustal fields face the sun.

Compared with the multi-species MHD model (*Ma et al.*, 2004), the multi-fluid MHD model employs separate mass, momentum and energy equations for the four ion fluids (*Najib et al.*, 2011; *Dong et al.*, 2014). The differences caused by solving individual momentum and energy equations for different ion species are shown in Figure 3.4, where the main feature is the asymmetric escape plume for heavy ion species. The asymmetry is primarily caused by different Lorentz forces acting on each ion species. Figure 3.4 displays the comparison between O^+ ion number density

distribution, from which only the multi-fluid MHD can show the asymmetry feature. In the individual momentum equations, the MF-MHD model includes the Lorentz force $n_s q_s(\mathbf{u_s} \times \mathbf{B} + \mathbf{E})$:

$$\frac{\partial \rho_s \mathbf{u_s}}{\partial t} + \nabla \cdot \left(\rho_s \mathbf{u_s} \mathbf{u_s} + p_s \vec{\vec{I}} \right) = n_s q_s \left(\mathbf{u_s} \times \mathbf{B} + \mathbf{E} \right) + \mathcal{S}_{\rho_s u_s} \tag{3.1}$$

where ρ_s, n_s, q_s, $\mathbf{u_s}$ and p_s are the individual mass density, number density, charge, velocity and pressure of the ion species s, respectively. $\mathbf{E}$ and $\mathbf{B}$ denote the electric and magnetic fields, $\mathbf{J}$ is the current density, $\vec{\vec{I}}$ is the identity matrix, e is the electric charge and $\mathcal{S}_{\rho_s u_s}$ is the momentum source term. The electric field $\mathbf{E}$ can be calculated from the generalized Ohm's law:

$$\mathbf{E} = -\frac{\nabla p_e}{e n_e} - \mathbf{u_e} \times \mathbf{B} = -\frac{\nabla p_e}{e n_e} - \left(\mathbf{u}_+ - \frac{\mathbf{J}}{e n_e} \right) \times \mathbf{B} \tag{3.2}$$

where $\mathbf{u_e}$ and $\mathbf{u}_+ = \sum_s n_s q_s \mathbf{u_s} / (e n_e)$ are the electron fluid velocity and the charge averaged ion velocity, respectively. p_e denotes the electron pressure and the term $\mathbf{J} \times \mathbf{B} / (e n_e)$ on the right-hand side is called the *Hall term*. Substituting $\mathbf{E}$ into the ion momentum equation, we are left with

$$\frac{\partial \rho_s \mathbf{u_s}}{\partial t} + \nabla \cdot \left(\rho_s \mathbf{u_s} \mathbf{u_s} + I p_s \right) = n_s q_s \left(\mathbf{u_s} - \mathbf{u}_+ \right) \times \mathbf{B} + \frac{n_s q_s}{n_e e} \left(\mathbf{J} \times \mathbf{B} - \nabla p_e \right) + S_{\rho_s u_s} \tag{3.3}$$

It can easily be proved that $(\mathbf{u_s} - \mathbf{u}_+) \times \mathbf{B}$ term will lead to a flow asymmetry in the $X-Z$ plane, as long as the magnetic field is in the $X-Y$ plane. Thus, the plume provides a channel for ions to escape while this cannot be captured by the multi-species model. Given all the ion species are fully picked up by the solar wind eventually and ignoring the friction resulted from the source term, the characteristic spatial scale, L_g, associated with the asymmetry is controlled by the ratio $\mathrm{m_s u_{sw}} / (\mathrm{q_s B})$ via dimen-

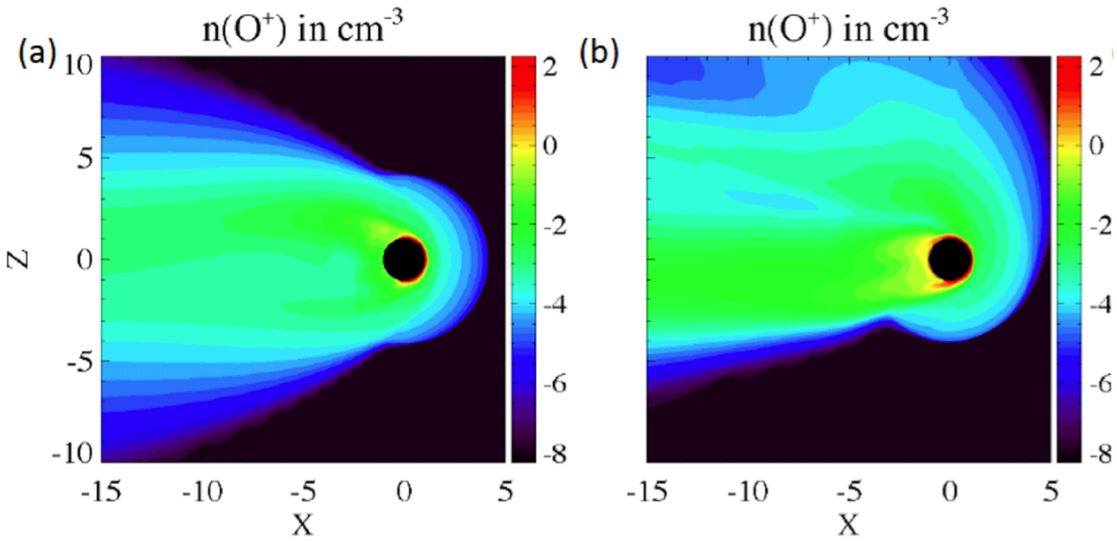

Figure 3.4: Comparison of (a) multi-species MHD and (b) multi-fluid MHD O^+ ion escape distribution in a logarithmic scale.

sional analysis. Actually, L_g is the characteristic spatial scale for the heavy ion fluid to reach the solar wind speed, u_{sw}, or to be fully picked up. Therefore, the heavier the ions are (note $q_s = e$ in the model), the more significant the escape plume is. On the other hand, from the particle simulation point of view, the asymmetry can also be explained by the induction electric field $\mathbf{E} = -\mathbf{u} \times \mathbf{B}$ (see black arrow in Figure 3.5 from *Fang et al.* (2010)). Actually, there is no essential difference between these two explanations except that in the multi-fluid code the ions of a certain species move together, while in a particle code they move individually. As long as the thermal velocity of the heavy ions is relatively small compared to their velocity relative to the magnetic field, the multi-fluid approximation is quite reasonable.

Comparing Case 1 with Case 2 (see Fig. 3.6), the escape plume is more significant for solar maximum conditions and the density close to the planet is increased. This is caused by enhanced solar radiation during solar maximum conditions which increases the amount of ions. Therefore, the ion escape rate for Case 2 should be larger than that of Case 1.

Case 3 is motivated by Pioneer Venus observations which measured very high

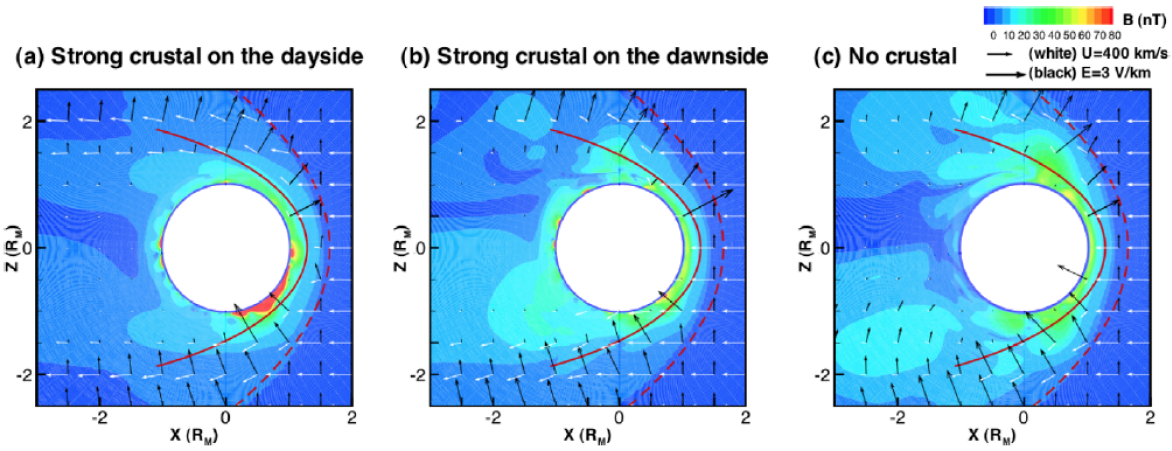

Figure 3.5: Multi-species MHD electric and magnetic fields background calculations for test particles where the magnetic field magnitude is shown by color contour, vector field of the plasma velocity is represented by white arrow, and convection electric field is displayed by black arrow in the noon-midnight plane (*Fang et al.*, 2010).

escaping ion fluxes from Venus during significantly increased solar wind pressure conditions (*Luhmann et al.*, 2007). Thus the simulation results of Case 3 may yield an estimation of ionospheric outflow during some extreme conditions such as ICMEs and CIRs. Inspection of Figure 3.6 reveals that the asymmetry in Case 3 becomes less obvious than Case 1 and Case 2 while the escape plume in the region near the Mars body becomes even stronger compared with Case 2. This is because the characteristic spatial scale, L_g, associated with the asymmetry is controlled by the ratio $m_s u_{sw}/(q_s B)$. It is worthwhile to note that the less obvious asymmetric escape plume of H^+ is caused by two factors. First, the proton mass is relatively small with respect to other heavy ion species. Second, the H^+ in the simulation is a combination of solar wind protons and Martian ionospheric protons. In principle, only the Martian ionospheric protons can make a contribution to the asymmetric escape plume due to the pickup effect, which can be found to be true by simulations separating the solar wind and ionospheric H^+ [see *Najib et al.*, 2011]. Therefore, for H^+ the asymmetric escape plume is much weaker than other heavy ion species as indicated in Figure 3.6.

We also test the effect of friction between different ion species or electromagnetic

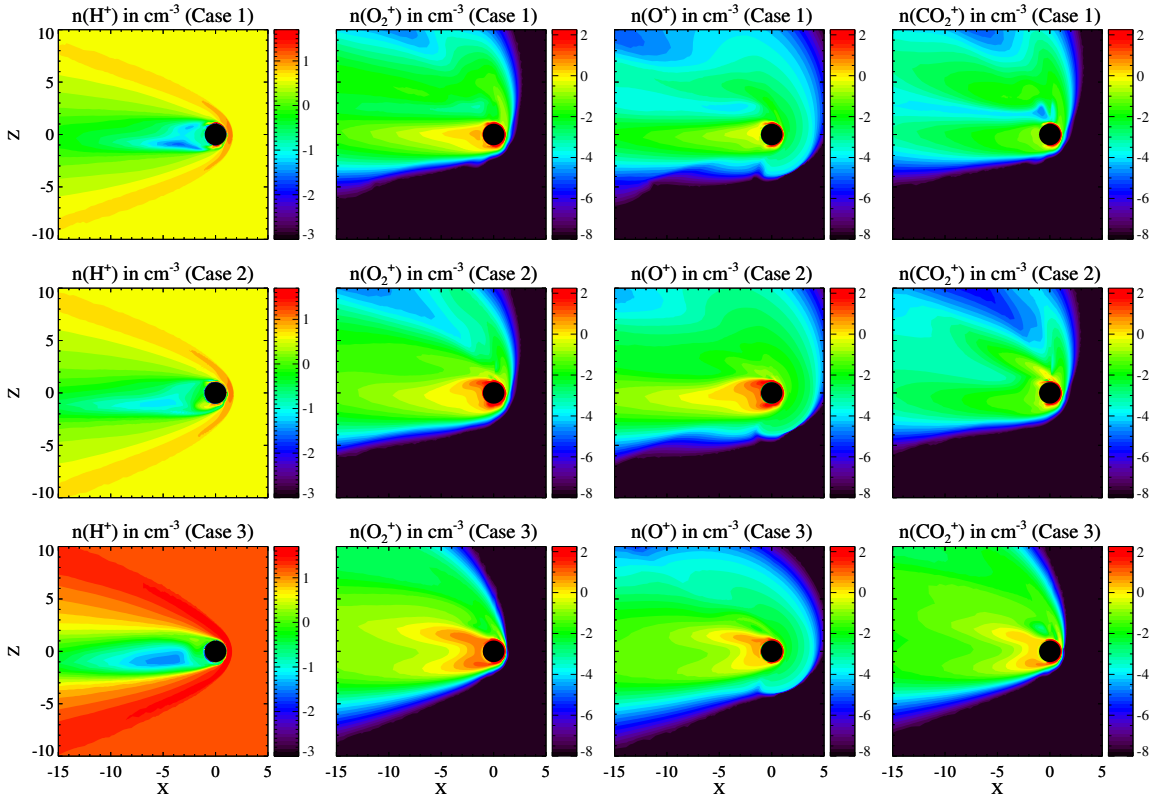

Figure 3.6: The calculated (Cases 1, 2, 3) ion number densities (no friction) in cm^{-3} in the $X-Z$ plane for H^+, O_2^+, O^+, and CO_2^+ in a logarithmic scale. Noted that the logarithmic scales in different plots are different.

ion-ion beam instabilities on the ion escape plumes. Once the velocity difference between two ion species is larger than the local Alfvén speed, $B/\sqrt{\rho\mu_0}$, a relaxation term is applied to reduce the velocity difference between different ion species (*Stockem*, 2006). Figure 3.7 illustrates the calculated ion number densities with friction. Compared with Figure 3.6, the ion escape plumes in Figure 3.7 become relatively weak. It is noteworthy that electromagnetic ion-ion beam instability is not the only kinetic instability at Mars. Technically speaking, the ion cyclotron instability is also very important at Mars due to the pickup ions from the ionosphere/exosphere and the reflected ion at the bow shock (*Gary*, 2005). The plasma and wave properties downstream of Martian bow shock has been studied by a hybrid code, focusing on the ion cyclotron instability caused by the temperature anisotropy of the reflected ion at shock front (*Dong et al.*, 2013).

We summarize the calculated ion escape rates by adopting different MHD models and neutral atmosphere profiles in Table 3.2. The calculation is conducted by integrals of the plasma density times the radial velocity component at the surface of a sphere far from the planet. In this chapter, we select the integral spherical surface to be 6 R_M since we find that the calculated ion escape rates do not change to any significant degree once the radius exceeds 4 R_M. *Lundin et al.* (2008) suggested that the total ion escape rate (O^+, O_2^+ and CO_2^+) is around 3×10^{24} s^{-1} during solar cycle minimum conditions and it may achieve values more than 10^{25} s^{-1} during the solar cycle maximum condition. *Nilsson et al.* (2011) found that the net ion escape rate for solar cycle minimum conditions is around 2×10^{24} s^{-1}. Our total ion escape rate for solar minimum conditions (Case 1) is 2.5×10^{24} s^{-1}, which is reasonably consistent with the available MEX observations. It is of particular interest to find that the calculated total ion escape rate for solar maximum conditions is about 2.6 times larger than that of solar minimum conditions, which is in good agreement with the value (~ 2.5) suggested by *Verigin et al.* (1991) and *Nilsson et al.* (2011). As we

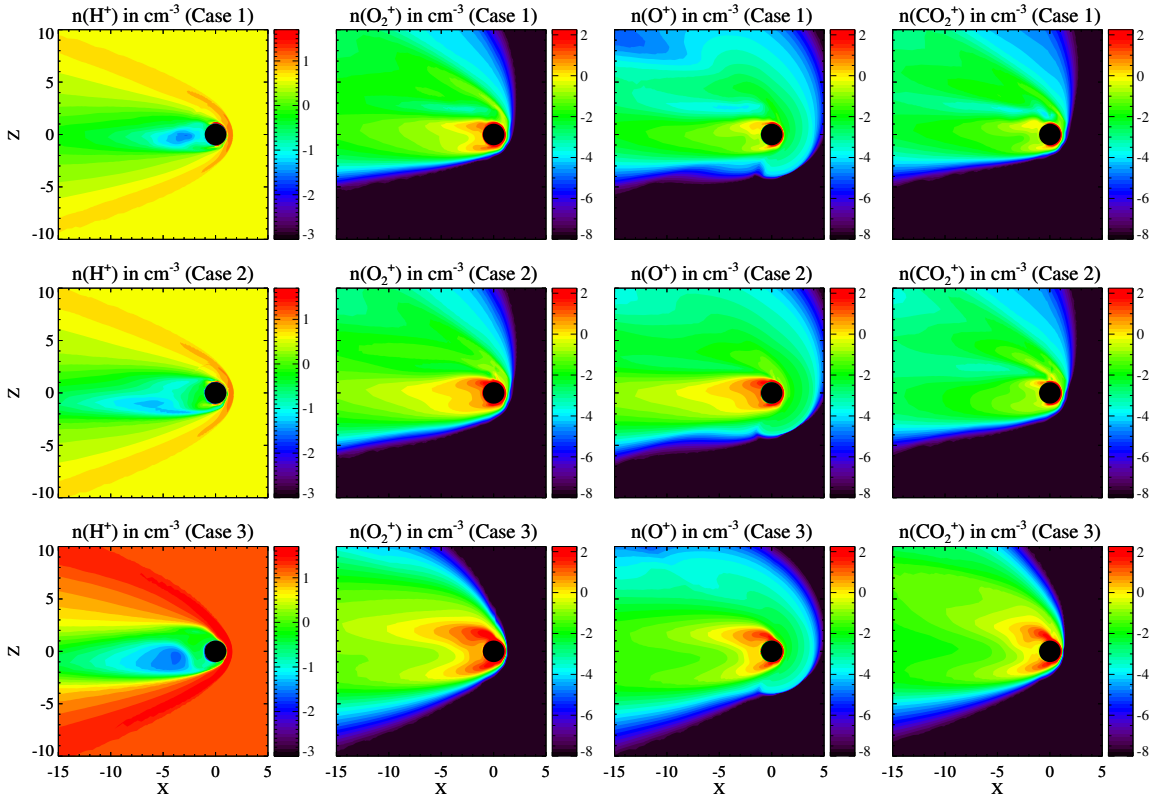

Figure 3.7: The calculated (Cases 1, 2, 3) ion number densities (with friction) in cm^{-3} in the $X-Z$ plane for H^+, O_2^+, O^+, and CO_2^+ in a logarithmic scale. Noted that the logarithmic scales in different plots are different.

expected from Figure 3.6, the total ion escape rate for extreme case (Case 3) is one order of magnitude larger than Case 1 and Case 2, and the value is on the order of 10^{25} s^{-1} which is again consistent with the value suggested by *Lundin et al.* (2008).

Table 3.2: Calculated ion escape rates (in s^{-1}).

MHD Model	Neutral Profile	Simulation Cases	O^+	O_2^+	CO_2^+	Total
multi-fluid	3-D M-TGCM	Case 1	4.2×10^{23}	1.7×10^{24}	3.5×10^{23}	2.5×10^{24}
		Case 2	3.7×10^{24}	2.5×10^{24}	3.8×10^{23}	6.6×10^{24}
		Case 3	1.0×10^{25}	2.5×10^{25}	8.2×10^{24}	4.3×10^{25}
multi-fluid‡	1-D	Case 2	7.7×10^{23}	9.0×10^{23}	1.7×10^{23}	1.84×10^{24}
multi-species†	3-D M-TGCM	Case 1	7.2×10^{23}	1.9×10^{23}	1.3×10^{23}	1.0×10^{24}
		Case 2	1.8×10^{24}	4.1×10^{23}	1.8×10^{23}	2.4×10^{24}
		Case 3	2.3×10^{25}	3.3×10^{24}	4.1×10^{24}	3.0×10^{25}

‡ The Case 2 shows the results from *Najib et al.* (2011) by adopting the 1-D spherically symmetric neutral atmosphere, where they defined the Case 2 we studied here as case 4.

† The multi-species simulation results are from *Ma and Nagy* (2007a), where they labeled the Case 1, 2, 3 we studied here as their Case 4, 6, 7.

Compared with the multi-species MHD simulation results (Table 3.2), the MF-MHD calculations show that the O^+ escape rate generally becomes smaller while the O_2^+, CO_2^+ and total escape rates increase for all three cases. One of the main reasons is that the heavy ions have a significant asymmetric ion escape plume and therefore the MF-MHD code provides a new channel for ions to escape; this feature, however, cannot be captured by the multi-species MHD model. On the other hand, the escape rate also greatly depends on the ionospheric chemical reactions in the model [refer to Table 2.1 in Chapter II], e.g., CO_2^+ is produced only from photoionization while it is consumed by three chemical reactions, indicating the CO_2^+ escape rate is less than that of O_2^+. In addition, the M-TGCM code has been improved since its output was first utilized in the multi-species MHD model of (*Ma and Nagy*, 2007a). Recent M-TGCM simulations include: (a) updated lower atmosphere forcing using dust opacity distributions from the MGS/Thermal Emission Spectrometer (*Smith*, 2004), and (b) the adoption of new solar fluxes (1.0-nm bins) from the empirically based Flare Irradiance Spectral Model (FISM) of *Chamberlin et al.* (2008) for solar minimum and maximum conditions.

3.3.2 Ion escape over Mars history

In this section, we study the solar wind interaction with Mars' upper atmosphere by employing one-way coupling between the BATS-R-US Mars multi-fluid MHD, the M-TGCM and the M-AMPS models by three selected times over the Martian history. Those correspond to: present day (denoted by Epoch 1), 2.7 Gyr ago (Epoch 2) and 3.5 $\pm$ 0.1 Gyr ago (Epoch 3). This new notation is closely related to the one used by past studies tied to the Extreme ultraviolet (EUV) flux enhancement in the past and often denoted 1 EUV, 3 EUV, 6 EUV. Epoch 1 corresponds to present day solar conditions (1EUV, 1 infrared, IR), epoch 2 corresponds to 3 times the present solar EUV flux and 0.79 times the present solar IR flux (3 EUV, 0.79 IR), and epoch 3 corresponds to 6 times the present solar EUV flux and 0.79 times the present solar IR flux (6 EUV, 0.79 IR) (*Valeille et al.*, 2010). For all these three cases, the strongest crustal source faces the sun and solar cycle minimum is adopted. Different from the previous section, here MF-MHD adopts both the 3-D M-TGCM cold neutral atmosphere (*Bougher et al.*, 2000, 2006) and 3-D M-AMPS hot oxygen corona (*Lee et al.*, 2014c) as inputs. Figure 3.8 shows the 3-D hot O for Epoch 1-3. The asymmetric feature of the 3-D hot O corona is missing in the 1-D spherically symmetric hot O profile from *Kim et al.* (1998). Epoch 1 has the weakest hot O corona and Epoch 3 has the most extensive hot O corona due to the largest solar EUV flux.

Figure 3.9 shows the calculated ion number densities (in cm^{-3}) in the $X-Z$ plane for different ion species. The top two panels are similar to those shown in Figure 3.6. The bottom panels, however, show great enhancement of O^+ and H^+ ion escape through the nightside plasma wake region. Different from Case 3 shown in Figure 3.6, the significant increase of nightside ion escape displayed in Figure 3.9 is caused by the strong solar EUV instead of high solar wind dynamic pressure. Table 3.3 summarizes the corresponding ion escape rates (in s^{-1}). The net ion escape rate

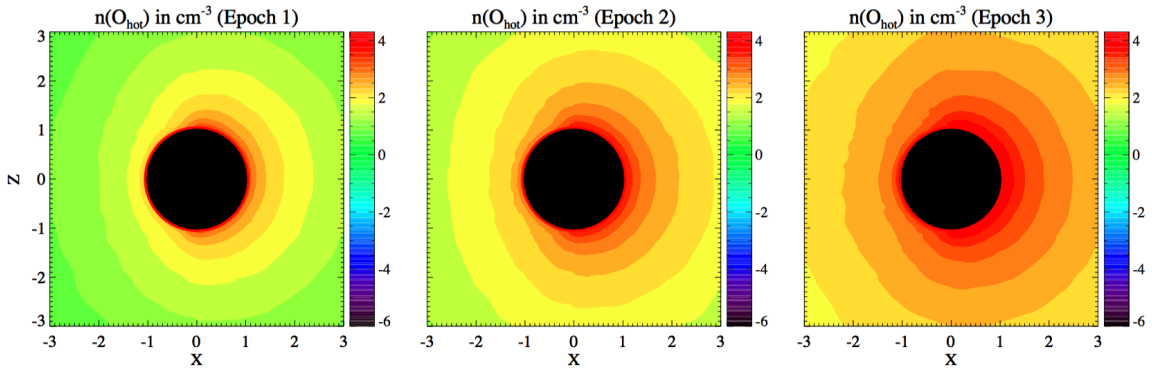

Figure 3.8: A comparison of the 3-D M-AMPS hot oxygen number density (in cm^{-3}) for Epoch 1, 2, 3. Note the use of a logarithmic scale..

at Epoch 3 can reach $\sim 10^{25}$ s^{-1} that is one order of magnitude larger than the current solar minimum conditions. Interestingly, O^+ ion loss becomes extremely important during ancient times. We can determine the integrated loss to space that has occurred through Martian history only after we have the ability to infer the ion loss rate in the past, so it is very important to study the ion escape rate from Mars at ancient times.

Table 3.3: Calculated ion escape rates (in s^{-1}).

Simulation Cases	O^+	O_2^+	CO_2^+	Total
Epoch 1	6.5×10^{23}	1.8×10^{24}	4.7×10^{23}	2.9×10^{24}
Epoch 2	3.1×10^{24}	1.6×10^{24}	3.4×10^{23}	5.0×10^{24}
Epoch 3	1.4×10^{25}	8.9×10^{23}	7.6×10^{22}	1.5×10^{25}

3.3.3 Discussion

In general, in the MF-MHD simulation, all the ion escape rates increase for the 3-D neutral inputs compared with the 1-D case (see Table 3.2). The 3-D neutral atmosphere basically changes the atmosphere temperature T_n, densities and the photoionization frequencies of neutral species O and CO_2 compared to the previous studies (*Najib et al.*, 2011). In a 3-D neutral upper atmosphere, the major Martian atmosphere components (CO_2 and O) are no longer symmetric about the planet. There exists more neutral CO_2 on the dayside than nightside (at a constant altitude) be-

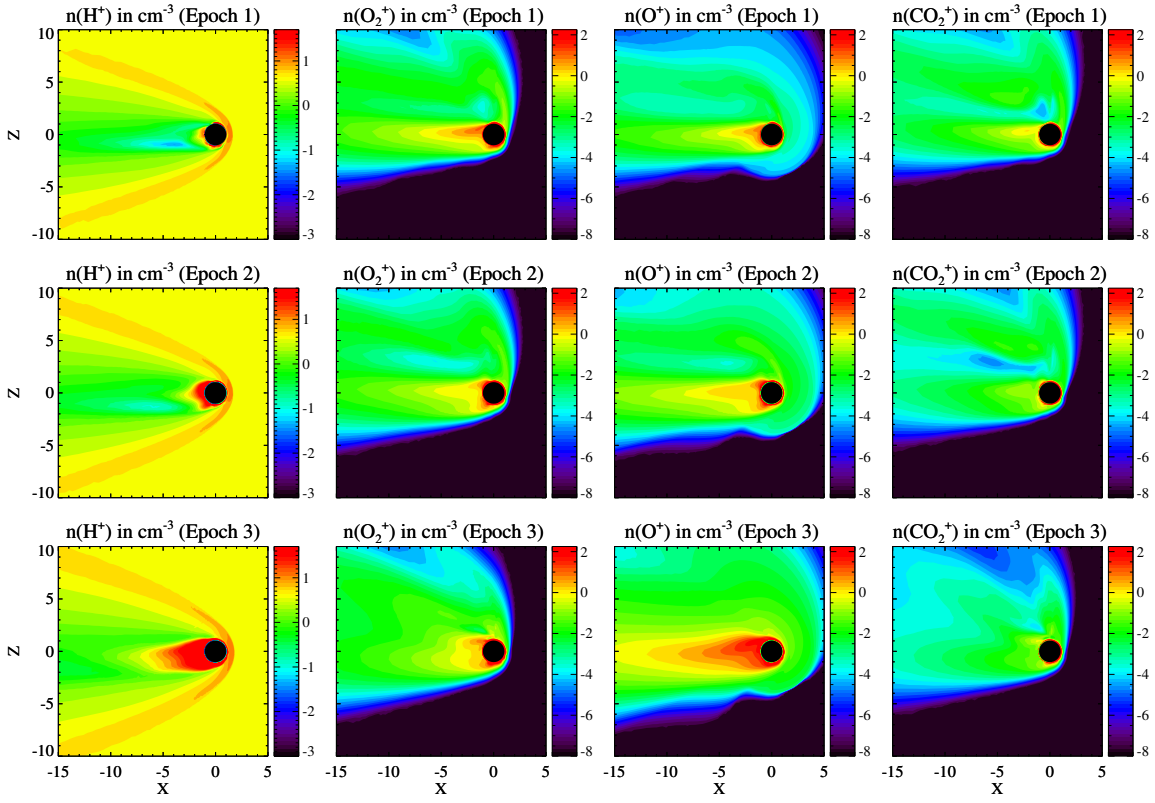

Figure 3.9: The calculated (Epoch 1, 2, 3) ion number densities in cm^{-3} in the $X-Z$ plane for H^+, O_2^+, O^+, and CO_2^+ in a logarithmic scale. Noted that the logarithmic scales in different plots are different.

cause the CO_2 global distribution is mainly controlled by the temperature structure and not global dynamics. The neutral CO_2 densities are enhanced (reduced) on the dayside (nightside) where temperatures are warmer (colder). Neutral O, however, is mainly controlled by transport due to its smaller mass. The neutral wind will transport neutral O from dayside to nightside, resulting in a bulge of neutral O in the nightside upper atmosphere. Hence, it is more realistic to use the 3-D atmospheric structure from the M-TGCM model than the 1-D neutral atmosphere. The significant change in (MHD) model inputs indicates that the M-TGCM neutral profiles essentially increase the ion sources resulting from various ionization processes (i.e., photoionization, charge exchange, and electron impact ionization), which in turn enhances the ion escape rate. It is noteworthy that although the M-TGCM model provides the MF-MHD code with 3-D neutral atmosphere profiles that are certainly more realistic (i.e. asymmetric about the globe), there are presently no accurate measurements of the (thermal and suprathermal) oxygen profiles in the Mars atmosphere (*Bougher et al.*, 2008). This uncertainty will affect the calculated ion escape rates. Therefore the neutral atmosphere profiles to be returned by the MAVEN mission will significantly reduce the uncertainty in calculated escape rates resulting from the lack of direct information regarding the oxygen abundance.

Besides providing better inputs to models, MAVEN also has the opportunity to test specific predictions from the models. For instance, MAVEN could test the enhanced ion escape rates during an extreme event, such as a ICME/CIR/SEP or a Martian dust storm and compare them with simulation results, which could help to improve the models with the possible missing physics. It is also possible that MAVEN could make direct observations of the magnetic reconnection in the near Martian magnetotail by its magnetometer (MAG), as has been observed near Venus by Venus Express (VEX) (*Zhang et al.*, 2012). To better study the magnetotail reconnection, one has to adopt adaptive mesh refinement (AMR) to refine the blocks

in the magnetotail region in order to reduce the numerical diffusion. Meanwhile, one needs to employ the resistive MHD model, where the electrical conductivity, σ, is no longer infinite. Although the heavy-ion (such as O^+) cyclotron waves generated from the pickup of exospheric O^+ have never been observed, they may be an important source for heating the cold ionospheric O^+ (*Dong et al.*, 2013). MAVEN may be able to investigate the existence of these waves upstream of the Martian bow shock using the Langmuir probe and waves antenna (LPW). In order to investigate this problem, high-resolution global hybrid simulations are essential. In short, the scientific return from the MAVEN mission will benefit greatly from combining its future returned data with various model results.

3.4 Conclusions

In summary, we studied the solar wind interaction with the Martian upper atmosphere at both current and ancient times by using a one-way coupling of two comprehensive 3-D models, i.e., the M-TGCM thermosphere-ionosphere model outputs were used as inputs for the MF-MHD model. 1-D and 3-D hot oxygen corona were used in the current epoch and ancient times studies, respectively. Our model predicted ion escape rates are in reasonable agreement with the recent observations. The friction or electromagnetic ion-ion beam instability caused by the relative drift velocity between different ion species has an effect to reduce the ion escape plume. At ancient Mars conditions, the net ion escape rate at Epoch 3 (3.5 ± 0.1 Gyr ago) can reach $\sim 10^{25}$ s^{-1}; i.e., one order of magnitude larger than that for current solar minimum conditions ($2\sim3 \times 10^{24}$ s^{-1}). Besides, O^+ ion loss becomes extremely important during ancient times. The second and third MAVEN primary scientific goals are: 2) to determine rates of atmospheric escape through various processes at the current epoch and with these answers, 3) to estimate the integrated loss to space that has occurred through Martian history. Therefore, the immediate impact of the

work will be improvements to estimated ion escape fluxes and global escape rates.

Additionally, we will discuss the solar wind interaction with the Martian upper atmosphere using a more sophisticated coupling approach. In the next few chapters, we will adopt the 3-D Mars cold neutral atmosphere profiles (100 - 300 km) from the newly developed and validated ground to exosphere Mars Global Ionosphere Thermosphere Model (M-GITM) (*Bougher et al.*, 2015a) and the 3-D hot oxygen profiles (100 km - 5 R_M) from Mars Adaptive Mesh Particle Simulator (M-AMPS) (*Lee et al.*, 2013, 2014a,b; *Lee et al.*, 2015). We will couple these 3-D model output fields with the 3-D BATS-R-US Mars multi-fluid MHD model (100 km - 20 R_M). The M-GITM model together with the M-AMPS model take into account the effects of solar cycle and seasonal variations on both cold and hot neutral atmospheres. This will allow us to investigate the corresponding effects on the Martian upper atmosphere ion escape by using a one-way coupling approach (i.e., both the M-GITM and M-AMPS model outputs will be used as the inputs for the MF-MHD model).

CHAPTER IV

Solar wind interaction with the Martian upper atmosphere: variable 3-D cold neutral thermosphere and hot oxygen corona

4.1 Introduction

Unlike Earth and Venus, Mars with a weak gravity allows an extended corona of hot species (*Valeille et al.*, 2009). Being the most important reaction, the dissociative recombination of O_2^+ is responsible for most of the production of dayside exospheric hot atomic oxygen deep in the dayside thermosphere/ionosphere. The sputtering caused by pickup ion (e.g., O^+) collisions with the Martian atmospheric neutral species is also an important source for the hot corona (*Johnson and Luhmann*, 1998). Compared with those cold neutral atoms and molecules, the hot oxygen has a thermal speed larger than the local background thermal speed of the thermosphere (calculated based on M-GITM thermospheric profile (*Bougher et al.*, 2015a)). The hot oxygen can be converted to the thermal oxygen via collisions with other background cold neutral species before it escapes to interplanetary space (*Lee et al.*, 2013; *Lee et al.*, 2015). There are hot hydrogen and carbon coronae as well (*Lee et al.*, 2014a). In this thesis, the cold neutral atoms and molecules refer to the thermal particles, and hot oxygen refers to those from dissociative recombination of O_2^+.

Besides the asymmetric hot oxygen corona, the major Martian atmosphere components (CO_2 and O) are also not symmetric about the planet (that we have mentioned for the M-TGCM outputs in Chapter III). There is more neutral CO_2 on the dayside than nightside (at a constant altitude) because the CO_2 global distribution is mainly controlled by the temperature structure instead of the dynamics. Neutral O, however, is mainly controlled by day-night transport due to its relatively small mass, resulting in a bulge of neutral O in the nightside upper atmosphere (*Bougher et al.*, 2000, 2006, 2008, 2009, 2015a). It is noteworthy that when we mention the cold heavy ionospheric molecular/atomic ions in the thesis, it refers to those ionized from the cold molecular/atomic neutrals. However, these ions can be accelerated to relatively high energy during their escape.

The real Mars upper atmosphere and exosphere are always associated with these asymmetric features. Three-dimensional "whole atmosphere" (from the ground to the exobase, $\sim$ 0 to 250 km) (*Bougher et al.*, 2015a) and exosphere models (*Lee et al.*, 2013; *Lee et al.*, 2015) are ultimately required to capture these asymmetric features by considering thermal, chemical, dynamical processes throughout the entire Mars atmosphere.

Mars provides a complex obstacle to the solar wind that varies on all spatial and temporal scales. Incident solar wind at Mars encounters an extended hot exosphere, a conductive ionosphere, and strong localized crustal magnetic fields. The exosphere, ionosphere and thermosphere are closely coupled with each other via chemical reactions, and are affected by both the low atmospheric dynamics and upstream solar wind conditions. The crustal fields are distributed about the surface of the planet in a very inhomogeneous manner (*Acuña et al.*, 1999). Among all the objects in the solar system Mars, therefore, offers perhaps the most challenging set of conditions to simulate.

In this chapter, we adopt the 3-D Mars thermosphere (i.e., neutral atmosphere

temperatures T_n, neutral densities n_O, n_{CO_2} , and photoionization frequencies I_O, I_{CO_2}) from the Mars Global Ionosphere Thermosphere Model (M-GITM) (*Bougher et al.*, 2015a) and the hot atomic oxygen density, $n_{O_{hot}}$, from the Mars exosphere Monte Carlo model Adaptive Mesh Particle Simulator (M-AMPS) (*Lee et al.*, 2013; *Lee et al.*, 2015). These outputs are one-way coupled with the 3-D Block-Adaptive-Tree-Solarwind-Roe-Upwind-Scheme (BATS-R-US) Mars multi-fluid MHD (MF-MHD) model (*Najib et al.*, 2011; *Dong et al.*, 2014) (see Figure 4.1 for the one-way coupling framework). Please refer to *Lee et al.* (2015) for the detailed study of one-way coupling between M-GITM and M-AMPS, as indicated by the solid grey line in Figure 4.1. M-GITM provides the thermosphere/ionosphere background as input into the M-AMPS exosphere model. The MF-MHD ion escape calculations are based upon M-AMPS adopting the thermosphere from M-GITM and the ionosphere from MF-MHD (see the dashed line in Figure 4.1). The calculations are carried out for selected cases with different solar cycles and crustal field orientations, all assuming equinox conditions in Chapter IV. In total, 19 cases are studied with the combinations of 1-D, 3-D and no hot oxygen corona. We compare the simulation results with both Mars Express (MEX) ion escape measurements and Viking ionospheric profiles.

4.2 Model Description

In this section, the Mars Global Ionosphere Thermosphere Model (M-GITM) (*Bougher et al.*, 2015a), the Mars exosphere Monte Carlo model Adaptive Mesh Particle Simulator (M-AMPS) (*Lee et al.*, 2013, 2014a,b; *Lee et al.*, 2015), and the 3-D BATS-R-US Mars multi-fluid MHD (MF-MHD) model (*Najib et al.*, 2011; *Dong et al.*, 2014) will be briefly introduced. All these models are being used to support the Mars Atmosphere and Volatile EvolutioN (MAVEN) mission activities (2014-2016) (*Lillis et al.*, 2015).

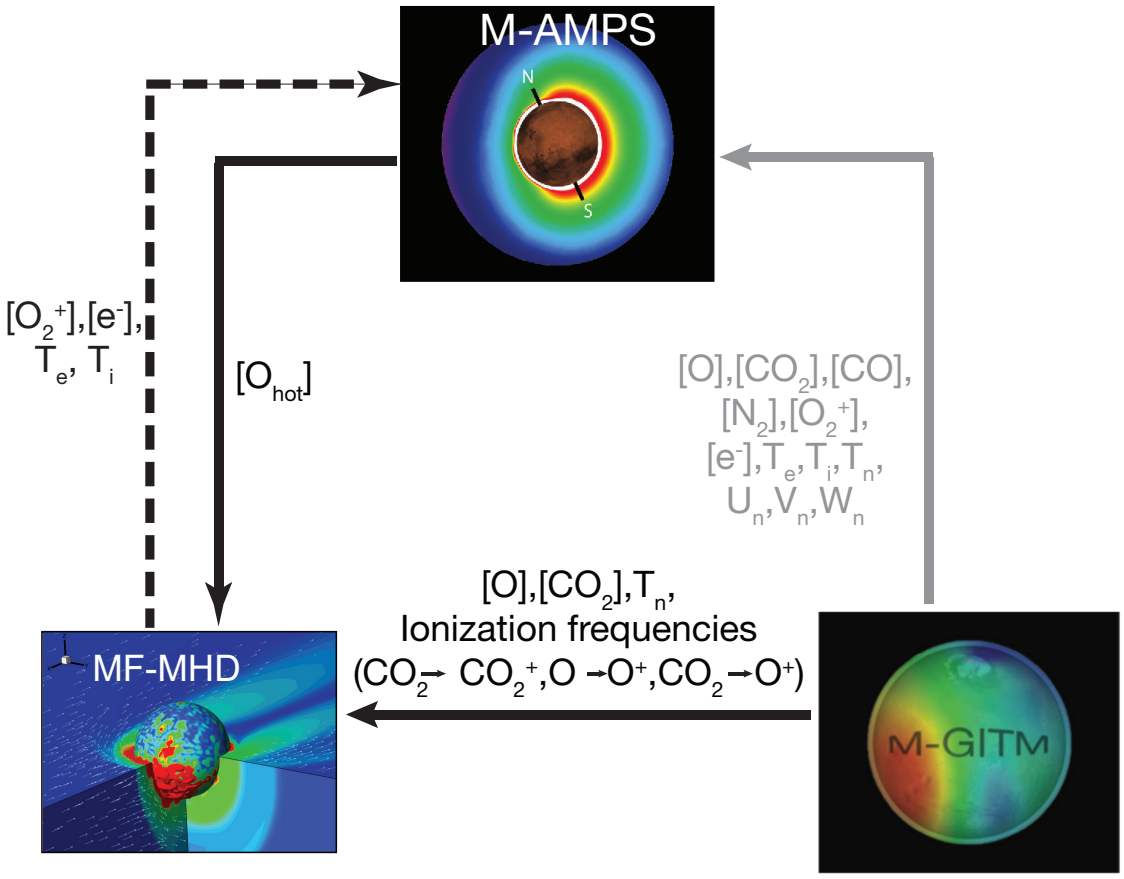

Figure 4.1: A sketch of a one-way coupling approach between M-GITM, M-AMPS and the MF-MHD model (after Figure 1 of *Dong et al.* (2015a)). The notation T_n denotes neutral atmosphere temperatures. [O], [CO_2], and [O_{hot}] are the neutral O, CO_2 and hot atomic oxygen number densities, respectively. Three photoionization processes are included. Here we focus on the one-way coupling indicated by the solid black line. We also test the coupling between MF-MHD and M-AMPS illustrated by the dashed black line. For the detailed study of the one-way coupling between M-GITM and M-AMPS (solid grey line), please refer to *Lee et al.* (2015).

4.2.1 Mars Global Ionosphere Thermosphere Model (M-GITM)

The Mars Global Ionosphere-Thermosphere Model (M-GITM) (*Bougher et al.*, 2015a), combines the terrestrial GITM framework (*Ridley et al.*, 2006; *Deng et al.*, 2008) with Mars fundamental physical parameters, ion-neutral chemistry, and key radiative processes in order to capture the basic observed features of the thermal, compositional, and dynamical structure of the Mars atmosphere from the ground to the exosphere (0 – 250 km). Lower, middle, and upper atmosphere processes are included, based in part upon formulations used in previous lower atmosphere (NASA Ames Mars General Circulation Model) (e.g., *Haberle et al.*, 1999) and upper atmosphere (NCAR Mars Thermospheric General Circulation Model) (e.g., *Bougher et al.*, 2000) models. This enables the M-GITM code to be run for various seasonal, solar cycle, and dust conditions.

M-GITM currently solves for three-dimensional neutral and ion densities, as well as neutral temperatures and winds around the globe. Key neutral species presently include: CO_2, CO, O, N_2, O_2, and Ar. Five key photochemical ion species currently include: O^+, O_2^+, CO_2^+, N_2^+ and NO^+. A dynamical ionosphere, with associated plasma velocities (horizontal and vertical ion velocities), is not presently calculated, but will be implemented soon. Typically, production runs are conducted for a 5×5 degree regular horizontal grid, with a constant 2.5 km vertical resolution (~ 0.25 scale height). There is no hydrostatic assumption in this model, thus it can deal with large vertical velocities (*Ridley et al.*, 2006; *Deng et al.*, 2008). It is noteworthy that the previous Mars Thermospheric General Circulation Model (M-TGCM) is based on the hydrostatic assumption (*Bougher et al.*, 2000, 2006), and thus cannot deal with large vertical winds appropriately, especially when experiencing extreme events (*Fang et al.*, 2013), such as coronal mass ejections (CMEs) and solar energetic particles (SEPs) heating.

M-GITM validation studies thusfar have focused upon simulations for a range of

solar and seasonal conditions (*Bougher et al.*, 2015a). Figure 4.2 shows the neutral number density of CO_2 and O on a sphere of altitude 220 km above the Martian surface for autumnal equinox minimum (AEQUMIN) conditions (L_s =180, F10.7=70). The frame of axes (upper right of Figure 4.2) is shown in the Mars-centered Solar Orbital (MSO) coordinate system, where the $+x$ axis points from Mars to the Sun and the subsolar point is highlighted in each figure. The cold neutral CO_2 is dominant on the dayside upper atmosphere while there is more neutral O in the nightside upper atmosphere owing to day-to-night transport of atomic oxygen by the global thermospheric circulation. These features indicate the importance of adopting the 3-D M-GITM neutral output in a plasma model for study of the solar wind interactions with the Martian upper atmosphere.

4.2.2 Mars Adaptive Mesh Particle Simulator (M-AMPS) model

A state-of-the-art 3-D Direct Simulation Monte Carlo (DSMC) model, the Adaptive Mesh Particle Simulator (AMPS) code was first coded for solving the Boltzmann equation of the gas flow in the coma of a comet (*Tenishev and Combi*, 2008). The AMPS code uses DSMC method, which employs a stochastic solver for both the linear and nonlinear Boltzmann equations. AMPS simulates the ensemble of model particles and captures the physics of the distribution of the gas species in the tenuous upper atmospheres. The AMPS code is generic and applicable to a wide range of kinetic problems.

For modeling the Martian hot atomic corona, M-AMPS has been run in a test-particle Monte Carlo mode with stationary background atmosphere supplied by M-GITM (as indicated by the solid grey line in Figure 4.1), completing the one-way coupling framework (*Lee et al.*, 2013, 2014a,b). The background species include O, CO_2, N_2, CO. The integrated cross sections (in cm^{-2}) are 1.2×10^{-14} for O-CO_2, 6.4×10^{-15} for O-O, and 1.8×10^{-14} for both O-N_2 and O-CO. A forward scattering

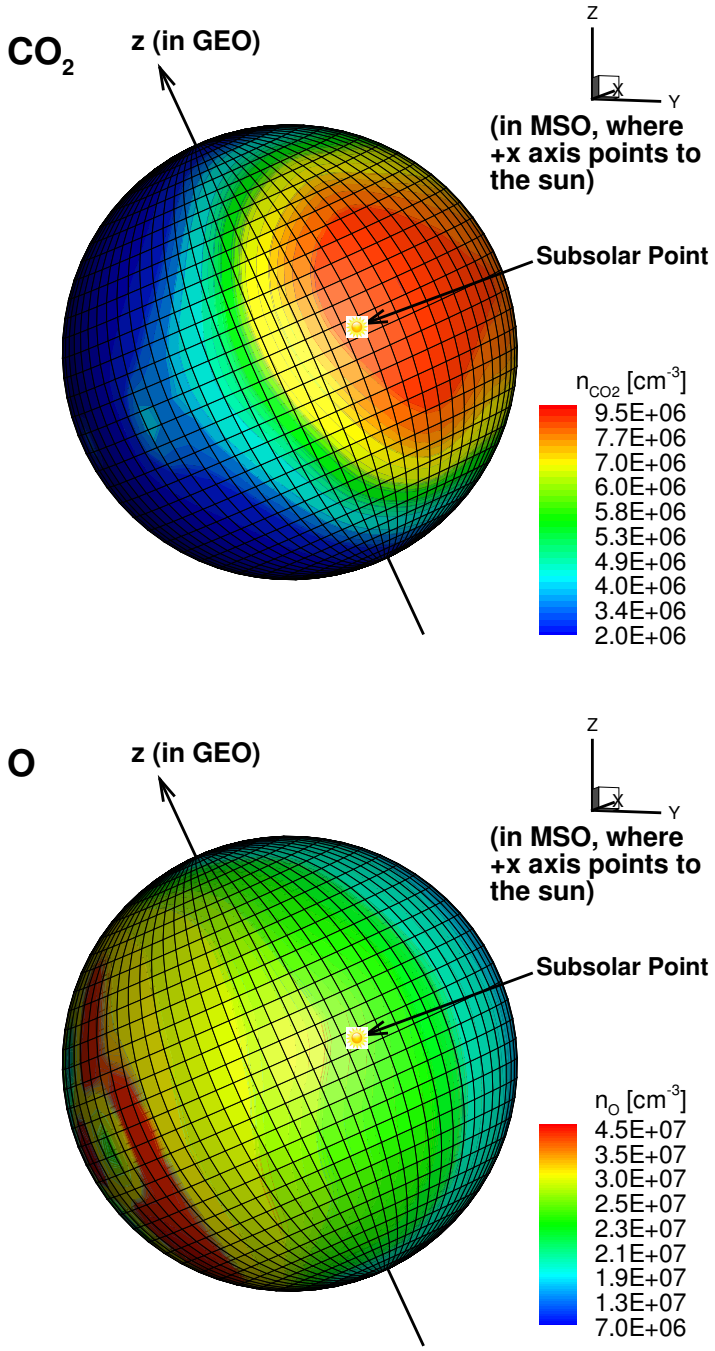

Figure 4.2: The neutral CO_2 and O number densities shown on a sphere of altitude 220 km above the Martian surface from M-GITM for autumnal equinox minimum (AEQUMIN) conditions. Two coordinate systems are displayed in the plot: the Geographic (GEO) and the Mars-centered Solar Orbital (MSO) coordinate systems. The subsolar point is highlighted in each plot.

scheme is used by adopting the angular differential cross section from *Kharchenko et al.* (2000).

Each hot particle in this coupling framework travels within the influence of the planet's gravitational field and collides with background species before escaping to space or being thermalized in the thermosphere. The type of possible collisions with a nascent hot particle can be either a collision between a hot particle and background species or a collision between hot particles. The nominal cell size is about 60 km at the lower boundary of the computational domain, and the maximum cell size is determined by the designated upper boundary of the domain. The computational domain extends from 100 km above the Martian surface to 5 R_M, where R_M is the radius of Mars ($\sim$ 3396 km). M-AMPS includes a data table, which keeps all the information from M-GTIM. All the macro-particles in M-AMPS are initialized based on the thermospheric profile in the data table (*Lee et al.*, 2014a,b). The collision frequencies between different particle species are also evaluated based upon the thermospheric information stored in the data table.

M-AMPS has been successfully one-way coupled with M-GITM and used to calculate both hot atomic carbon and oxygen coronae for Mars (*Lee et al.*, 2013, 2014a,b; *Lee et al.*, 2015). Figure 4.3 shows the hot atomic oxygen number density distribution in a logarithmic scale from a 1-D spherically symmetric model (left) (*Kim et al.*, 1998) and the 3-D M-AMPS code (right) for both autumnal equinox solar minimum (upper panel) and solar maximum (bottom panel) conditions (*Lee et al.*, 2013; *Lee et al.*, 2015). Compared with the 1-D model, the M-AMPS output shows a great day-night O_{hot} asymmetry around Mars globe. The hot atomic oxygen corona is more extensive for solar maximum conditions than for solar mimimim conditions. Figure 4.3 indicates that in order to accurately calculate the ion escape rate, it is imperative to adopt the 3-D hot oxygen corona in a plasma code. When adopting the 1-D hot oxygen profiles from *Kim et al.* (1998) in a plasma model, the O^+ ion escape rates

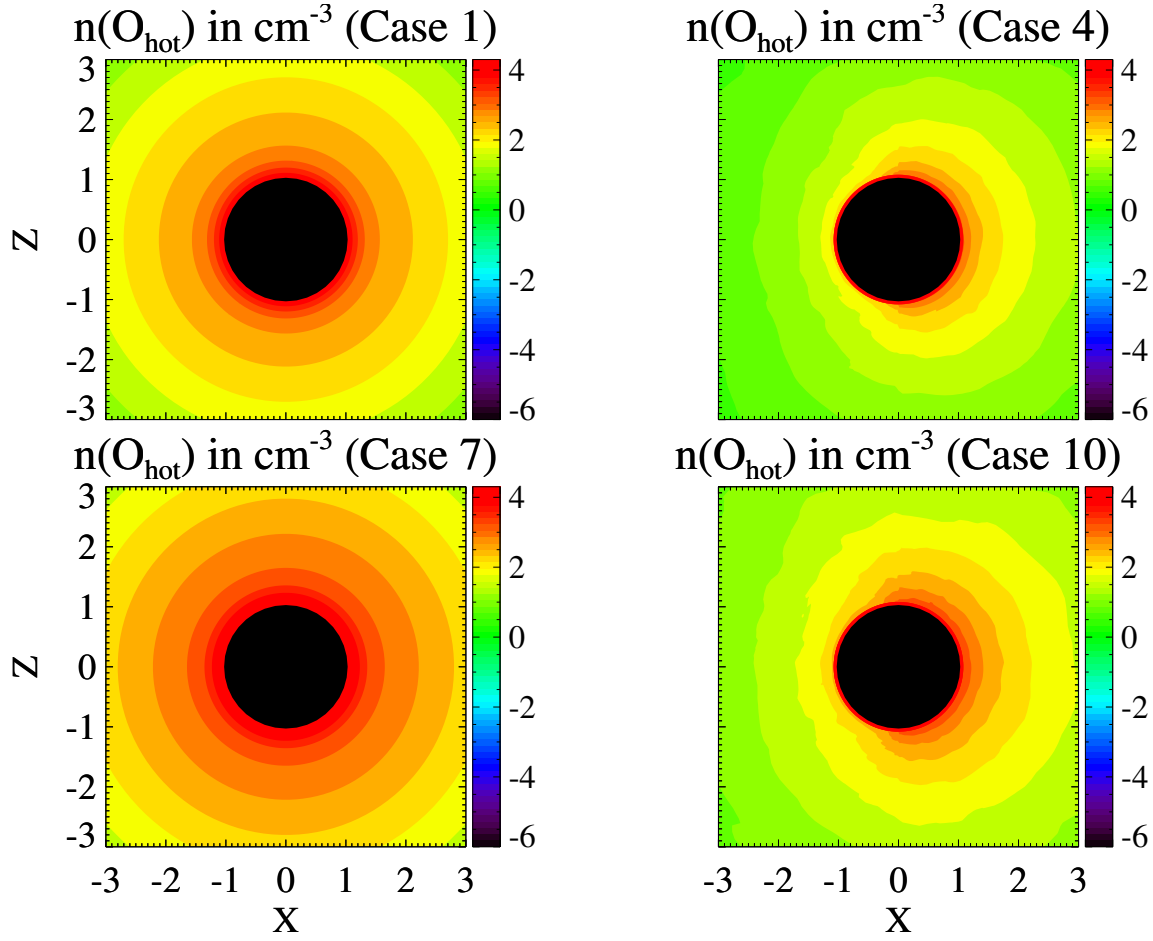

Figure 4.3: A comparison of the hot oxygen number density (in cm^{-3}) distribution from a 1-D spherically symmetric model (left) (*Kim et al.*, 1998) and the M-AMPS code (right) in the x-z plane in the MSO coordinate system. The upper panels show hot O distribution for the autumnal equinox solar minimum (AEQUMIN) conditions and bottom panels illustrate the hot O distribution for the autumnal solar maximum (AEQUMAX) conditions. Note the use of a logarithmic scale.

from the Martian upper atmosphere are larger than those with M-AMPS outputs, as in Table 4.2.

4.2.3 BATS-R-US Mars multi-fluid MHD (MF-MHD) model

The newly developed 3-D BATS-R-US Mars multi-fluid MHD (MF-MHD) model solves separate continuity, momentum and energy equations for the four ion fluids H^+, O^+, O_2^+, CO_2^+ (*Powell et al.*, 1999; *Glocer et al.*, 2009; *Najib et al.*, 2011; *Tóth et al.*, 2012; *Dong et al.*, 2014). Please read Chapter III for more detail on model

descriptions, where the MF-MHD model has been successfully one-way coupled with the 3-D Mars Thermospheric General Circulation Model (M-TGCM) (*Bougher et al.*, 2000, 2006). The effect of the 3-D cold M-TGCM neutral atmosphere on the ion escape has been studied for the current epoch. However, in Chapter III, we adopted the 1-D hot oxygen profiles from *Kim et al.* (1998) for the current epoch studies, and were not able to investigate the effect of the varying inhomogenous crustal fields on the ion escape rate in detail. Moreover, as we described above, the M-TGCM model may not be able to handle the extreme cases (i.e., resulting in large vertical velocities) due to the hydrostatic assumption.

4.2.4 One-way Coupling Approach

Before we discuss the simulation results, we want to briefly mention the method we have chosen to implement the one-way coupling between these models. The three models introduced above use different coordinate systems. The M-GITM and M-AMPS codes run in the Geographic (GEO) coordinate system, where the x axis points from the center of Mars to the surface point (0°N, 0°E), the z axis is perpendicular to the Martian equatorial plane, and the y axis (0°N, 90°E) completes the right-hand system. On the other hand, we use the Mars-centered Solar Orbital (MSO) coordinate system in the MF-MHD model, where the x axis in the coordinate system points from Mars toward the Sun, the z axis is perpendicular to the Martian orbital plane, and the y axis points opposite of the Martian orbital velocity vector, completing the right-handed coordinate system. In Chapter III, we did not use the MSO coordinate in the MF-MHD code but adopted a GEO-like coordinate where the x axis points to the sun but the z axis is the same as in the GEO coordinate for simplification. It is noteworthy that Mars has an axial tilt of 25.19 degrees, indicating an angle of 25.19° between the z axes in GEO and MSO coordinate systems. Figure 4.4 illustrates the coordinate transformation from GEO to MSO system for autumnal equinox minimum

(AEQUMIN) conditions. The frame of axes (upper right) is shown in MSO coordinate system while the mesh and the rotation z-axis are shown in GEO coordinate system. In order to one-way couple these three complicated models, first we need to transfer the cold (M-GITM) and hot (M-AMPS) neutral atmosphere from the GEO to the MSO coordinate system.

In addition, the M-GITM and MF-MHD models use a spherical coordinate system but M-AMPS runs with a Cartesian coordinate system. Since both M-GITM and MF-MHD model are built on spherical coordinates, we can linearly interpolate the cell value from one to the other in the overlapping domains of the two models (100 – 220 km). From 220 km to 5 R_M, we assume constant neutral temperatures and photoionization frequencies based on the M-GITM output (at 220 km) since these values are almost constant when the altitude approaches 220 km. For the neutral atmosphere densities, however, we use an extrapolation based upon the hydrostatic assumption which assumes the neutral atmosphere densities decrease exponentially with altitudes (also read Chapter III). Technically speaking, the hydrostatic assumption may not be accurate enough to describe the cold oxygen component in the Martian exosphere, which should dominate the hot component up to 600 km in altitude (*Feldman et al.*, 2011). However, the comparison of model results (from the one-way coupling between M-GITM and M-AMPS (*Lee et al.*, 2015)) and ALICE/Rosetta observations of the OI 1304 $\mathring{A}$ brightness (*Feldman et al.*, 2011) shows good agreement with each other on the transition altitude from cold to hot oxygen ($\sim$ 600 km), indicating that our extrapolation approach is reasonable. The M-AMPS hot atomic oxygen densities for the MF-MHD model are taken from 100 km to 5 R_M by a linear interpolation approach in the overlapping domain (see Figure 4.3). The input neutral background atmosphere in MF-MHD keeps static during the simulations, while the solar wind and ionosphere are calculated self-consistently.

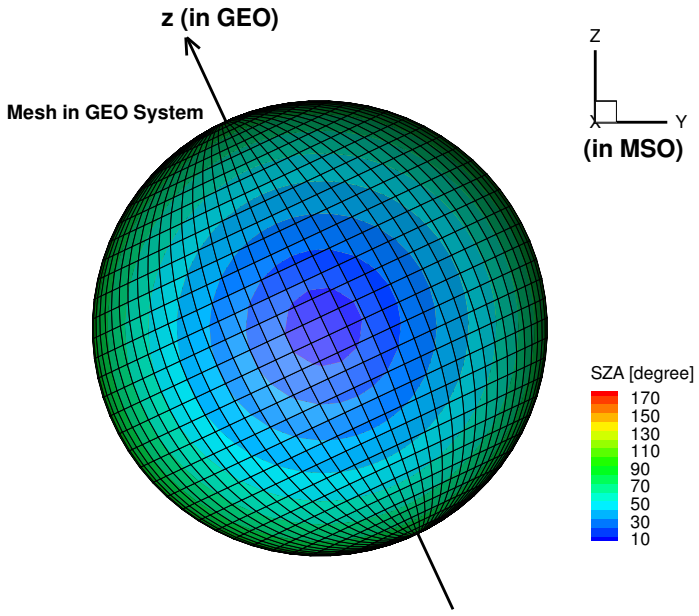

Figure 4.4: An illustration of coordinate transformation from GEO to MSO system for autumnal equinox minimum (AEQUMIN) conditions. The frame of axes (upper right) is shown in $y-z$ plane in MSO coordinate system. The mesh and the rotation (z) axis are shown in GEO coordinate system. The contour shows the solar zenith angle (ZSA).

4.3 Simulation Results and Discussions

In this section, we discuss the simulation results by using the one-way coupling approach introduced in Section 4.2.4, i.e., both the M-GITM and M-AMPS outputs are used as the inputs for the MF-MHD model (Figure 4.1). In order to evaluate the effects of different solar radiation conditions and crustal field orientations on the Mars upper atmosphere ion loss, we study six cases for autumnal equinox solar minimum (AEQUMIN) and solar maximum (AEQUMAX) conditions, respectively. These cases combine different crustal field orientations with 1-D and 3-D hot atomic oxygen profiles. We also study two more cases without the hot oxygen corona for AEQUMAX conditions. In addition, the effect of the M-AMPS outputs by including the solar wind-Mars interaction and crustal field orientation on the Martian ion loss is also studied (see the dashed line in Figure 4.1). Moreover, we calculate the ion

Table 4.1: Input parameters used for the different calculations.

Simulation Cases	Subsolar Position	Hot Oxygen Profiles	Solar Cycle Conditions
Case 1	0°W 0°N	1-D spherically symmetric	Autumnal Equinox Solar Minimum (AEQUMIN)
Case 2	180°W 0°N		
Case 3	270°W 0°N		
Case 4	0°W 0°N	3-D M-AMPS	
Case 5	180°W 0°N		
Case 6	270°W 0°N		
Case 7	0°W 0°N	1-D spherically symmetric	Autumnal Equinox Solar Maximum (AEQUMAX)
Case 8	180°W 0°N		
Case 9	270°W 0°N		
Case 10	0°W 0°N	3-D M-AMPS	
Case 11	180°W 0°N		
Case 12	270°W 0°N		
Case 13	0°W 0°N	no hot O corona	
Case 14	180°W 0°N		
Case 15	0°W 0°N	3-D M-AMPS (MF-MHD Ionosphere)	Autumnal Equinox Solar Minimum
Case 16	180°W 0°N		
Case 17	0°W 0°N	3-D M-AMPS (MF-MHD Ionosphere)	Autumnal Equinox Solar Maximum
Case 18	180°W 0°N		
Case 19	180°W 0°N	1-D M-AMPS (SZA=60°)	AEQUMAX

escape rate for one case where MF-MHD takes a 1-D hot oxygen corona extracted from 3-D M-AMPS output at solar zenith angle (SZA) of 60°. For all the cases, we adopt the 3-D thermosphere profiles from M-GITM. Solar wind density is set to 4 cm^{-3}, the upstream solar wind plasma temperatures are set to 3.5×10^5 K, the interplanetary magnetic field (IMF), B, is assumed to be a Parker spiral in the X-Y plane with an angle of 56°, and solar wind velocity is 400 km/s for all the 19 cases. Table 4.1 summarizes the parameters used for the different cases.

Figures 4.5 and 4.6 illustrate the 2-D (latitude *vs.* local time, at an altitude of 220 km) ionospheric profiles calculated by the MF-MHD model for AEQUMINSSL270 and AEQUMAXSSL270, respectively. For both cases, the top panels show the O^+ ion distribution, and the middle and bottom panels respectively illustrate the O_2^+ and CO_2^+ ion densities. Interestingly, O_2^+ and CO_2^+ ions mirror similar ionospheric

patterns while O^+ displays different ionospheric distributions. As we described above (also see Figure 4.2), there exists more neutral CO_2 on the dayside than nightside while neutral O is dominated at the nightside (at a constant altitude) (*Bougher et al.*, 2008). It is noteworthy that the major source of daytime ionization at Mars is solar EUV radiation. The ionized CO_2^+ quickly reacts with neutral O to produce O_2^+, which becomes the major ion near 130-140 km altitude (Figure 4.7) (*Bougher et al.*, 2008). Although O^+ can be photoionized mainly by neutral O, the absence of the neutral source leads to the low abundance of O^+ in the dayside Martian upper atmosphere, consistent with the neutral distribution shown in Figure 4.2. Inspection of the colorbars in all contour plots (Figures 4.5-4.6) reveals that O_2^+ ions are the major ions in the Martian ionosphere at 220 km altitude. In order to show improved MF-MHD simulation results by adopting the 3-D thermosphere profile, we compare the calculated ion densities with Viking data (*Hanson et al.*, 1977) for the AEQUMIN case with SSL=270 (Case 6). Compared with Figure 8 in *Najib et al.* (2011), Figure 4.7 reveals a better agreement between the calculated ion densities and the Viking data, especially for the O^+ ion.

Figure 4.8 shows a comparison of O^+ ion escape plumes in the $x - z$ plane for 1-D (Case 7), 3-D (Case 10) and no (Case 13) hot atomic oxygen corona simulations. The main feature of the MF-MHD model is the asymmetric escape plume shape for heavy ion (O^+, O_2^+, and CO_2^+) species. The asymmetric plume provides a channel for ions to escape that cannot be captured by the multi-species MHD model (*Ma et al.*, 2004; *Ma and Nagy*, 2007a). As is evident is Figure 4.8, the MF-MHD calculation with 1-D hot O has a stronger O^+ ion escape plume than that with a 3-D M-AMPS hot O corona, especially at the high altitude corona region. It indicates that using the 1-D spherically symmetric hot atomic oxygen profiles results in the largest O^+ ion escape rate from the Martian upper atmosphere. Compared with Cases 7 and 10, the contour plot of Case 13 (right panel) mirrors a less asymmetric and relatively

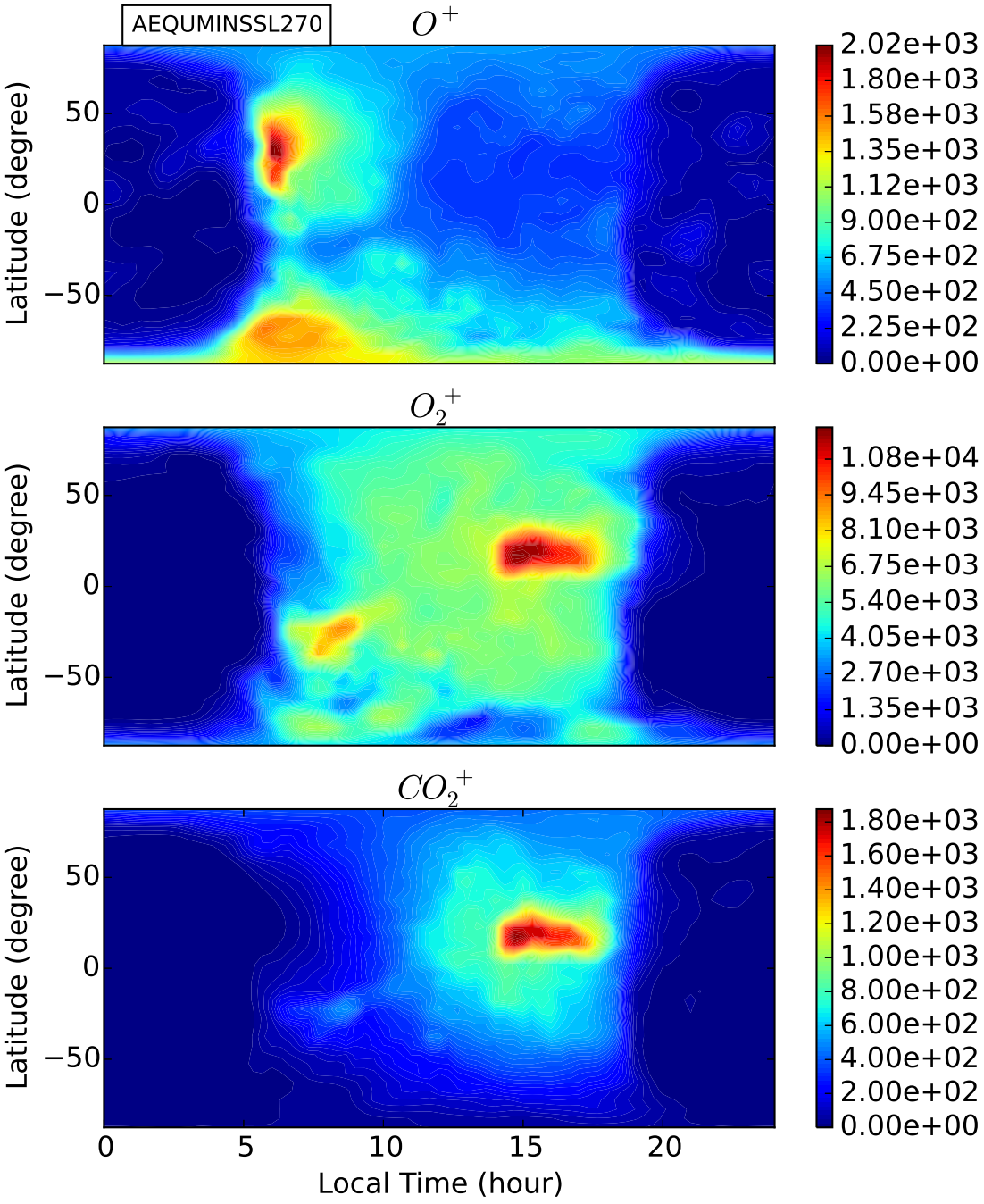

Figure 4.5: The ionospheric ion density profiles for O^+, O_2^+, and CO_2^+ at altitude 220 km for autumnal equinox minimum (AEQUMIN) conditions with subsolar longitude equal to 270° E.

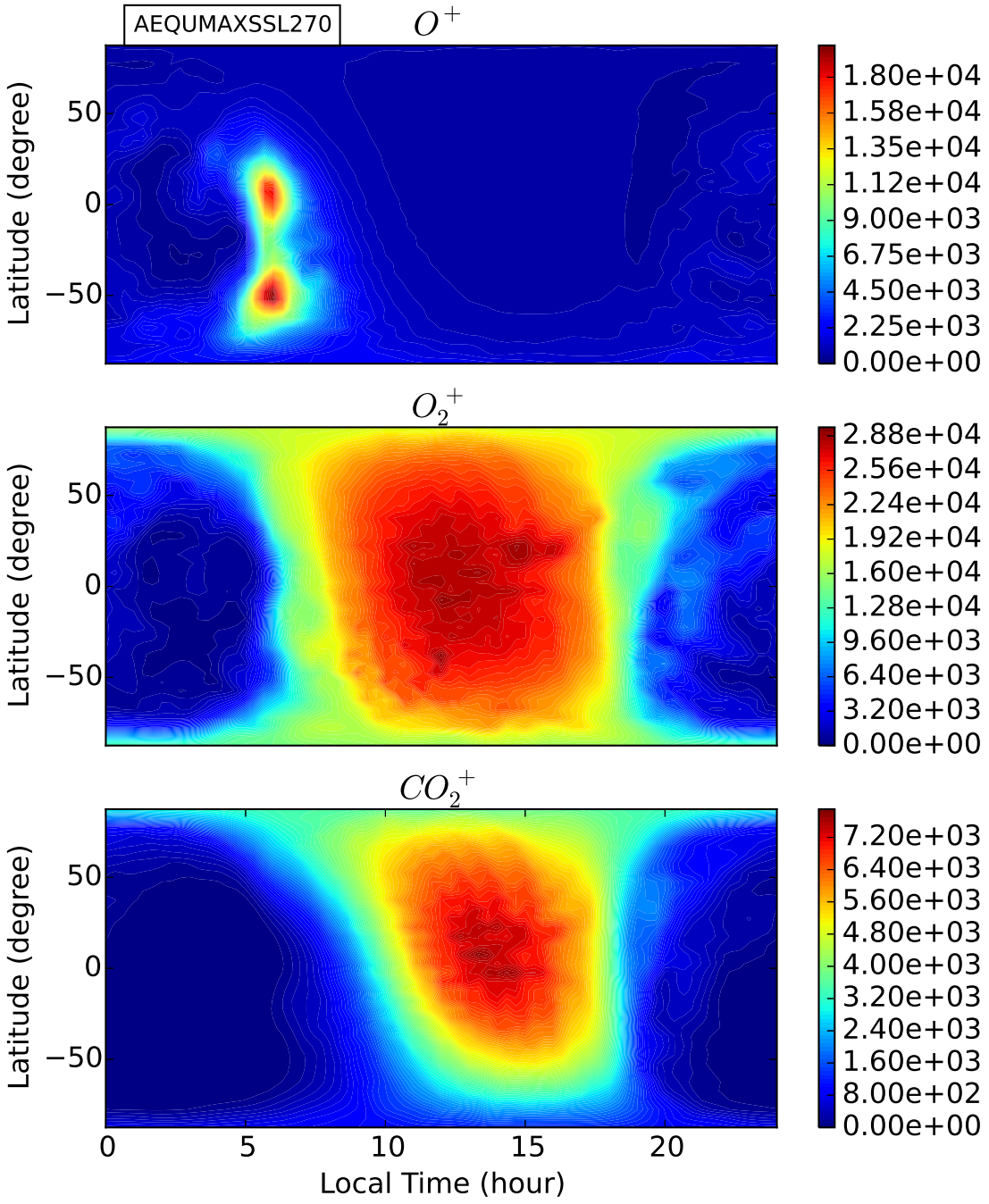

Figure 4.6: The ionospheric ion density profiles for O^+, O_2^+, and CO_2^+ at altitude 220 km for autumnal equinox maximum (AEQUMAX) conditions with subsolar longitude equal to 270° E.

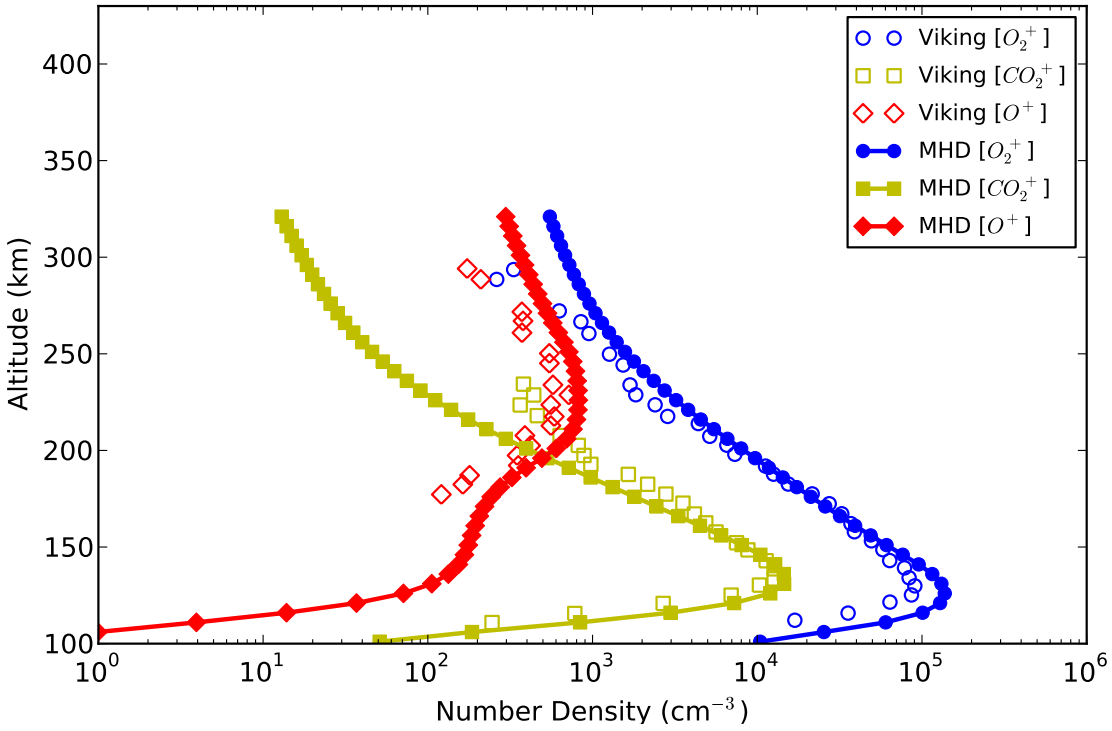

Figure 4.7: The ion density comparison between the MF-MHD simulations and the Viking observations for O_2^+, CO_2^+, and O^+ ions (*Hanson et al.*, 1977).

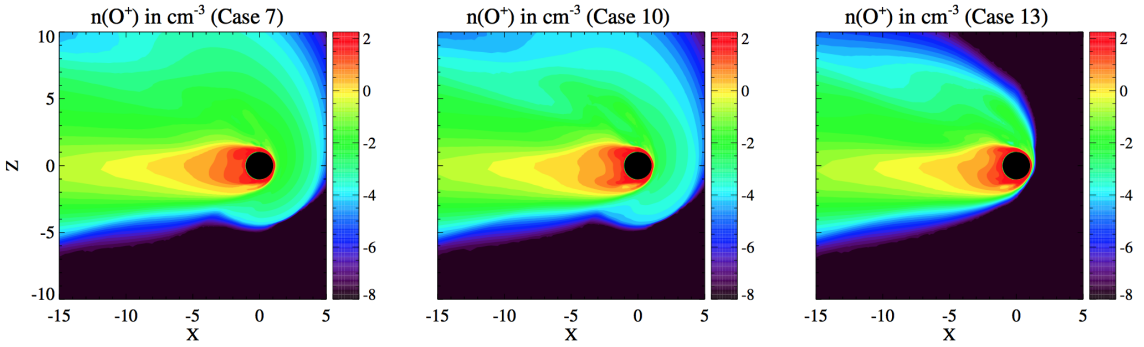

Figure 4.8: A comparison of O^+ ion escape plume in the $x - z$ plane for 1-D, 3-D and no hot atomic oxygen corona. Left: AEQUMAX with 1-D spherically symmetric hot oxygen corona from *Kim et al.* (1998) (Case 7); middle: AEQUMAX with 3-D M-AMPS hot oxygen corona (Case 10); right: AEQUMAX without hot oxygen corona (Case 13). Note the use of a logarithmic scale.

weak escape plume due to the lack of a neutral hot oxygen corona. However, the O^+ ion escape plume (in Case 13) without hot oxygen can still be clearly observed, implying that the cold neutral oxygen plays an important role in the O^+ ion escape. Without calculating the values, it is reasonable to infer that the O^+ ion escape rate is decreasing from the left panel to the right panel. The contour plots in Figure 4.8 are consistent with the neutral hot oxygen profiles (Figure 4.3) and the corresponding ion escape rates (Table 4.2).

We further investigate the effect of different hot oxygen profiles on the Martian upper atmosphere ion loss. Figure 4.9 compares different hot O profiles. The dotted black and dashed red curves represent calculations considering the effects of solar wind and crustal field (i.e., adopting a dynamical ionosphere). The dash-dotted blue curve represents the case where M-AMPS uses a ionosphere based upon photochemical equilibrium from M-GITM. All the M-AMPS profiles in Figure 4.9 are extracted at solar zenith angle (SZA) of 60°. The hot oxygen profiles (solid yellow curves) from *Kim et al.* (1998) are always the largest among all four cases independent of solar cycle, which suggests the corresponding O^+ ion escape rates are also the largest. When the main crustal source is on the nightside, there is no significant difference between the M-AMPS outputs (dashed red and dash-dotted blue curves). However,

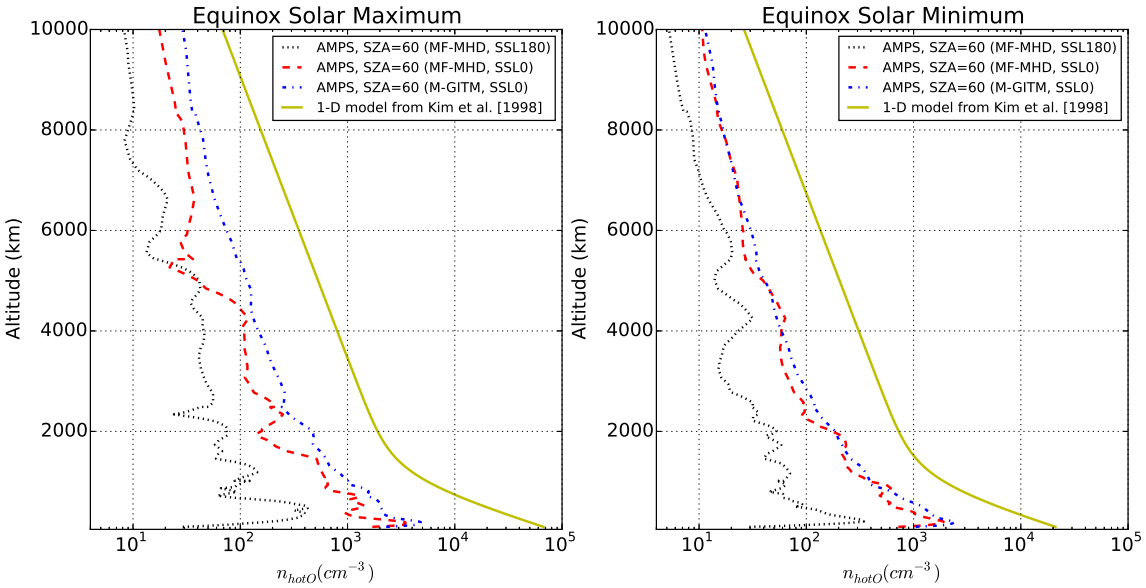

Figure 4.9: The comparison of different hot oxygen profiles. The dotted black and dashed red curves represent the hot oxygen profile at solar zenith angle (SZA) of 60 by taking MF-MHD ionosphere (SSL=180 and 60) as M-AMPS inputs. The dash-dotted blue curves display the hot oxygen profile at SZA of 60 by taking M-GITM ionosphere (SSL=0) as M-AMPS input. The solid yellow curves show the 1-D hot oxygen model from *Kim et al.* (1998).

the dayside crustal fields shift the M-AMPS output to smaller values (for more detail, please refer to Lee et al., 2015, in preparation), leading to a reduction of the O^+ ion escape rate as will be shown later.

We summarize the calculated ion escape rates for 19 cases in Table 4.2. The calculations are conducted by integrals of the plasma density multiplied by the radial velocity component at the surface of a sphere far from the planet. Given the fact that the calculated ion escape rates do not change to any significant degree once the radius exceeds 4 R_M, we set the integral spherical surface to 6 R_M. On average, our CO_2^+ ion contribution to the total ion escape (O^+, O_2^+ and CO_2^+) is about 6.74% for AEQUMIN conditions (Cases 4-6), 3.59% for AEQUMAX conditions (Cases 10-12) and 4.29% for AEQU conditions (average over solar cycles), which are consistent with the observations (< 10%) (*Lundin et al.*, 2009). Based on our solar wind input (density: 4 cm^{-3} and velocity: 400 km/s), the total ion escape rate for AEQUMIN conditions (Cases 1-3 average: 2.08×10^{24} s^{-1}, and Cases 4-6 average: 1.93×10^{24}

s^{-1}) is $\sim 2 \times 10^{24}$ s^{-1}, and for AEQUMAX conditions is (6.87 to 7.48) $\times 10^{24}$ s^{-1} (on the order of $\sim 1 \times 10^{25}$ s^{-1}), which is reasonably consistent with the ion escape rate estimated from MEX data (*Lundin et al.*, 2013; *Ramstad et al.*, 2015). A detailed investigation of the ion escape rates by including the seasonal variations is given in Chapter V.

In order to show the simulation results in an intuitive way, we plot two histograms for AEQUMIN (upper panel) and AEQUMAX (bottom panel) conditions in Figure 4.10. Several conclusions can be summarized based on the comparison among the 19 cases: (1) The total ion escape rates (O^+, O_2^+ and CO_2^+) for AEQUMIN conditions are always smaller than those of AEQUMAX conditions (on average by a factor of $\sim$ 3.6). (2) For AEQUMIN conditions, the major ion escape rate is contributed by O_2^+ ions, while O^+ is the main escape ion species for AEQUMAX conditions. CO_2^+ has the smallest ion escape rate among all the heavy ionospheric ion species for all the cases. (3) Compared with the 1-D spherically symmetric hot atomic oxygen corona from *Kim et al.* (1998), the 3-D M-AMPS output reduces the O^+ ion escape rate. (4) Comparing cases with different crustal field orientations, the crustal fields are demonstrated to have a shielding effect, which protects Mars from interacting with the solar wind and thus reduces the ion escape rate. (5) Comparing cases with and without hot oxygen corona, it is found that the hot oxygen corona has an effect to increase the O^+ ion escape rate but decrease the cold ionospheric heavy ions (O_2^+ and CO_2^+) loss. It also shows that the cold neutral oxygen plays an important role in the Martian O^+ ion escape. (6) There is no significant influence on the calculated ion escape rates by including a MF-MHD dynamical (instead of a M-GITM photochemical equilibrium) ionosphere in M-AMPS. (7) By adopting the 1-D hot O profile from M-AMPS at the SZA of 60°, the MF-MHD simulation can well reproduce the ion escape rates by using the 3-D M-AMPS hot O corona as inputs.

The reasons are given as follows. The solar radiation fluxes for AEQUMAX con-

ditions (F10.7=200) are higher than those for AEQUMIN conditions (F10.7=70). Therefore, more neutral atmosphere particles are ionized for AEQUMAX conditions due to higher photoionization rates. Technically speaking, in the same solar wind and IMF environments, a larger ion source leads to enhanced ion loss during the solar wind interaction. Compared with AEQUMIN conditions, O^+ is the dominant escape ion for AEQUMAX conditions. It is caused by both high photoionization frequencies, and enhanced cold and hot O densities in the thermosphere/exosphere, especially below 600 km (*Feldman et al.*, 2011). The cold thermospheric/exospheric oxygen component (e.g., see Figures 1 and 2 in *Ma et al.* (2004)) also plays an important role in the solar wind planet interaction.

In order to test this idea, we conducted simulations for two addition cases (Case 13 and Case 14) for AEQUMAX conditions without any hot oxygen corona. Interestingly, the ion escape rate of O^+ is still dominant over the other two heavy ionospheric species. Compared with Case 13 (subsolar longitude, SSL=0°W), Cases 7 & 10 show that the hot oxygen corona increases the O^+ ion escape but decreases the cold heavy ionospheric ions (O_2^+ and CO_2^+) loss. Comparison of Case 14 with Cases 8 & 11 (SSL=180°W) also mirrors that the hot oxygen corona can protect the heavy ionospheric ions from escaping through solar wind erosion. In the absence of a hot oxygen corona, the solar wind can directly interact with the Martian upper atmosphere without any mass loading of corona O^+ ion. Besides, the ionized corona O^+ ion behaves like a conductor, which can help to prevent the electromagnetic fields from penetrating deeply into the Martian ionosphere, and thus the Martian lower ionosphere are less affected. The reason why CO_2^+ is the ion species with the smallest loss rate is because it is the heaviest one among all the major Martian ionospheric components, therefore, it is located relatively deep in the Martian ionosphere. Besides, the ionosphere abundance of CO_2^+ is lower than that of O_2^+ in the Martian ionosphere (Figure 4.7).

The crustal fields provide a magnetic pressure, $B^2/(2\mu_0)$, to balance the solar wind dynamic pressure, $\rho_{sw}v_{sw}^2$, during the process of solar wind interaction. When the crustal fields face the sun, they prevent the solar wind from penetrating deeply into the Martian lower ionosphere due to this pressure balance; thus the lower ionosphere is less affected and ion loss is decreased. Compared with Cases 10 and 11 (ratio of SSL0/SSL180 for O^+: 1.20, O_2^+: 1.40, and CO_2^+: 1.08), the crustal field shielding effect is more significant on the control of ion loss (especially for O^+ ions) when there is no hot oxygen corona (Cases 13 and 14, ratio of SSL0/SSL180 for O^+: 1.59, O_2^+: 1.55, and CO_2^+: 1.41). The reason is that the crustal field has a strong shielding effect on protecting the Martian ionosphere but it does not have a significant constraint on the exospheric O^+ ion loss by the pickup process that occurs far away from the Martian ionosphere. As we described earlier, the source of O^+ ion loss in Cases 13 and 14 is the ionized cold thermosphere and exosphere oxygen, therefore the crustal fields can still significantly protect these ion from escaping. By analyzing the ASPERA-3 data from MEX, *Lundin et al.* (2011) reported that when the crustal field faces the sun, it has an effect to deviate the dayside ion flow and thus reducing the tailward transport and escape of ionospheric plasma. It supports our simulation results.

As indicated in Figures 4.3 and 4.8, the spherically symmetric 1-D hot atomic oxygen profile from *Kim et al.* (1998) shows the largest abundance of the hot O around Mars globe, especially near the polar regions and on the nightside of the Martian upper atmosphere. The most extensive hot oxygen corona from *Kim et al.* (1998) produces the largest amount of O^+ from photoionization and electron impact ionization (*Curry et al.*, 2013), which in turn enhances O^+ ions escaping from Mars upper atmosphere. In order to investigate the effects of solar wind-Mars interaction and crustal field orientation on the M-AMPS output, we studied four more cases by including the MF-MHD calculated ionosphere in the M-AMPS model. The M-AMPS neutral profiles are still taken from M-GITM. In other words, when M-AMPS

Table 4.2: Calculated ion escape fluxes (in $\times 10^{24}$ s^{-1}).

Simulation Cases	O^+	O_2^+	CO_2^+	Total	$(O_2^+ + CO_2^+)/O^+$	CO_2^+/Total (%)
Case 1 (MINSSL0-1D)	0.52	1.72	0.15	2.40	3.58	6.42
Case 2 (MINSSL180-1D)	0.41	1.14	0.11	1.66	3.00	6.48
Case 3 (MINSSL270-1D)	0.58	1.47	0.14	2.19	2.76	6.30
1-3 average (MIN-1D)	0.51	1.44	0.13	2.08	3.11	6.39
Case 4 (MINSSL0-3D)	0.41	1.68	0.15	2.24	4.42	6.90
Case 5 (MINSSL180-3D)	0.31	1.12	0.11	1.53	4.01	6.89
Case 6 (MINSSL270-3D)	0.44	1.45	0.13	2.02	3.60	6.46
4-6 average (MIN-3D)	0.39	1.42	0.13	1.93	4.00	6.74
Case 7 (MAXSSL0-1D)	5.59	2.45	0.24	8.28	0.48	2.94
Case 8 (MAXSSL180-1D)	4.44	1.76	0.23	6.43	0.45	3.56
Case 9 (MAXSSL270-1D)	5.50	2.01	0.23	7.74	0.41	2.92
7-9 average (MAX-1D)	5.18	2.07	0.23	7.48	0.45	3.11
Case 10 (MAXSSL0-3D)	4.57	2.52	0.26	7.35	0.61	3.49
Case 11 (MAXSSL180-3D)	3.81	1.80	0.24	5.86	0.54	4.16
Case 12 (MAXSSL270-3D)	4.99	2.17	0.24	7.40	0.48	3.25
10-12 average (MAX-3D)	4.46	2.17	0.25	6.87	0.54	3.59
Case 13 (MAXSSL0-noO_{hot})	3.70	3.25	0.31	7.27	0.96	4.32
Case 14 (MAXSSL180-noO_{hot})	2.33	2.10	0.22	4.64	1.00	4.65
13-14 average (MAX-noO_{hot})	3.01	2.68	0.26	5.96	0.98	4.45
4-6 & 10-12 average (AQEU-3D)	2.42	1.79	0.19	4.40	0.82	4.29
Case 15 (MINSSL0-3D,MF-MHD Iono)	0.40	1.65	0.15	2.20	4.50	6.82
Case 16 (MINSSL180-3D,MF-MHD Iono)	0.31	1.14	0.11	1.56	4.03	7.05
Case 17 (MAXSSL0-3D,MF-MHD Iono)	4.58	2.57	0.26	7.41	0.62	3.51
Case 18 (MAXSSL180-3D,MF-MHD Iono)	3.68	1.79	0.24	5.72	0.55	4.20
Case 19 (MAXSSL180-1D-SZA60)	3.79	1.80	0.24	5.83	0.54	4.12

is coupled with M-GITM, neutral density (n_O, n_{N_2}, n_{CO}, n_{CO_2}), temperature (T_e, T_i, T_n), neutral wind (U_n, V_n, W_n), and ion and electron densities ($n_{O_2^+}$ and n_{e^-}) are all taken from M-GITM. However, in order to include a dynamical (instead of a photochemical equilibrium) ionosphere, we now adopt the densities ($n_{O_2^+}$ and n_{e^-}) and temperatures (T_i and T_e) from MF-MHD as M-AMPS inputs (see the dashed line in Figure 4.1). Although the O^+ ion escape rate is reduced slightly (e.g., Case 11 and Case 18), ion escape rates do not change to any significant degree. The effect of the dynamical ionosphere on the neutral escape rates is given in another paper (Lee et al., 2015, in preparation). Moreover, we compare MF-MHD calculations by adopting M-AMPS 1-D (at SZA=60°) and 3-D hot O profiles. The small difference on the ion escape rates between Case 11 and Case 19 suggests that ion escape calculations by adopting an appropriate 1-D hot O profile can well reproduce results by utilizing the 3-D M-AMPS outputs.

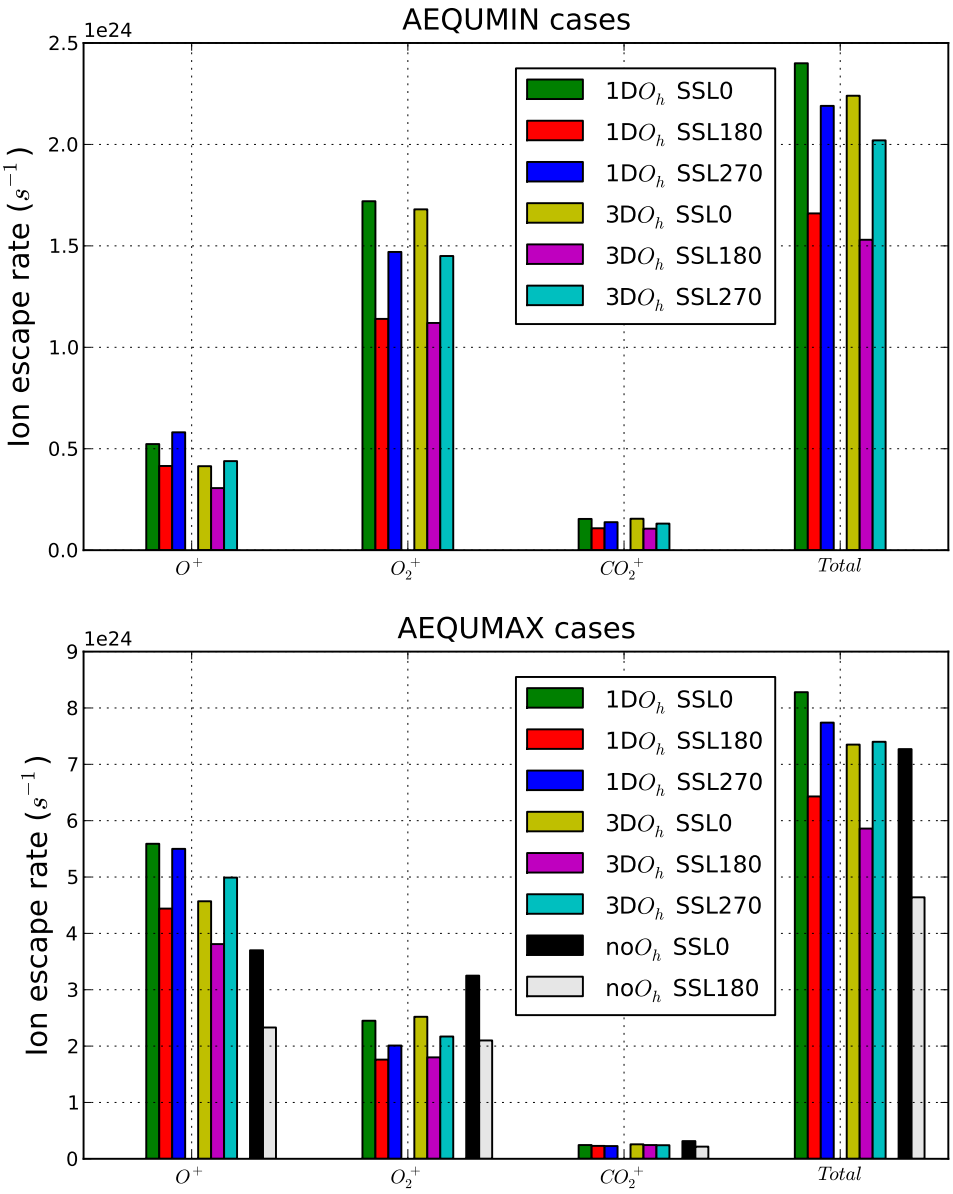

Figure 4.10: The histograms of ion escape rate (in s^{-1}). Upper panel: cases with AEQUMIN conditions; bottom panel: cases with AEQUMAX conditions. Note that the scales in vertical axes (ion escape rate) in these two plots are different. SSL stands for subsolar longitude.

4.4 Conclusions

In summary, we studied the solar wind interaction with the Martian upper atmosphere by using a one-way coupling of three comprehensive 3-D models, i.e., the M-GITM thermosphere-ionosphere model outputs and the M-AMPS hot atomic oxygen corona are used as inputs for the MF-MHD model. The effects of 1-D/3-D asymmetric cold neutral atmosphere, hot oxygen corona, and crustal field orientations are studied in detail using comparisons among 19 simulated cases. Compared with the 1-D spherically symmetric hot O profiles from *Kim et al.* (1998), our simulations showed that the 3-D M-AMPS oxygen corona reduces the O^+ ion loss. It is found that there is no significant effect on the MF-MHD calculated ion escape rates by using hot oxygen coronae from M-AMPS, where either a photochemical equilibrium or dynamical (by including the effects of solar wind-Mars interaction and crustal fields) ionosphere is adopted. Besides, by adopting the 1-D hot oxygen profile extracted from a 3-D M-AMPS simulation at a suitable solar zenith angle of 60°, the MF-MHD can well reproduce the calculated ion escape rate by utilizing the 3-D M-AMPS output. The crustal fields can protect Mars from interacting with the solar wind and thus reducing the ion loss from the Martian upper atmosphere due to its shielding effect. In addition, the hot oxygen corona plays an important role in increasing the O^+ ion escape and decreasing the heavy ionospheric ion species (O_2^+ and CO_2^+) loss. Meanwhile, simulations show that the cold oxygen is the primary neutral source for O^+ ion escape. Our calculated ion escape rates are in reasonable agreement with the MEX observations. For AEQUMIN conditions, our total ion (O^+, O_2^+ and CO_2^+) escape rate is (1.93 to 2.08) $\times$ 10^{24} s^{-1} and for AEQUMAX conditions, the net ion loss is (6.87 to 7.48) $\times$ 10^{24} s^{-1}, on the order of $\sim$ 1.0 $\times$ 10^{25} s^{-1}.

Since there is no significant effect on the calculated ion escape rates by using either a dynamical or photochemical equilibrium ionosphere, we will adopt the M-AMPS outputs based upon the M-GITM ionosphere in the following chapters for

simplification (i.e., ignoring the dashed line illustrated in Figure 4.1). In the next chapter, we will focus on the effects of crustal field orientation, solar cycle and seasonal variations on the Martian upper atmosphere ion loss.

CHAPTER V

Solar wind interaction with the Martian upper atmosphere: Crustal field orientation, solar cycle and seasonal variations

5.1 Introduction

The Sun has a powerful influence on planetary atmospheres. Annual changes in temperature on a planet are caused by a combination of two factors: axial tilt and variations in the distance from the Sun. On Earth, the axial tilt determines nearly all of the annual variations, because Earth's orbit is nearly circular. Mars, however, has the highest orbital eccentricity of any planet except Mercury; the distance from the Sun to Mars varies approximately from 1.38 AU to 1.66 AU over a Martian year. This large variation, combined with an axial tilt (25.19°) slightly greater than Earth's (23.4°), gives rise to seasonal variations far greater than those we experience even in the coldest areas on our own planet (*de Pater and Lissauer*, 2010). Furthermore, Mars has no global intrinsic dipole magnetic field; instead, it has a crustal magnetic field, which was first discovered by the Mars Global Surveyor spacecraft (MGS) (*Acuña et al.*, 1999). The crustal fields, B_c, are distributed about the surface of the planet in a very inhomogeneous manner, which plays an important role in the process of solar wind planet interaction.

Atmospheric dynamics and chemistry are greatly affected by temperature, suggesting that the entire Mars atmosphere is an integrated system that must be treated as a whole from the ground to the exobase ($\sim$ 0 to 250 km) (*Bougher et al.*, 2015a). In fact, strong coupling processes are known to link the Mars lower to upper atmospheres (e.g., *Bougher et al.*, 2014). These processes are crucial to be quantified in order to reliably predict upper atmosphere densities, temperatures, winds, planetary waves (e.g., tides and gravity waves) over various timescales (e.g. solar cycle, seasonal, and diurnal). Three-dimensional "whole atmosphere" models are ultimately required to capture these coupling processes (e.g., thermal, chemical, dynamical) throughout the entire Mars atmosphere. The 3-D Mars Global Ionosphere Thermosphere Model (M-GITM) (*Bougher et al.*, 2015a) is such a model that can generate a relatively realistic Martian atmosphere with detailed structures that incorporates the effects of solar cycle and seasonal variations.

The weak gravity of Mars allows an extended corona of hot species to be present (*Valeille et al.*, 2009) (read Chapter IV for more detail). In order to reproduce a realistic asymmetric corona of hot species from observations, a 3-D global kinetic exosphere model is required, especially above the exobase (Knudsen number, $K_n \approx 1$) where the fluid assumption usually fails (*Lee et al.*, 2013). One such model is the Mars exosphere Monte Carlo model Adaptive Mesh Particle Simulator (M-AMPS) (*Tenishev and Combi*, 2008; *Lee et al.*, 2013, 2014a,b), which can generate a 3-D hot (e.g., oxygen and carbon) corona with detailed asymmetric structure. In order to capture these 3-D asymmetries, 3-D thermosphere/ionosphere inputs from a validated ground-to-exobase atmospheric model (e.g., M-GITM) are essential (see Figure 4.1).

It is difficult to accurately calculate global ion escape rates from spacecraft data due to the complex geometry of loss regions around Mars. Thus the use of global simulations is necessary. In this chapter, we study the solar wind interaction with the Martian upper atmosphere by using a one-way coupling of three comprehensive

3-D models as described in Chapter IV. The calculations are carried out for twenty-two cases with combinations of different crustal field orientations (four cases without crustal field), solar cycle and Martian seasonal conditions.

5.2 Model Descriptions and results

Since we have already introduced the Mars Global Ionosphere Thermosphere Model (M-GITM) (*Bougher et al.*, 2015a), the Mars exosphere Monte Carlo model Adaptive Mesh Particle Simulator (M-AMPS) (*Lee et al.*, 2013, 2014a,b), and the 3-D BATS-R-US Mars multi-fluid MHD (MF-MHD) model (*Najib et al.*, 2011; *Dong et al.*, 2014) in Chapters III and IV. Here we only show some model results related to the Martian seasonal, solar cycle and crustal field variations.

5.2.1 Mars Global Ionosphere Thermosphere Model (M-GITM)

Figure 5.1 illustrates the CO_2 and O densities on a sphere of altitude 220 km for two extreme conditions. Again, great day-night asymmetry and detailed local structure are clearly shown in these four density contour plots, demonstrating the importance of adopting 3-D M-GITM neutral outputs. These plots are shown on a 2-D spherical surface with the rotation axis parallel to both $x - z$ plane (in MSO coordinates) and the plane of the paper, where the subsolar point is highlighted in each plot. Note that there is an angle of 25.19 degrees between the two z axes due to the axial tilt.

5.2.2 Mars Adaptive Mesh Particle Simulator (M-AMPS) model

Figure 5.2 shows the hot atomic oxygen number density distribution in a logarithmic scale from the 3-D M-AMPS code. The upper panel shows the autumnal equinox solar minimum (AEQUMIN, left) and maximum (AEQUMAX, right) conditions and the bottom illustrates aphelion solar minimum (APHMIN, left) and perihelion so-

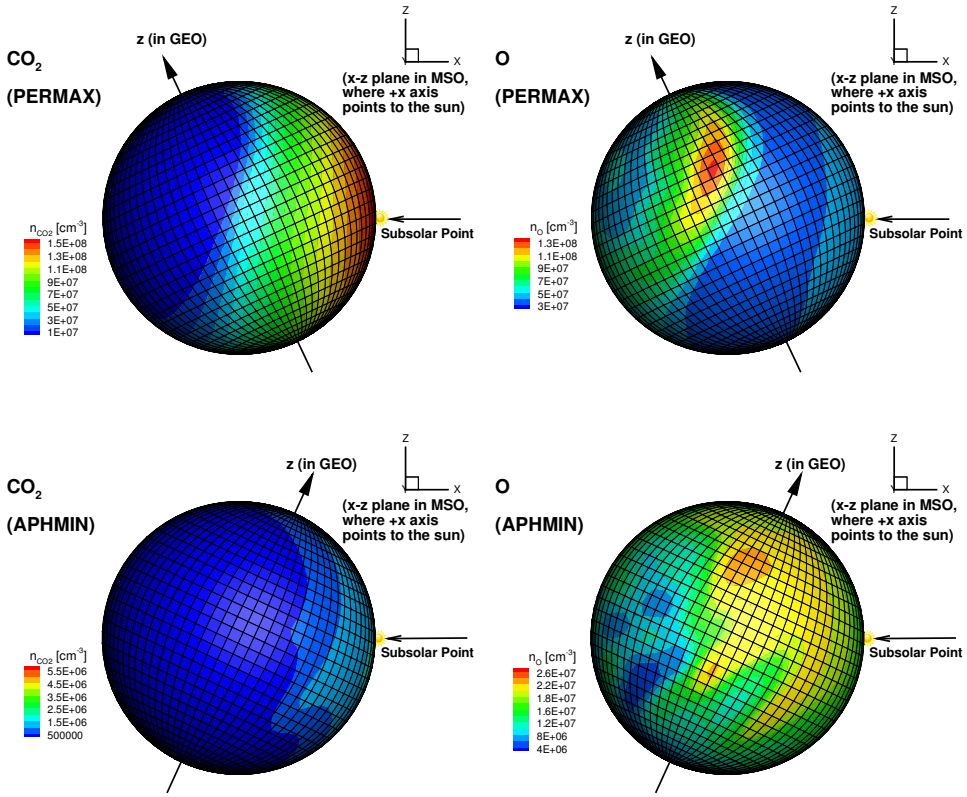

Figure 5.1: The neutral CO_2 and O number densities shown on a sphere at an altitude of 220 km above the Martian surface from M-GITM for perihelion solar maximum (PERMAX) and aphelion solar minimum (APHMIN) conditions. Two coordinate systems are indicated in each plot: the Geographic (GEO) and the Mars-centered Solar Orbital (MSO) coordinate systems. The spheric contour plots are shown in the $x-z$ plane (not a $x-z$ cut) of both coordinates. The subsolar point is highlighted in each plot.

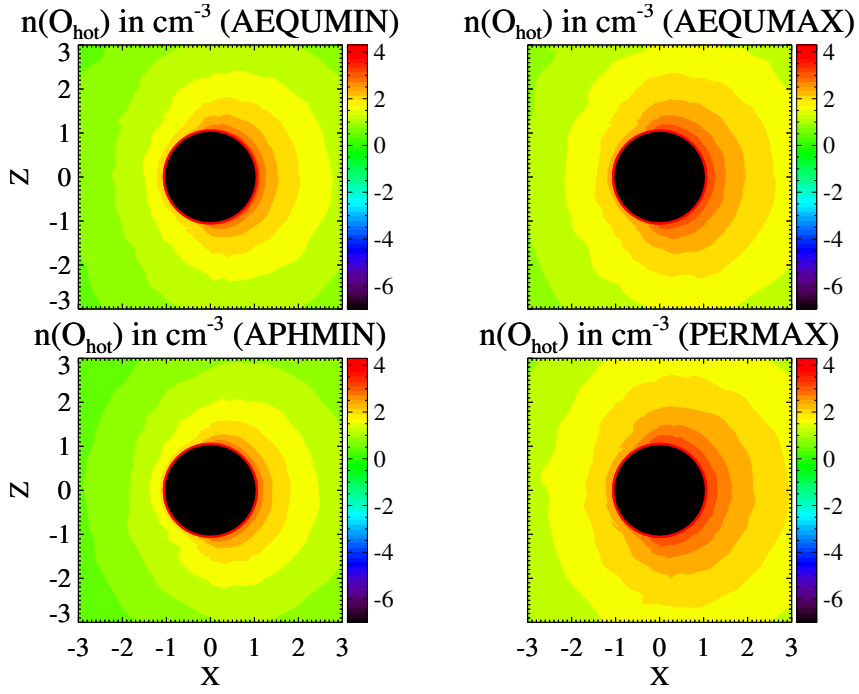

Figure 5.2: A comparison of the M-AMPS output hot oxygen number density (in cm^{-3}) distribution between autumnal equinox solar minimum (AEQUMIN, case 7) and maximum (AEQUMAX, case 10) conditions (upper panel), and aphelion solar minimum (APHMIN, case 1) and perihelion solar maximum (PERMAX, case 16) conditions (bottom panel) in the $x - z$ plane in the MSO coordinate system. All the results are based on the subsolar longitude, SSL = 0. Note the use of a logarithmic scale.

lar maximum (PERMAX, right) conditions. By comparing these four cases, the hot atomic oxygen corona is the most extensive and has the highest O_{hot} abundance for the PERMAX conditions, followed by the AEQUMAX case; the hot atomic oxygen corona for the APHMIN conditions is the weakest. Furthermore, all these plots clearly show the asymmetric features of the hot atomic oxygen distribution, indicating that in order to accurately calculate the ion escape rate, it is important to adopt an appropriate 3-D hot oxygen corona in a plasma code.

5.3 Simulation Results and Discussions

In this section, we discuss the simulation results by implementing the one-way coupling approach, i.e., both the M-GITM and AMPS 3-D outputs are used as the

inputs for the MF-MHD model (Figure 4.1). In order to evaluate the effects of different crustal field orientations, plus various solar cycle and seasonal conditions on the Mars upper atmosphere ion loss, we study 18 standard cases plus four cases without crustal fields. The 18 cases combine three crustal field orientations (subsolar longitude, SSL=0° W, 180° W, 270° W), three Martian seasons (aphelion, autumnal equinox, perihelion) with solar maximum (F10.7=200) and solar minimum (F10.7=70) conditions. Due to the fact that there is no significant difference between vernal equinox and autumnal equinox (the heliospheric distance difference between these two cases is not zero but small), we only study the latter. For all the cases, the solar wind density is set to 4 cm^{-3}, the upstream solar wind plasma temperature is set to 3.5×10^5 K, the interplanetary magnetic field (IMF), **B**, is assumed to be a Parker spiral in the X-Y plane of MSO coordinate system with an angle of 56°, and the solar wind velocity is 400 km/s. Table 5.1 summarizes the cases studied in this chapter.

The calculated ion escape rates (in $\times10^{24}$ s^{-1}) are summarized in Table 5.2 and the corresponding histograms are shown in Figure 5.3. The calculation of ion escape rate is conducted by integrals of the plasma density multiplied by the radial velocity component at the surface of a 6 R_M sphere. The results are quite interesting and several conclusions can be made.

5.3.1 Effects of crustal field orientation

First, the crustal magnetic field has a shielding effect to protect Mars from interacting with the solar wind and is therefore able to reduce the ion escape rates (the same as what we found in Chapter IV). For example, comparison of cases in the AEQUMIN conditions (cases 7-9) shows that case 8 (SSL=180°W, crustal field, B_c, mainly faces the Sun) has the smallest net ion escape rate (O^+, O_2^+ and CO_2^+) and case 7 (SSL=0°W, B_c mainly faces the tail region) has the largest net ion escape

Table 5.1: Input parameters used for different calculations.

Simulation Cases	Subsolar Longitude (SSL)	Solar Cycle Conditions	Seasonal Variations
Case 1	0^oW	Solar Minimum	Aphelion (APH)
Case 2	180^oW	(APHMIN)	
Case 3	270^oW		
Case 4	0^oW	Solar Maximum	
Case 5	180^oW	(APHMAX)	
Case 6	270^oW		
Case 7	0^oW	Solar Minimum	Autumnal Equinox (AEQU)
Case 8	180^oW	(AEQUMIN)	
Case 9	270^oW		
Case 10	0^oW	Solar Maximum	
Case 11	180^oW	(AEQUMAX)	
Case 12	270^oW		
Case 13	0^oW	Solar Minimum	Perihelion (PER)
Case 14	180^oW	(PERMIN)	
Case 15	270^oW		
Case 16	0^oW	Solar Maximum	
Case 17	180^oW	(PERMAX)	
Case 18	270^oW		
Case 19	180^oW	APHMIN	Aphelion and Perihelion comparison with crustal magnetic field turned off
Case 20	180^oW	APHMAX	
Case 21	180^oW	PERMIN	
Case 22	180^oW	PERMAX	

Table 5.2: Calculated ion escape rates (in $\times 10^{24}$ s^{-1}).

Simulation Cases	O^+	O_2^+	CO_2^+	Total	$(O_2^+ + CO_2^+)/O^+$	CO_2^+/Total (%)
Case 1 (APHMINSSL0)	0.30	1.43	0.13	1.86	5.27	6.87
Case 2 (APHMINSSL180)	0.27	1.65	0.20	2.12	6.75	9.30
Case 3 (APHMINSSL270)	0.32	1.70	0.17	2.18	5.90	7.67
1-3 average (APHMIN)	0.30	1.59	0.16	2.05	5.95	7.99
Case 4 (APHMAXSSL0)	3.08	2.84	0.38	6.29	1.04	5.98
Case 5 (APHMAXSSL180)	2.64	2.38	0.41	5.44	1.06	7.63
Case 6 (APHMAXSSL270)	3.17	2.72	0.44	6.33	1.00	6.92
4-6 average (APHMAX)	2.96	2.64	0.41	6.02	1.03	6.81
1-6 average (APH)	1.63	2.12	0.29	4.03	1.48	7.11
Case 7 (AEQUMINSSL0)	0.41	1.68	0.15	2.24	4.42	6.90
Case 8 (AEQUMINSSL180)	0.31	1.12	0.11	1.53	4.01	6.89
Case 9 (AEQUMINSSL270)	0.44	1.45	0.13	2.02	3.60	6.46
7-9 average (AEQUMIN)	0.39	1.42	0.13	1.93	4.00	6.74
Case 10 (AEQUMAXSSL0)	4.57	2.52	0.26	7.35	0.61	3.49
Case 11 (AEQUMAXSSL180)	3.81	1.80	0.24	5.86	0.54	4.16
Case 12 (AEQUMAXSSL270)	4.99	2.17	0.24	7.40	0.48	3.25
10-12 average (AEQUMAX)	4.46	2.17	0.25	6.87	0.54	3.59
7-12 average (AEQU)	2.42	1.79	0.19	4.40	0.82	4.29
Case 13 (PERMINSSL0)	0.49	1.63	0.13	2.25	3.55	5.67
Case 14 (PERMINSSL180)	0.49	1.51	0.14	2.14	3.34	6.57
Case 15 (PERMINSSL270)	0.71	2.06	0.17	2.94	3.16	5.79
13-15 average (PERMIN)	0.56	1.73	0.15	2.44	3.33	5.98
Case 16 (PERMAXSSL0)	5.07	3.08	0.48	8.63	0.70	5.56
Case 17 (PERMAXSSL180)	4.02	2.40	0.38	6.80	0.69	5.62
Case 18 (PERMAXSSL270)	5.51	3.39	0.53	9.43	0.71	5.64
16-18 average (PERMAX)	4.86	2.96	0.46	8.29	0.70	5.61
13-18 average (PER)	2.71	2.35	0.31	5.37	0.98	5.69
1-3 & 7-9 & 13-15 average (SOLARMIN)	0.42	1.58	0.15	2.14	4.16	6.85
4-6 & 10-12 & 16-18 average (SOLARMAX)	4.10	2.59	0.37	7.06	0.72	5.30
1-18 average (ALL)	2.26	2.08	0.26	4.60	1.04	5.66
Case 19 (APHMINSSL180 [no B_c])	0.46	2.13	0.20	2.79	5.09	7.27
Case 20 (APHMAXSSL180 [no B_c])	3.13	2.69	0.43	6.26	1.00	6.94
19-20 average (APH [no B_c])	1.79	2.41	0.32	4.52	1.52	7.04
Case 21 (PERMINSSL180 [no B_c])	0.71	2.24	0.23	3.19	3.47	7.29
Case 22 (PERMAXSSL180 [no B_c])	5.41	2.51	0.56	8.48	0.57	6.58
21-22 average (PER [no B_c])	3.06	2.38	0.40	5.84	0.90	6.78

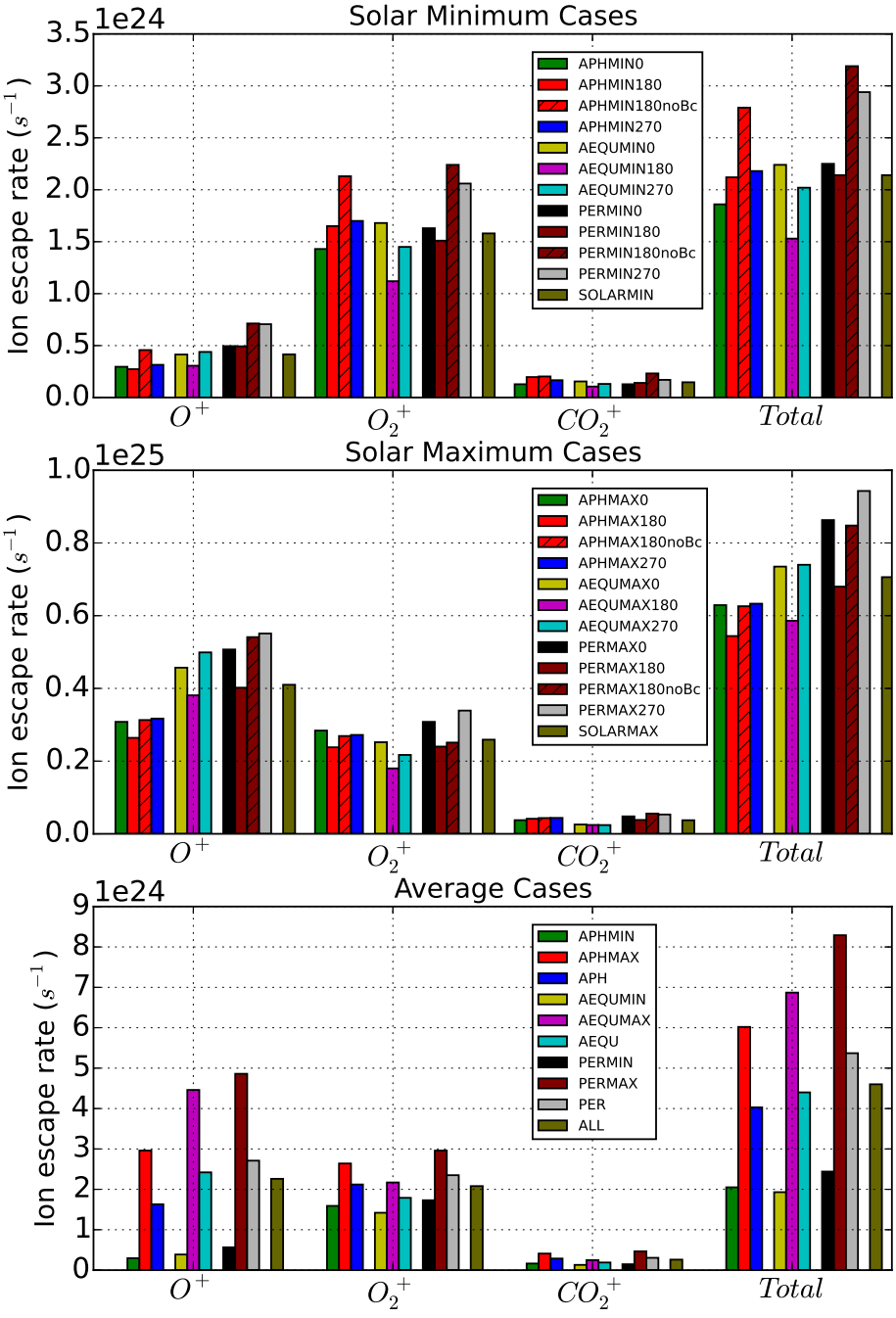

Figure 5.3: The histograms of ion escape rates (in s^{-1}). Upper panel: cases with solar minimum conditions; middle panel: cases with solar maximum conditions; bottom panel: average cases. Noted that the ion escape rate scales in these three plots are different.

rate among these three cases. Interestingly, the same conclusion in Chapter IV is not valid for aphelion and perihelion conditions due to the axial tilt, inhomogenous distribution of the crustal field, and possibly the 3-D atmosphere profiles (e.g., the effect of surface albedo and thermal inertia in M-GITM). For aphelion conditions, even when SSL=180 (cases 2 and 5), the crustal magnetic field is mainly concentrated in the southern hemisphere polar region in the MSO coordinate system (as indicated by Figure 5.1). Therefore, the crustal field does not play a significant role in the solar wind Mars interaction like in the equinox cases. For perihelion conditions, when SSL=180 (cases 14 and 17), the crustal magnetic field is mainly concentrated in the dayside equatorial region (almost exactly facing the Sun). The shielding effect of the crustal field under this circumstance is stronger than those in the equinox cases.

Contrary to our initial expectation, the smallest net escape rate is associated with the AEQUMIN conditions when the crustal magnetic field faces the Sun (case 8, 1.53×10^{24} s^{-1}) instead of the APHMIN conditions with the same crustal field orientation (case 2, 2.12×10^{24} s^{-1}). This behavior indicates that considering only the heliocentric distance or the associated chemical reaction rates is not sufficient to determine the ion escape rates due to the influence of the crustal magnetic field. According to our simulation, case 18 (PERMAX, SSL=270) has the largest net ion escape rate, 9.43×10^{24} s^{-1}. Although the existence of the axial tilt and the potential influence of the 3-D atmosphere can break the simple conclusion we draw for the equinox conditions, overall the crustal field shows a strong shielding effect to prevent the ion loss from the solar wind Mars interaction. It is interesting to point out that both hybrid models (e.g., *Brecht and Ledvina*, 2014a) and other MF-MHD codes (e.g., *Harnett and Winglee*, 2006) also showed that the crustal field has a strong shielding effect to protect Mars from interacting with the solar wind regardless of different model setups and inputs. Meanwhile, *Riousset et al.* (2014) pointed out that the ionospheric outflows are likely to be prevented when the surface and lower

atmospheres are shielded by closed field lines due to the presence of magnetic loops and arcades. Such shielding ultimately reduces the fluxes of ions from the dynamo region to the upper ionosphere and thus reducing the ion escape rate. Furthermore, *Lundin et al.* (2011) reported when the crustal field faces the sun, it has an effect to deviate the dayside ion flow and thus reducing the tailward transport and escape of ionospheric plasma by analyzing the ASPERA-3 data from MEX.

5.3.2 Effects of seasonal variations

Second, by averaging over different crustal field orientations and solar cycle conditions, we found that aphelion conditions (APH) are associated with a net ion escape rate of 4.03×10^{24} s^{-1}, autumnal equinox conditions (AEQU) are associated with a net ion escape rate of 4.40×10^{24} s^{-1}, and perihelion conditions (PER) yield an increased net ion escape rate up to 5.37×10^{24} s^{-1}. As expected, perihelion has the largest net ion escape rate and aphelion has the smallest total ion loss rate. According to the values mentioned above, the seasonal variations may cause a factor of ~ 1.33 variation in the ion loss rate.

Although we try to eliminate the effect of crustal field when estimating the ion escape affected by seasonal variations alone, the crustal field still has a potential effect on the results due to the axial tilt. In other words, the seasonal variations and crustal magnetic field orientations are closely connected with each other, and may not be simply decoupled by averaging over different B_c orientations and solar cycles. With different crustal field orientations but the same solar cycle and seasonal conditions, we calculated the ratio of maximum net ion loss to minimum ion loss (Table 5.3) for APHMIN (2.18/1.86∼1.17), APHMAX (6.33/5.44∼1.16), and the average of APHMIN and APHMAX, APH (∼1.17); AEQUMIN (2.24/1.53∼1.46), AEQUMAX (7.40/5.86∼1.26) and AEQU (∼1.36); PERMIN (2.94/2.14∼1.37), PERMAX (9.43/6.80∼1.39) and PER (∼1.38). Based on the results, we could easily prove

Table 5.3: Maximum ($\mathcal{R}_{max}$) and minimum ($\mathcal{R}_{min}$) ion escape rates (in $\times 10^{24}$ s^{-1}), and the corresponding ratio ($\mathcal{R}_{max}/\mathcal{R}_{min}$) for different seasons.

	APHMIN	APHMAX	AEQUMIN	AEQUMAX	PERMIN	PERMAX
Maximum escape rate ($\mathcal{R}_{max}$)	2.18	6.33	2.24	7.40	2.94	9.43
Minimum escape rate ($\mathcal{R}_{min}$)	1.86	5.44	1.53	5.86	2.14	6.80
Corresponding ratio ($\mathcal{R}_{max}/\mathcal{R}_{min}$)	1.17	1.16	1.46	1.26	1.37	1.39
Average over solar cycle (ratio)	1.17 (APH)		1.36 (AEQU)		1.38 (PER)	

that the shielding effect of crustal field are significantly correlated with season. Figure 5.3 may help to illustrate this conclusion in a more intuitive way. The crustal field has a more significant shielding effect for perihelion conditions than for the aphelion conditions due to the axial tilt.

In order to investigate the seasonal control of the ion loss more accurately, we calculated four more cases without the crustal magnetic field: APHMIN, APHMAX, PERMIN and PERMAX, in which all SSL=180 °W. Surprisingly, we obtained a factor of ~ 1.29 variation in the ion escape due to different seasons, which is only slightly smaller (within 5%) than the previous estimate ~ 1.33, based on the average of results obtained with three crustal field orientations. Therefore, it may be appropriate to estimate the seasonal control of the ion loss by averaging over different crustal field orientations, but further investigations with more crustal field orientations or a real-time case are needed to verify this argument. Compared with the corresponding cases with crustal magnetic fields, all the ion escape rates increase (also see Figure 5.3) when crustal field is turned off, consistent with the first conclusion drawn above. On the other hand, the ion escape rate of case 18 is generally higher than that of case 22, implying that the crustal field may also help ions to escape from the Martian upper atmosphere under certain circumstances, e.g., magnetic reconnection. The results may also be caused by the different M-GITM atmospheric profiles (with different subsolar longitudes) used in these two cases. Currently, surface albedo and thermal inertia are the only two parameters implemented into M-GITM that can affect atmospheric profiles during Mars' rotation (*Bougher et al.*, 2015a). Although these two parameters may affect the upper atmosphere profile to some extent, they

are more important for the lower atmospheric structure via the radiative transfer process. At present, M-GITM does not include surface topography.

5.3.3 Effects of solar cycle conditions

Third, by averaging over different crustal field orientations and seasonal variations, we obtained that the net ion escape rate for solar maximum conditions (SOLARMAX, 7.06×10^{24} s^{-1}) is about 3.3 times higher than that of solar minimum conditions (SOLARMIN, 2.14×10^{24} s^{-1}). In other words, different solar cycles can affect the ion escape rate by a factor of $\sim$ 3.3 based on our simulations. Our calculated total ion escape rate for SOLARMIN conditions is $\sim 2\times10^{24}$ s^{-1}, in reasonable agreement with the MEX data as shown in Figure 4 in *Lundin et al.* (2013). For SOLARMAX conditions, the calculated result is 7.06 $\times10^{24}$ s^{-1}, which is also reasonably consistent with the ion escape rate estimate from MEX data, $\sim 1\times10^{25}$ s^{-1} (*Lundin et al.*, 2013). The increasing trend of the ion escape rate with solar activity is somewhat different from that reported by *Lundin et al.* (2013) (a factor of $\sim$ 10). One possible explanation is that we did not include the neutral winds in our simulations, which can greatly affect the ion loss (*Brecht and Ledvina*, 2014b). On the other hand, the recent paper published by *Ramstad et al.* (2015) showed that the solar wind density and velocity can greatly affect the ratio of escape rate between low and high solar EUV conditions. They adopted more than seven years of ion flux measurements in the energy range 10 eV–15 keV from ASPERA-3/IMA instrument on board MEX. As shown in their Figure 5, it is clear that based on our simulation parameters (solar wind velocity 400 km and solar wind density 4 cm^{-3}), the escape rate ratio is less than a factor of 10.

A careful analysis of individual mass spectra in *Lundin et al.* (2009) shows that the CO_2^+ contribution to the low-energy ($<$ 300 eV) heavy ion outflow is $\leq$ 10%. On average, our CO_2^+ ion contribution to the total ion escape (O^+, O_2^+ and CO_2^+) is

about 6.85% for SOLARMIN conditions and 5.30% for SOLARMAX conditions; both these values and the ratio from ALL conditions (as shown in Table 5.2, $\sim 5.66\%$) are consistent with the observations ($< 10\%$). *Nilsson et al.* (2011) pointed out that the average flux ratio of the molecular species (O_2^+ and CO_2^+) to O^+ ions is 0.9 ± 0.1 based on the statistics of MEX data from May 2007 to May 2011 for ion energies below 50 eV. Our escape rate ratio of molecular (O_2^+ and CO_2^+) to O^+ ions varies case by case as shown in Table 5.2. Since the estimate by *Nilsson et al.* (2011) is based upon a four-year average, the calculated ratio should be independent of seasonal variations given the fact that one Martian year is approximately equal to two Earth's years. Based on our calculations, this ratio is ~ 4.16 for SOLARMIN conditions and 0.72 for SOLARMAX conditions. The average over solar cycles leads to a ratio of 1.04 (ALL conditions as shown in Table 5.2), in reasonable agreement with the MEX data. The MEX data used in previous studies (*Nilsson et al.*, 2011) was collected only from low solar activity to moderate level, but our result is based on the average over two solar cycle conditions. The other important factor that can lead to a difference is that their estimate of the flux ratio was based on ion energies below 50 eV, while our calculations include ions from all energy ranges. The low energy limit in their calculation underestimates the high energy escape ions. It is noteworthy that although M-GITM and M-AMPS provide the MF-MHD code with more realistic 3-D cold and hot neutral atmosphere profiles (Figure 5.1 and Figure 5.2), currently there are few accurate measurements of the (thermal and suprathermal) oxygen profiles in the Mars atmosphere (*Bougher et al.*, 2014). This uncertainty affects the calculated ion escape rates. Therefore, the neutral atmosphere profiles to be returned by the MAVEN mission will significantly reduce the uncertainty in calculated escape rates resulting from the lack of direct information regarding the cold and hot oxygen abundances.

Figure 5.4 shows a comparison of H^+, O_2^+ and O^+ ion escape plumes in the $x - z$ plane of the MSO coordinate system for two extreme cases: APHMIN (case 1) and

PERMAX (case 18). The main feature of the MF-MHD model is the asymmetric escape plume for heavy ion (O^+, O_2^+) species. The lack of significant escape plume for H^+ ions is because of its small mass (and thus small gyroradius) and the fact that the solar wind and ionospheric protons are combined in the model (*Najib et al.*, 2011). From Figure 5.4, it is not difficult to distinguish the aphelion case from the perihelion case according to the different strengths of the ion escape plume, primarily caused by different solar radiation. The upper panel is associated with aphelion conditions which has a weaker ion escape plume than the bottom panel for perihelion conditions, especially when focusing on the hot oxygen corona region of the contour plot. The contour plots shown in Figure 5.4 are also consistent with the hot oxygen profiles shown in Figure 5.2 and the ion escape rates shown in Table 5.2.

5.3.4 Effects of mass differentiation

Last but not least, all the ion escape rates show a positive linear correlation with each other (Figure 5.5). The cold heavy ionospheric molecular ion escape fraction [(O_2^+ and/or CO_2^+)/Total] is inversely proportional to the atomic ion escape fraction [O^+/Total], whereas O_2^+ and CO_2^+ ion escape fractions show a positive linear correlation (Figure 5.6). The escape fraction is defined as the escape rate ratio between an individual or sum of several ion species to total ions. The positive linear correlation in Figure 5.5 is mainly caused by the fact that an increase in solar irradiance leads to a higher amount of ionized gas via photoionization. Although the perfect linear anti-correlation in Figure 5.6 (d) is mathematically to be expected, all the linear correlations indicated in Figure 5.6 can also be physically interpreted. As we mentioned above, Mars has a solar cycle dependent hot atomic oxygen corona (see Figure 5.2), which is ionized by the solar radiation and the solar wind electrons via photoionization and electron impact ionization, respectively. The ionized O^+ can be picked up by the solar wind and escape from the Martian upper atmosphere. The

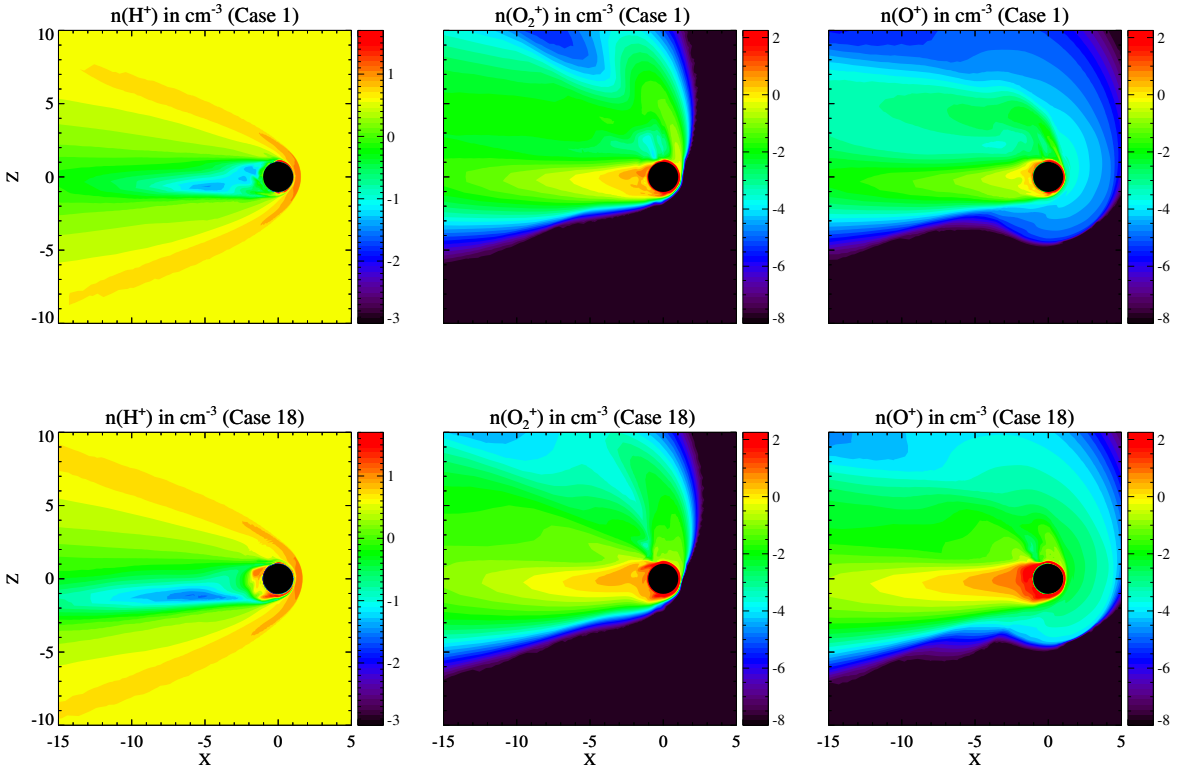

Figure 5.4: The calculated ion number densities in cm^{-3} in the $x-z$ plane for H^+, O_2^+, and O^+ in a logarithmic scale. Case 1 is shown in the upper panels and case 18 is shown in the bottom panels. Noted that the logarithmic scales in different plots are different. The direction of the solar wind is parallel to the x-axis and in the $-x$ direction.

mass loading process reduces the solar wind speed and the dynamic pressure, and thus the solar wind has a reduced opportunity to penetrate deeply into the Martian ionosphere mainly due to the momentum conservation. As a result, the cold heavy ionospheric molecular ions (O_2^+ and CO_2^+) are relatively less affected by the solar wind and the associated ion escape rate fraction [(O_2^+ + CO_2^+)/Total] is decreased. Besides, the ionized hot oxygen corona behaves approximately as a perfect conductor and therefore prevents the electric and magnetic fields from penetrating into the Martian ionosphere to a certain degree. Both the mass loading and electromagnetic shielding contribute to the inverse correlation between the cold heavy ionospheric molecular ion escape fraction [(O_2^+ and/or CO_2^+)/Total] and the atomic ion escape fraction [O^+/Total]. Meanwhile, O_2^+ and CO_2^+ ion escape fractions (ionospheric ion outflow) show a positive linear correlation (r-value=0.68) because both species are originated from the cold Martian ionosphere and should follow the same escape path. In order to avoid any artificial factor resulting from both the small datasets and missing the solar moderate cases, we decided to adopt the linear regression rather than a cubic polynomial regression fit to increase the correlation coefficient (r-value). In the future work, we plan to add the datasets from the solar moderate cases for the linear regression, most of which should lie in the middle of Figures 5.5 and 5.6, and thus may help increase the r-value.

In Figures 5.5 and 5.6, the calculated ion escape rates and the ion escape rate fractions (with respect to the total ion loss) associated with solar minimum and solar maximum conditions are indicated by the red circle and blue square markers, respectively. The corresponding mean values are highlighted by the green markers with the same shape in both Figures. The least squares polynomial linear fit of the simulation results based on cases 1-18 (2 average green points are not included) is shown in each figure as well. Correlations among different ion escape rates and the corresponding correlations among their fractions for different solar cycle conditions

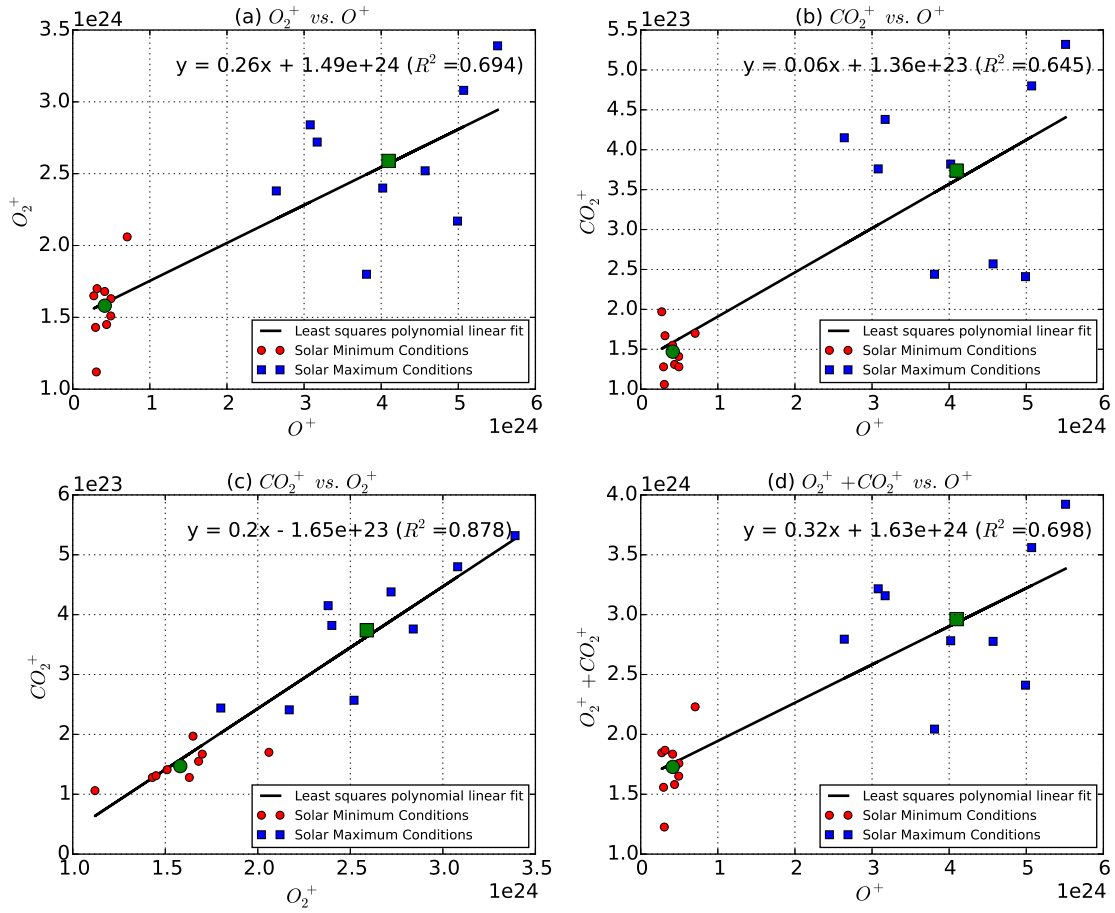

Figure 5.5: Least squares polynomial linear fit of the simulation results based on cases 1-18. The calculated ion escape rates associated with solar minimum and solar maximum conditions are indicated by the red circle and blue square markers, respectively. The corresponding mean values are highlighted by the green markers with the same shape.

help us to understand the physics behind the regression lines. For example, during the period of high solar activity, Mars has a more extensive hot oxygen corona (see Figure 5.2), so the O^+ ion escape fraction is relatively large in Figure 5.6 (mainly distributed in the lower right corner when O^+/Total is the horizontal axis) while the cold heavy ionospheric molecular ion escape fraction is relatively small. The associated statistical details, e.g., slope and intercept of the regression line, correlation coefficient (r-value), coefficient of determination (r-squared, R^2), two-sided p-value and standard error of the estimate (stderr) are shown in Table 5.4.

The r-value is a measure of the linear correlation (dependence) between two vari-

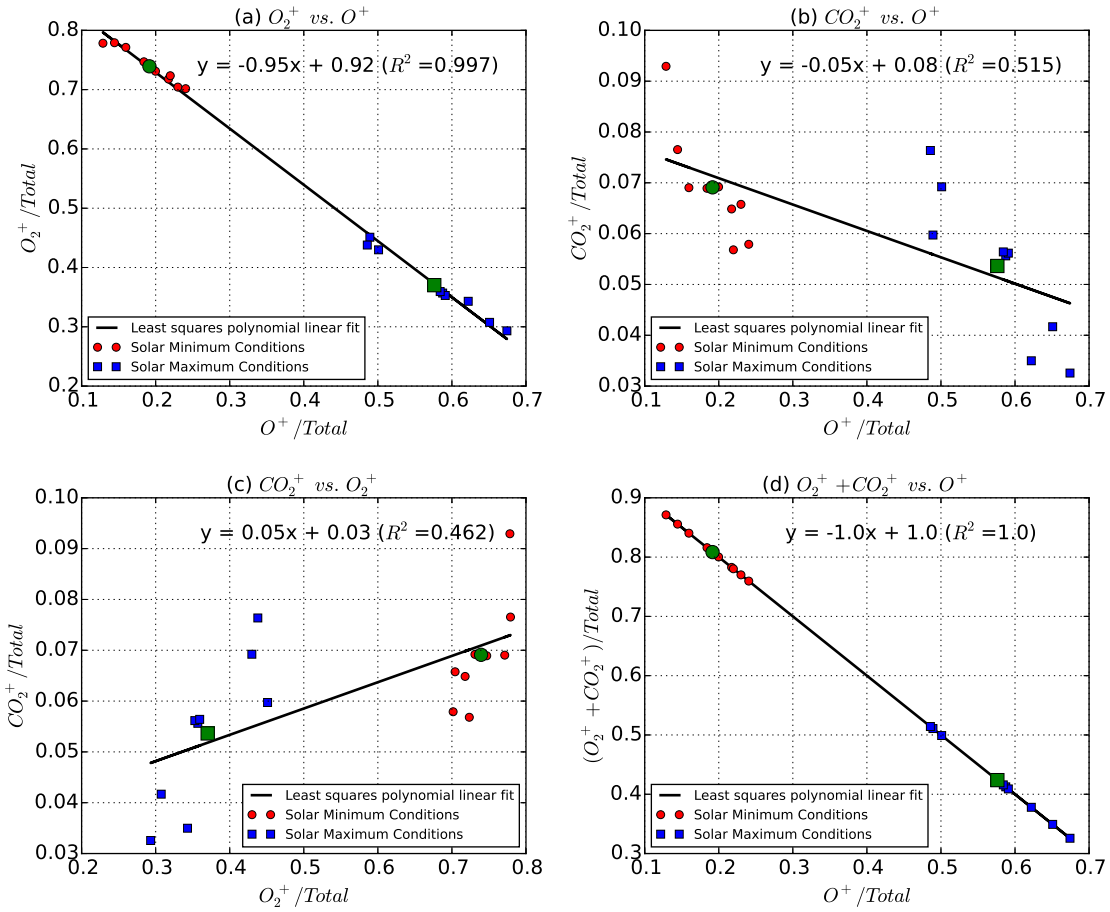

Figure 5.6: Least squares polynomial linear fit of the simulation results based on cases 1-18. The calculated ion escape rate fractions (with respect to the net ion loss) associated with solar minimum and solar maximum conditions are indicated by the red circle and blue square markers, respectively. The corresponding mean values are highlighted by the green markers with the same shape. Although the perfect linear anti-correlation in Figure 5.6 (d) is mathematically to be expected, all the linear correlations indicated in Figure 5.6 can also be physically interpreted.

Table 5.4: Slope and intercept of the regression line shown in Figure 5.6, correlation coefficient (r-value), coefficient of determination (r-squared, R^2), two-sided p-value for a hypothesis test whose null hypothesis is that the slope is zero, standard error of the estimate (stderr).

	slope	intercept	r-value	R^2	p-value	stderr
O_2^+ *vs.* O^+	0.264	1.49×10^{24}	0.833	0.694	1.776×10^{-5}	0.0438
CO_2^+ *vs.* O^+	0.0553	1.357×10^{23}	0.803	0.645	5.949×10^{-5}	0.0103
CO_2^+ *vs.* O_2^+	0.204	-1.647×10^{23}	0.937	0.878	9.95×10^{-9}	0.019
O_2^+ + CO_2^+ *vs.* O^+	0.319	1.626×10^{24}	0.835	0.698	1.592×10^{-5}	0.0525
O_2^+ *vs.* O^+ (fraction)	-0.948	0.919	-0.999	0.997	7.791×10^{-22}	0.0126
CO_2^+ *vs.* O^+ (fraction)	-0.052	0.081	-0.718	0.515	8.015×10^{-4}	0.0126
CO_2^+ *vs.* O_2^+ (fraction)	0.052	0.033	0.680	0.462	1.922×10^{-3}	0.014
O_2^+ + CO_2^+ *vs.* O^+ (fraction)	-1.0	1.0	-1.0	1.0	5.027×10^{-159}	0.0

ables X and Y, giving a value between +1 and -1, where 1 is total positive correlation, 0 is no correlation, and -1 is total negative correlation. It is defined as the (sample) covariance of the variables divided by the product of their (sample) standard deviations. The coefficient of determination, denoted R^2 or r^2, is a number that indicates how well data fits a statistical model. The two-sided p-value indicates the probability of the correlation occurring by random chance. The standard error of the estimate (stderr) represents the average distance that the observed values fall from the regression line. Conveniently, it tells you how wrong the regression model is on average using the units of the response variable. Smaller values are better because it indicates that the observations are closer to the fit line. The linear correlation in Figures 5.5 and 5.6 is very useful when one does not have all the ion escape information and/or the spacecraft instrument mass resolution is not high enough to distinguish ion species, *e.g.*, O^+ and O_2^+. Knowing the total ion and O^+ ion escape rates, the cold heavy ionospheric molecular ion escape rate can simply be calculated based on the linear fits shown in Figure 5.6 (d). If one needs to distinguish between O_2^+ and CO_2^+, the linear fit in the plot of CO_2^+ versus O_2^+ (Figure 5.5 (c)) can be used.

Due to different model setups and inputs, it is inappropriate to quantitatively compare our simulation results with the previous similar case studies (e.g., *Harnett and Winglee*, 2006; *Brecht and Ledvina*, 2014a) because MEX observations show that the solar wind density and velocity can greatly affect the ion escape rates (*Ramstad et al.*, 2015). By adopting a 1-D O corona, *Brecht and Ledvina* (2014a) found that O_2^+ is always the dominant escape ion regardless of solar cycles and the presence of crustal fields, whereas our simulations show this conclusion only holds true during AEQUMIN conditions. It is also noteworthy that *Brecht and Ledvina* (2014b) showed that the ion escape rates can be greatly enhanced by including the neutral wind in a hybrid model. This neutral wind effect is not yet incorporated into the MF-MHD code but will be implemented in future work.

5.4 Conclusions

In summary, the work in this chapter aims to build a model library for the MAVEN mission (2014-2016). We studied the solar wind interaction with the Martian upper atmosphere by using one-way coupling of three comprehensive 3-D models (the same approach as described in Chapter IV). The effects of crustal field orientation, solar cycle and seasonal variations on the Martian upper atmosphere ion escape are investigated in detail by comparing 22 cases. Different solar cycles can affect the ion loss by a factor of ~ 3.3, while different seasons can vary the ion loss by a factor of ~ 1.3. The coexistence of crustal field and axial tilt lead to a quite intricate solar wind-Mars interaction. There is no simple conclusion that a certain crustal magnetic field orientation can lead to the smallest ion escape rate as found in previous studies (e.g. *Ma and Nagy* (2007a)). Instead, in this study, we found that the smallest ion escape rate also depends on the seasonal variations due to the axial tilt and the 3-D atmospheric structure. Overall, it is clear that the crustal magnetic field has a shielding effect to protect Mars from interacting with the solar wind, and this effect is the strongest for perihelion conditions with the crustal field facing the Sun. Furthermore, the cold heavy ionospheric molecular ion escape fraction [(O_2^+ and/or CO_2^+)/Total] is inversely proportional to the atomic ion escape fraction [O^+/Total]. On the other hand, O_2^+ and CO_2^+ ion escape fractions (ionospheric ion outflow) show a positive linear correlation.

Contrary to our initial expectation, the smallest total ion escape rate is associated with the autumnal equinox solar minimum (AEQUMIN) case instead of the aphelion solar minimum (APHMIN) case, again due to the effect of coexisting crustal field and axial tilt plus the 3-D atmosphere. Based on averages over different solar cycles and various crustal field orientations, perihelion conditions yield the highest total ion escape rate and aphelion conditions yield the lowest total ion escape rate, which is well within our expectations. The calculated ion escape rates are in reasonable agreement

with the recent observational data from MEX. For solar minimum conditions, the total ion (O^+, O_2^+ and CO_2^+) escape rate is around 2.0×10^{24} s^{-1} and for solar maximum conditions, the net ion loss is 7.06 $\times10^{24}$ s^{-1}. By averaging our 18 MHD model cases, we obtained CO_2^+/Total ($\sim$ 5.66%) and (CO_2^++O_2^+)/O^+ ($\sim$ 1.04), which are reasonably consistent with the statistical results from 4-year MEX observational data.

In the next chapter, we will study the passage of a powerful interplanetary coronal mass ejection (ICME) at Mars that drove a significant response from Mars' atmosphere and its ambient space plasma environment on March 8th, 2015 (*Jakosky et al.*, 2015b). This ICME0308 event has been observed by the MAVEN instruments. A detailed data-model comparison will be shown to 1) further validate the multi-fluid MHD model, and 2) help the community to better understand the Martian upper atmosphere response to the (extreme) variation in the solar wind and its interplanetary environment from a global perspective. In addition, we will also show a data-model comparison of the Martian ionospheric ion densities between the MAVEN measurements and the MF-MHD simulations during the second MAVEN Deep Dip campaign.

CHAPTER VI

Multi-fluid MHD study of the solar wind interaction with Mars' upper atmosphere during the 2015 March 8 ICME event and the MAVEN Deep Dip campaign

6.1 Introduction

Unmagnetized planets, like Mars, are especially susceptible to atmospheric scavenging because the solar wind can interact directly with the upper atmosphere due to the lack of an intrinsic dipole magnetic field. Recently, MAVEN observed a powerful ICME arrived at Mars at approximately 15:22 Universal Time (UT) on March 8th, 2015, which drove a significant response from the Martian space plasma environment (*Jakosky et al.*, 2015b). Besides, MAVEN made the first comprehensive measurements of Martian thermosphere and ionosphere composition, structure, and variability at altitudes down to ∼130 km in the subsolar region during the second of its unique Deep Dip campaigns this April (*Bougher et al.*, 2015b). This chapter aims to study the solar wind-Mars interaction during the ICME0308 event and the Deep-Dip campaign by using a global multi-fluid MHD model. In order to investigate and understand the Martian global response to the ICME0308 event, we did a detailed data-model

comparison, mainly using data from the Solar Wind Ion Analyzer (SWIA) (*Halekas et al.*, 2015), Magnetometer (MAG) (*Connerney et al.*, 2015), and Neutral Gas and Ion Mass Spectrometer (NGIMS) (*Mahaffy et al.*, 2014) instruments. We also presented a data-model comparison of the Martian ionospheric ion densities between the NGIMS measurements and the MF-MHD simulations during the second MAVEN Deep Dip campaign.

SWIA is a part of the Particles and Fields (P & F) Package and measures the solar wind and magnetosheath proton flow around Mars and constrains the nature of solar wind interactions with the upper atmosphere. In order to determine the energy input to the upper atmosphere, the charge exchange rate, and the bulk plasma flow from solar wind speeds (∼350 to ∼1000 km/s) down to stagnating magnetosheath speeds (tens of km/s), SWIA measures the properties of solar wind and magnetosheath ions, including density, temperature, and velocity (*Halekas et al.*, 2015). The magnetometer is also a part of the Particles and Fields (P & F) Package and measures interplanetary solar wind and ionospheric magnetic fields. MAG measures the vector magnetic field in the unperturbed solar wind (B $\sim$ 3 nT), magnetosheath (B $\sim$ 10-50 nT), and crustal magnetospheres (B $<$ 3000 nT), with the ability to spatially resolve crustal magnetic cusps (horizontal length scales of $\sim$ 100 km) (*Connerney et al.*, 2015). NGIMS measures the composition and isotopes of thermal neutrals and ions. Specifically, NGIMS measures the basic structure of the upper atmosphere (major species He, N, O, CO, N_2, NO, O_2, Ar, and CO_2) and ionosphere from the homopause to above the exobase. It also measures stable isotope ratios, and variations (*Mahaffy et al.*, 2014).

In this chapter, we chose four cases to study for the observed ICME event. One is during a quiet period before the ICME (Case 1: pre-ICME phase), the other three are at different stages after the ICME arrival (Cases 2: early sheath phase, Case 3: late sheath phase, and Case 4: ejecta phase). For the data-model comparisons during the

second MAVEN Deep Dip campaign, we chose two orbits to study: O1069 (DeepDip1 on 19-April-2015) and O1085 (DeepDip2 on 22-April-2015).

6.2 Model and inputs

We use the multi-fluid MHD model with the M-GITM neutral atmosphere inputs in this study (read Chapter IV for more details). In order to evaluate the Martian response to different stages of the ICME, we studied four cases corresponding to four successive orbits, from orbit 848 (O848) to orbit 851 (O851). Case 1 corresponds to the pre-ICME condition, Case 2 and Case 3 correspond to the early and late sheath phases (solar wind density, velocity and IMF strength all increase, but the late sheath phase has the greatest compression), and Case 4 corresponds to the ejecta phase (maintain the strong field and solar wind velocity in the sheath phase, but the ion density drops down). The upstream solar wind density and velocity are taken from the SWIA instrument average over the time period when MAVEN was in the solar wind. The interplanetary magnetic field (IMF) is based on the MAG measurements averaged over the same time period. Table 6.1 summarizes the parameters used for the four cases. It is noteworthy that the solar wind and IMF inputs for the MF-MHD code are based on the average over the time period listed in the second row of Table 6.1, while the crustal field orientations are based upon the periapsis time of each orbit. Unfortunately, MAVEN was not in the solar wind during the Deep Dip campaign, and thus do not have in-situ measurements of the solar wind and IMF parameters. We adopted the approximate solar wind velocity and density (U_x, N_{sw}) from SWIA instrument leader that equal to (-279 km/s, 61 cm^{-3}) and (-500 km/s, 1.1 cm^{-3}) for DeepDip1 and DeepDip2, respectively. We assume IMF as a 56° Parker spiral in the $x-z$ plane for Deep Dip as well. We use the 60 degree harmonic expansion for the crustal magnetic field developed by *Arkani-Hamed* (2001) to describe the observed fields at Mars (*Acuña et al.*, 1999).

Table 6.1: Input parameters and calculated ion escape rates for different cases (in $\times 10^{24}$ s^{-1}).

Simulation Cases (Orbit #)	Case 1 (O848)	Case 2 (O849)	Case 3 (O850)	Case 4 (O851)
Time Period[a]	11:30-11:45	16:25-16:55	20:45-21:15	01:10-01:30
N_{SW} (cm^{-3})	1.9	3.0	11.9	4.5
B_{IMF} (nT)	(-2.1,3.1,-1.0)	(-8.4,-3.3,-8.7)	(5.2,5.4,1.7)	(18.1,7.6,-0.8)
U_{SW} (km/sec)	(-510.4,19.6,-5)	(-830,141,-18)	(-825,62.9,-5.8)	(-800,-45,-10)
Periapsis Time[b]	2015-03-08T13:22:53	2015-03-08T17:53:22	2015-03-08T22:23:53	2015-03-09T02:54:24
Subsolar position (long, lat)	(81.86,-20.55)	(16.06,-20.52)	(-49.74,-20.49)	(-115.54,-20.46)
O^+ ion escape rate	0.60	0.72	1.92	0.92
O_2^+ ion escape rate	1.28	4.40	18.7	6.37
CO_2^+ ion escape rate	0.17	0.51	1.88	0.81
Total ion escape rate	2.05	5.62	22.5	8.10

[a] The time period for this study is from 2015-03-08 (Case 1–3) to 2015-03-09 (Case 4). The solar wind and IMF inputs are based on the average over these four time periods. Given that the case studies here are based on steady state simulations, we slightly modified the solar wind and IMF parameters (<5%, except the change of $B_{IMF,z}$ in Case 1 from -3.0 nT to -1.0 nT) in order to match the bow shock location. The solar wind variability makes the average values not necessarily the correct ones to use for our simulations, but overall the values listed above are close to the real solar wind and IMF data.
[b] The crustal field orientation is based on the periapsis time of each orbit.

6.3 March 8th ICME event

6.3.1 Data-model comparison and model validation

IIn order to validate our model calculations, we first compared the MF-MHD simulation results with the MAVEN data. Since we ran four steady state cases, each simulation can produce the results along the MAVEN trajectories from orbit 848 (O848) to orbit 851 (O851). In Figure 6.1, simulation results from different cases are shown in different background colors. The magenta line shows the ICME arrival time (∼15:22 UT).

The first panel of Figure 6.1 displays the MAVEN trajectories. The dash-dotted black, dashed green and solid red curves represent the latitude, solar zenith angle (SZA), and altitude of MAVEN trajectories, respectively. These three parameters are adequate to locate the MAVEN position with respect to Mars. The second panel of Figure 6.1 compares the calculated ion densities (dashed black n_i and solid red $n_{O_2^+}$ curves) with the SWIA (dotted blue line) and NGIMS (magenta circle marker) densities, which are in good agreement. It is noteworthy that SWIA has no mass resolution (*Halekas et al.*, 2015), so it cannot distinguish different ion species. In addition, only two orbits (O849 and O851) of the NGMIS ion densities were measured

because the ion mode is turned on with the closed source mode (measuring, *e.g.*, Ar, CO_2, O_2, NO, and He) on every other orbit (*Mahaffy et al.*, 2014).

In the third panel of Figure 6.1, we compare the solar wind velocity from the SWIA instrument (solid line) with the MF-MHD results (dashed line), which again are quite consistent. The nearly perfect match for U_x indicates that the MF-MHD code captures the right bow shock location as observed by SWIA. Comparisons of the MF-MHD calculations (dashed line) and the MAG data (solid line) are shown in the next three panels, which are also consistent with each other. The solid red curve (in the bottom panel) represents the calculated Martian crustal field strength, demonstrating that the increase of magnetic field strength near periapsis is mainly caused by the localized crustal field. The good agreement between the MF-MHD calculations and MAVEN data in all panels of Figure 6.1 indicates that the MF-MHD model can reproduce most of the features observed by MAVEN, thus validating its estimate of ion escape rates that will be shown in the following paragraphs.

Figure 6.2 presents a detailed data-model comparison on the orbits where NGIMS ion data are available. All four simulation results along orbits 849 and 851 are plotted in Figure 6.2 in order to demonstrate the little influence of different ICME phases on the model ion distribution (at altitudes $\lesssim 200$ km, where the background ion density is very large) and its comparison with the data. Overall, the model results are consistent with the NGIMS data. The whole Martian ionosphere response to this ICME event, however, needs to be further investigated by a time-dependent simulation in a future study.

6.3.2 Ion escape plume and ion loss rate

The multi-fluid MHD model can simulate the dayside ion escape plumes by considering the dynamics of individual ion species. The asymmetry is primarily caused by different Lorentz forces acting on each ion species. Combined with the generalized

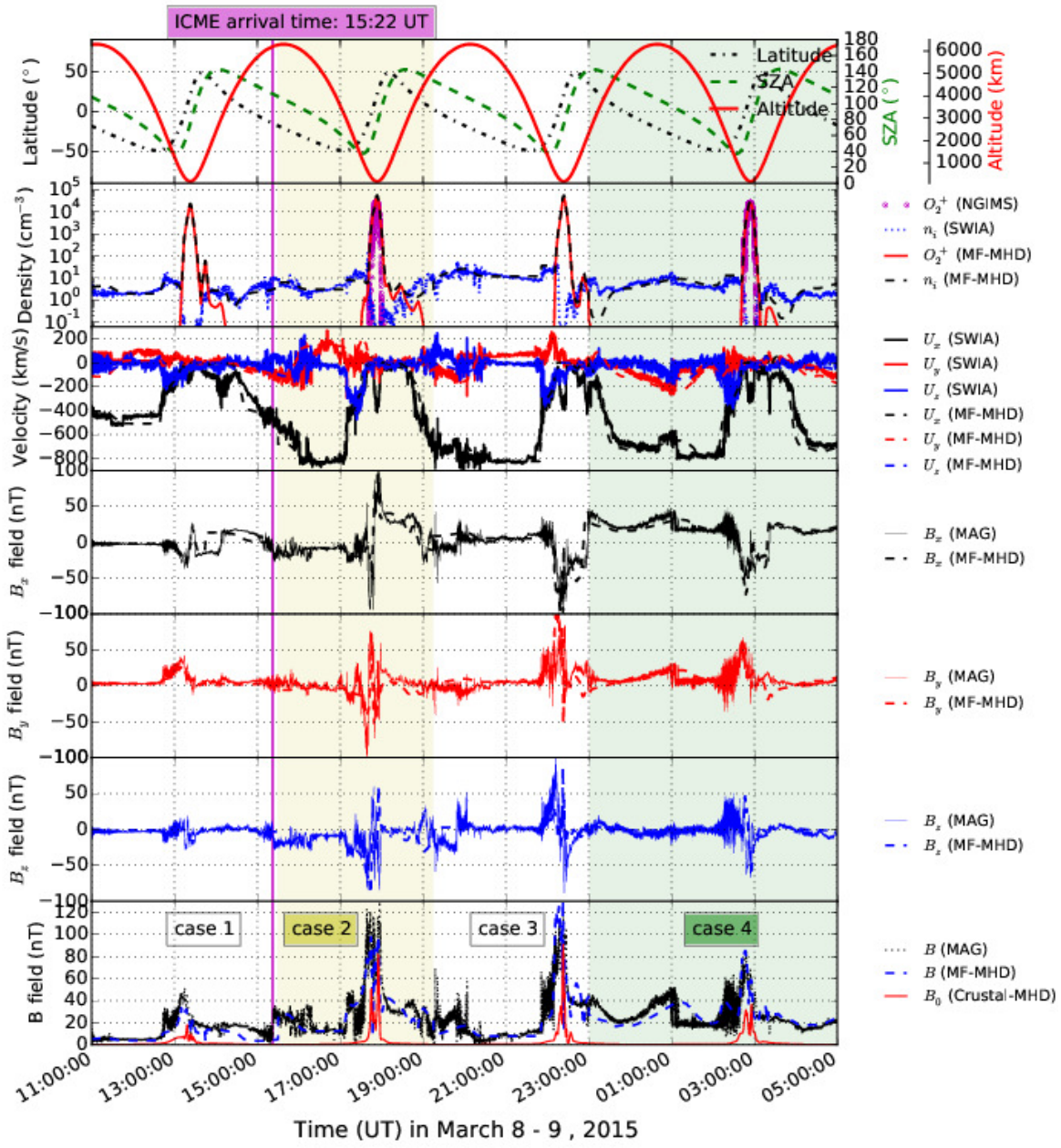

Figure 6.1: Data-model comparison of O_2^+ ion density, solar wind density and velocity, and magnetic field using the NGIMS, SWIA, and MAG data.

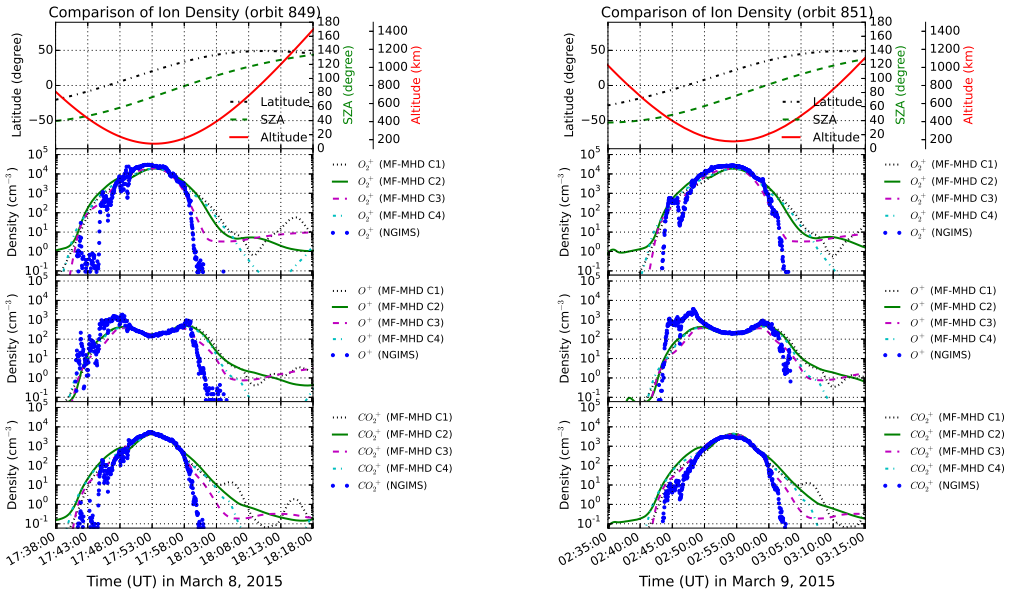

Figure 6.2: Data-model comparison of ionospheric ion density profiles by using NGIMS ion data. Case 1: black dotted curve, Case 2: solid green curve, Case 3: dashed magenta curve, and Case 4: dash-dotted cyan curve.

Ohm's law, the Lorentz force term in the ion momentum equations, $n_s q_s(\mathbf{u_s} \times \mathbf{B} + \mathbf{E})$ can be reformatted, among which the term $n_s q_s(\mathbf{u_s} - \mathbf{u}_+) \times \mathbf{B}$ is the main force to accelerate the planetary pickup ions and cause an asymmetric ion escape plume in the plane perpendicular to the magnetic field vector (*Dong et al.*, 2014). Here n_s, q_s, $\mathbf{u_s}$ are the ion fluid number density, charge, and velocity of the species s, respectively. $\mathbf{E}$ $(=-\mathbf{u}_+ \times \mathbf{B})$ and $\mathbf{B}$ denote the electric and magnetic fields, and $\mathbf{u}_+ = \sum_s n_s q_s \mathbf{u_s}/(en_e)$ is the charge averaged ion velocity. The pickup ion first accelerated by the electric field $\mathbf{E} = -\mathbf{u}_+ \times \mathbf{B}$, and then deflected by the $\mathbf{u_s} \times \mathbf{B}$ force the ion reaches (at most) twice the solar wind velocity (u_{sw}) before turning back and then being decelerated towards the cusp. Interestingly, it has been shown that a multi-fluid MHD model can partially reproduce some major features obtained with a hybrid code, such as the gyration of the planetary/cometary heavy ions and the associated pickup process (*Rubin et al.*, 2014). The characteristic spatial scale, $\sim L_g$, associated with the asymmetry

is controlled by the ratio $m_s u_{sw}/(q_s B)$ via dimensional analysis, at which the ion is fully picked up (*Dong et al.*, 2014). In a kinetic particle model, this characteristic length is essentially the ion gyroradius (e.g., *Dong et al.*, 2013; *Curry et al.*, 2014), but it may not be appropriate to use this terminology in a code based on the fluid description. The heavier the ions (note $q_s = e$ in the model and $L_g \propto m_s$), the more significant the escape plume. Recently, the ion escape plume has been observed and verified using MAVEN measurements (*Dong et al.*, 2015d; *Brain et al.*, 2015). *Dong et al.* (2015d) estimated the O^+ escape rate through the polar plume to be $\sim 35\%$ of the tailward escape and $\sim 25\%$ of the total escape for energies > 25 eV.

Figure 6.3 shows the contour plot of the O_2^+ ion speed, $U_{O_2^+}$, on an isosurface of O_2^+ ion density with $n_{O_2^+}$=0.005 cm^{-3}. It is well known that the dayside ion escape plume is a region filling with low-density and high-energy ion fluxes (*Dong et al.*, 2015d). Isosurfaces with other $n_{O_2^+}$ values can show similar structures. However, in order to evince the structure, $n_{O_2^+}$ cannot be too large. In addition, the O^+ and CO_2^+ ions also display similar asymmetric plume-shaped isosurfaces as that of O_2^+ ion. The $U_{O_2^+}-$colored isosurfaces are illustrated for two purposes: **(1)** To show a global picture of the pickup ion acceleration. The color ($U_{O_2^+}$) variation along the isosurface indicates that the ions escaping from the dayside plume can be accelerated to a higher speed (thus energy) than those escaping from the nightside plasma wake region (at a constant altitude). This physical picture is further verified in Figure 6.4, where we plot both O_2^+ ion velocity vector in the $x - z$ plane and its speed along two selected $\mathbf{U}_{O_2^+}$ streamlines. As shown in Figure 6.4 (both the velocity vectors and speed curves), the escaping ion originated from dayside ionosphere can be accelerated to a higher speed (along the solid red streamline located in the escape plume region) than those originated from nightside ionosphere (along the dashed blue streamline located in the nightside plasma wake region). Compared with the pre-ICME phase, the ion acceleration is more significant in the sheath phase (Figure 6.4). **(2)** To

reveal two main ion escape channels: accelerated pickup ion loss through the dayside plume and "cold" ionospheric ion loss through the nightside plasma wake region. The word "cold" in this paper means that the energy is low. Detailed case studies on the response of pickup ions to this ICME event can be found in *Curry et al.* (2015b) using a test-particle code (*Curry et al.*, 2014).

Unlike previous studies (e.g., *Najib et al.*, 2011; *Dong et al.*, 2014), which assumed an idealized solar wind (U_x component only) and IMF (56° Parker spiral), we adopted actual solar wind and IMF measurements from SWIA and MAG. The orientation of the ion escape plume in a multi-fluid MHD code is mainly in the $\mathbf{E} = -\mathbf{u}_+ \times \mathbf{B}$ direction (*Najib et al.*, 2011). In Figure 6.3, the dayside ion escape plume does not always originate from the geographical polar region; therefore, when the term "polar plume" is used, it is specified in the Mars-Sun-Electric field (MSE) coordinate system, where the electric field is always parallel to the z-axis (*Brain et al.*, 2015; *Curry et al.*, 2015b; *Dong et al.*, 2015d). Compared with the pre-ICME phase (Case 1), the density isosurface of O_2^+ ion indicates that the ion escape is greatly enhanced during the ICME sheath phase (Case 3).

We summarize the calculated ion escape rates for all four cases by using a sphere with the radius equal to six Mars radii (r=6R_M) in Table 6.1. Table 6.1 mirrors the enhancement of individual ion escape rates during the ICME event. The O^+, O_2^+ and CO_2^+ ion losses are respectively increased by factors of ~ 3.2, ~ 14.6 and ~ 11.1, which results in an increase in the total ion escape rate by a factor of ~ 11, from 2.05×10^{24} s^{-1} (Case 1, pre-ICME phase) to 2.25×10^{25} s^{-1} (Case 3, sheath phase), during this time period. Figure 6.4 shows the calculated O_2^+ ion number densities in the $x - z$ plane. Inspection of Figure 6.4 reveals that the nightside ion escape is significantly increased in Case 3 compared to Case 1. The large fraction of tailward ion escape fluxes at the ejecta phase (Case 3) is mainly caused by two factors: 1) Compared with the pre-ICME phase (Case 1), the solar wind dynamic

pressure was drastically intensified at the ejecta phase, leading to the largest solar wind proton density in the Martian upper atmosphere and the greatest compression of plasma boundaries (see Figure 6.5). 2) The IMF magnitude is significantly increased at the ejecta phase, thus the characteristic length, $L_g \propto u_{sw}/B$, associated with the asymmetry is decreased (refer to the isosurface shape illustrated in Figure 6.3). We plan to adopt the approach described in *Dong et al.* (2015d) to estimate the ion loss through the dayside escape plume and the nightside plasma wake in a future study.

Brain et al. (2015) estimated a net ion escape rate of $\sim 2.5 \times 10^{24}$ s^{-1} by choosing a spherical shell at ∼1000 km above the planet with energies >25 eV over a four-month MAVEN period. It is interesting to mention that our model calculations for the pre-ICME case (which is close to the nominal solar wind condition) are in reasonable agreement with the ion escape rate estimated from available MAVEN data and previous estimates using the MEX data (*Lundin et al.*, 2013; *Ramstad et al.*, 2015) during this relatively weak solar cycle. The ion escape rates of Case 1 are further investigated by using selected spheres with different radii in order to demonstrate that the calculated ion escape rates do not change to any significant degree once the radius of the sphere exceeds 6 R_M (total ion escape rate, in $\times 10^{24}$ s^{-1}, at a sphere of 3R_M: 2.22, 4R_M: 2.26, 5R_M: 2.12, 6R_M: 2.05, 7R_M: 2.04, 8R_M: 2.05, 9R_M: 2.06, 10R_M: 2.07; not listed in Table 6.1).

6.3.3 Variation of plasma boundaries at the subsolar region

Finally, we plot the pressure balance along the Mars-Sun line on the dayside for three case studies corresponding to three major ICME phases: pre-ICME phase (Case 1), sheath phase (Case 3), and ejecta phase (Case 4). Different pressures (the magnetic pressure, P_b=$B^2/(2\mu_0)$, the dynamic pressure, P_{dyn}=ρv^2, and the thermal pressure, P_{th}=nk_BT) are represented by different curves in the left panels of Figure 6.5. The total thermal pressure, $P_{th(Tot)}$, by definition is the sum of $P_{th(SW)}$ and $P_{th(Iono)}$; the

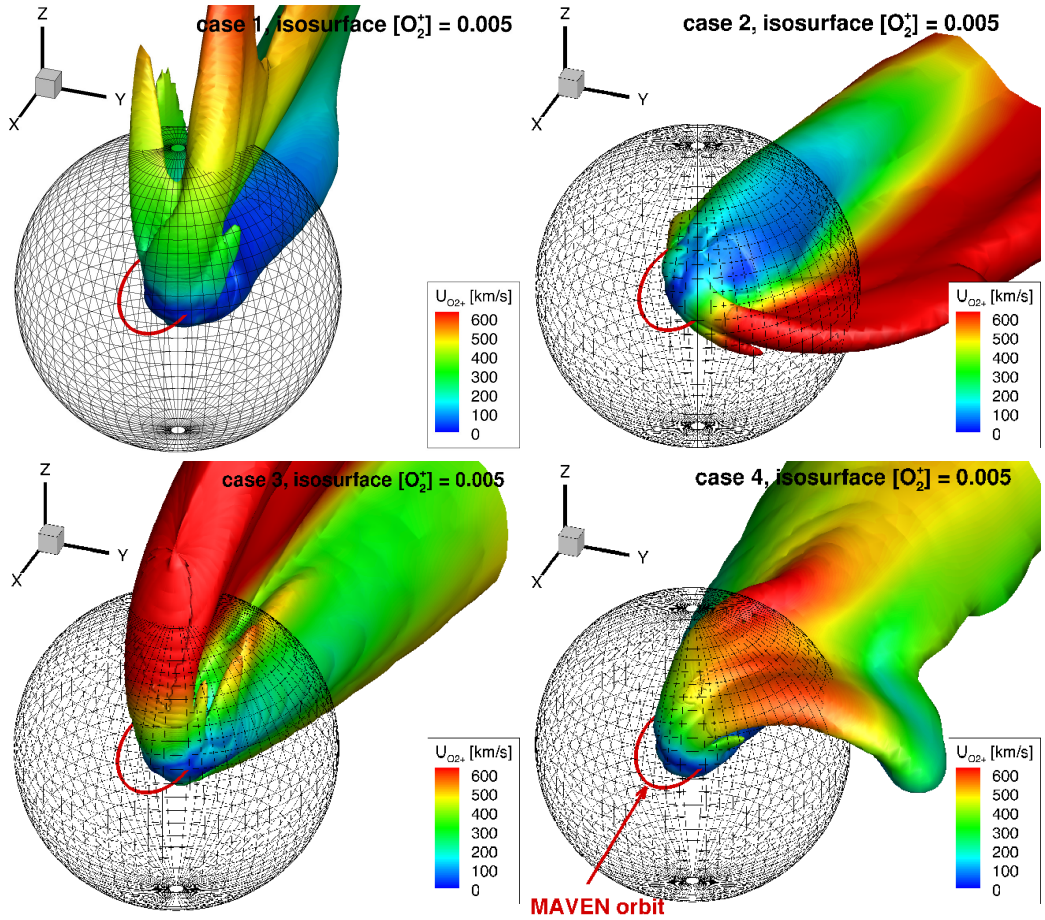

Figure 6.3: The isosurface of O_2^+ ion density with $n_{O_2^+}$=0.005 cm^{-3}, on which the contour of O_2^+ ion speed $U_{O_2^+}$ is presented. The meshed grid is the sphere with r=6R_M used to calculate the ion escape rate. The r=6R_M sphere in each plot is also used as a reference to know the relative size of the isosurface. The red curves are the MAVEN trajectories.

latter peaks in the Martian ionosphere and is contributed by the planetary ions. It is noteworthy that in pre-ICME and sheath phases (Cases 1 and 3), the contribution of $P_{B(Tot)}$ to P_{total} is negligible in the upstream of Martian bow shock. The contribution of $P_{B(Tot)}$ to P_{total} in the ejecta phase (Case 4), however, cannot be ignored because of the strong IMF strength. Different from Case 4, $P_{B(Crustal)}$ increases dramatically near Mars (in Cases 1 and 3) due to the existence of strongly localized crustal magnetic fields, which helps the formation of strongly magnetized regions at Mars (*Riousset et al.*, 2013, 2014).

By adopting the same approach in *Najib et al.* (2011), the intersection of $P_{dyn(SW)}$

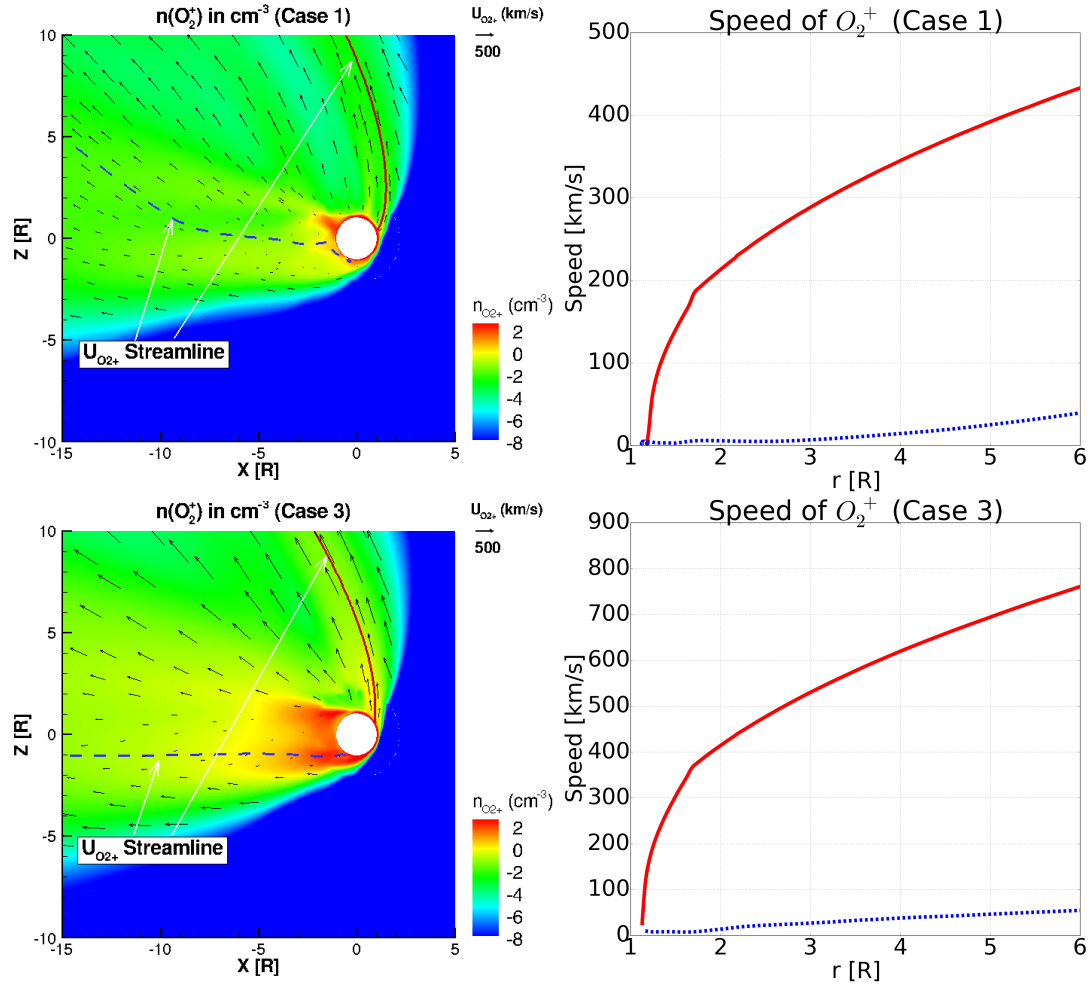

Figure 6.4: (left) The calculated O_2^+ ion number densities in cm^{-3} in the $x-z$ plane in a logarithmic scale (see density colorbar). The black arrow represents the O_2^+ ion velocity vector (a reference vector of 500 km/s magnitude is displayed in the upper right corner). The selected solid red and dashed blue curves in the contour plot are the $\mathbf{U}_{O_2^+}$ streamlines at dayside escape plume and nightside plasma wake region, respectively. (right) The corresponding speed (with same line style) along the streamline.

and $P_{th(Tot)}$ is defined as the bow shock (BS) location, and the intersection of $P_{th(Tot)}$ and $P_{B(Tot)}$ is defined as magnetic pileup boundary (MPB). The BS and MPB positions are indicated by the red arrows in Figure 6.5. The bow shock location moves from x=1.57R_M (Case 1) towards Mars at x=1.47R_M (Case 3) due to the great enhancement of solar wind dynamic pressure. Compared with Case 3, the shock stand off distance, x=1.47R_M, slightly moves away from Mars in Case 4 mainly due to the sharp decrease of the ion density at the ejecta phase. The position of the magnetic

pileup boundary follows a similar trend as that of the bow shock at the subsolar region: it first moves from x_{cut}=1.2R_M (Case 1) to x=1.16R_M (Case 3) and then slightly moves away from Mars and back to x=1.17R_M (Case 4). The pressure balance in Figure 6.5 reveals the plasma boundary variations at the subsolar region during this event, but the behavior of these boundaries at the flanks may be different from those at the subsolar region.

The right panels of Figure 6.5 display the solar wind proton density (in cm^{-3}) at altitude of 800 km for Cases 1, 3, 4. The largest density in the middle panel (Case 3) indicates that the solar wind proton in the ICME late sheath phase can compress the boundaries downward more significantly than the other two cases, consistent with the results shown in Figure 6.4 and Figure 6.5 (left panel).

6.4 Data-model comparison for the second MAVEN Deep Dip campaign

Figures 6.6 and 6.7 present the data-model comparisons between the NGIMS measurements and the MF-MHD simulations (O^+, O_2^+, and CO_2^+ ion densities) for orbits O1069 (DD2) and O1085 (DD2), respectively. Both the inbound and outbound comparisons are displayed. The data-model comparisons are based upon the MF-MHD steady state simulations with the SWIA solar wind inputs and the 3-D M-GITM atmospheric profiles (read one-way coupling approach in Chapter IV). Overall the simulation results are in reasonable agreement with the NGIMS data, especially below altitudes of ∼220 km. Note key areas of disagreement.This disagreement between the model and observation may be caused by: 1) The information of the solar wind velocity vector components, IMF orientation and strength were missing, which leads to a lot of uncertainties on the model inputs for these two runs. 2) Some atmospheric dynamics are missing in the current version of the M-GITM model. At present, M-

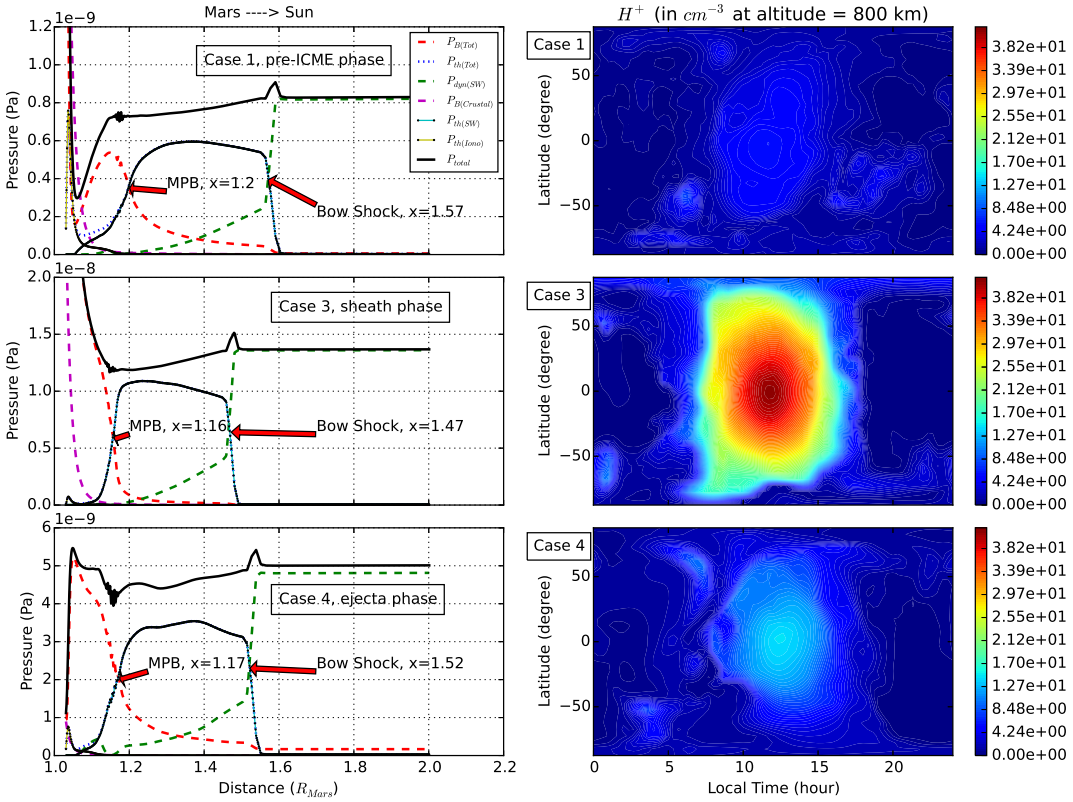

Figure 6.5: Left: Pressure profiles along the Mars-Sun line (see top of the plot) on the dayside for Case 1 (pre-ICME phase), Case 3 (sheath phase), and Case 4 (ejecta phase). Different curves represent different pressures: the total magnetic pressure, $P_{B(Tot)}$ (dashed red), the total thermal pressure, $P_{th(Tot)}$ (dotted blue), the solar wind dynamic pressure, $P_{dyn(SW)}$ (dashed green), the crustal magnetic pressure, $P_{B(Crustal)}$ (dashed magenta), the solar wind thermal pressure, $P_{th(SW)}$ (solid cyan), the ionospheric thermal pressure, $P_{th(Iono)}$ (solid yellow), and the total pressure, P_{total} (solid black). Right: The solar wind proton density profiles (in cm^{-3}) at altitude of 800 km for Cases 1, 3, 4.

GITM does not include the surface topography, thus there are no gravity waves in the model, which has an important effect on the upper atmospheric dynamics/transport due to the gravity wave breaking. 3) We did not include the neutral winds in the MF-MHD calculations.

6.5 More discussion

MAVEN has provided a great opportunity to study the evolution of the Martian atmosphere and climate. A large quantity of useful data has been returned for future studies. These kinds of data-model comparisons can help the community to better understand the Martian upper atmosphere response to the (extreme) variation in the solar wind and its interplanetary environment from a global perspective. Further investigation on this ICME event will be implemented by a real-time study using a well-validated multi-species MHD (MS-MHD) code (*Ma and Nagy*, 2007a; *Ma et al.*, 2014), which is computationally cheaper than the MF-MHD code by ignoring the individual ion dynamics. Although the MS-MHD code cannot reproduce the dayside ion escape plumes, the simulation based upon a real-time study is able to calculate the time-dependent ion escape rates and reveal more details on how boundaries (i.e., bow shock and MPB) vary with time during this event. Further study on the Deep Dip comparisons includes adopting the NGIMS measured neutral atmosphere profiles as the MF-MHD inputs. The neutral atmosphere profiles observed by the NGIMS instrument should include all the necessary atmospheric dynamics and variations, especially above altitudes of $\sim$ 220 km.

6.6 Conclusion

In summary, we studied the solar wind interaction with the Martian upper atmosphere during the March 8th ICME event based on four steady state case studies.

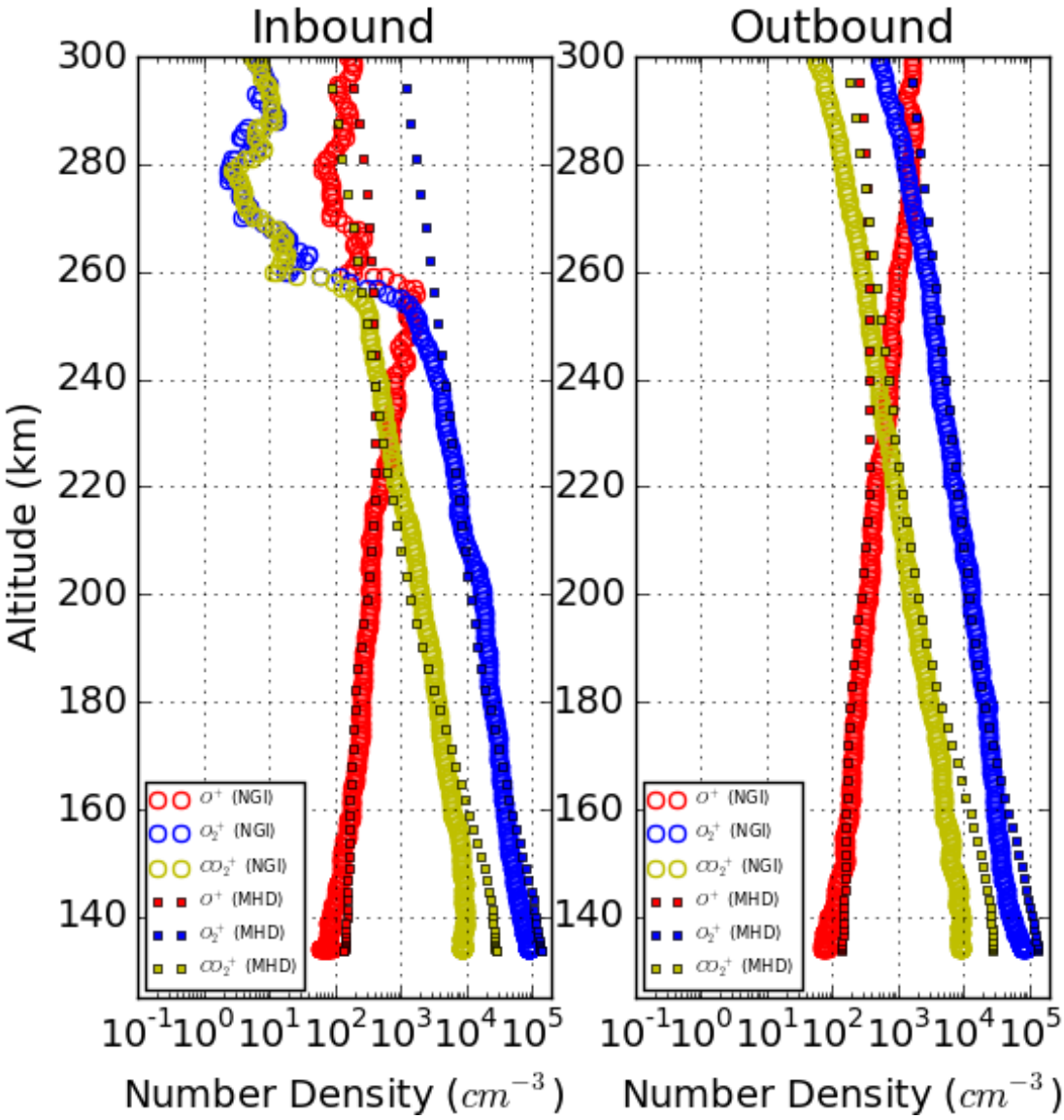

Figure 6.6: Data-model comparison between the NGIMS data and the MF-MHD simulation for orbit 1069 on 19-April-2015. Both the inbound and outbound comparisons are displayed.

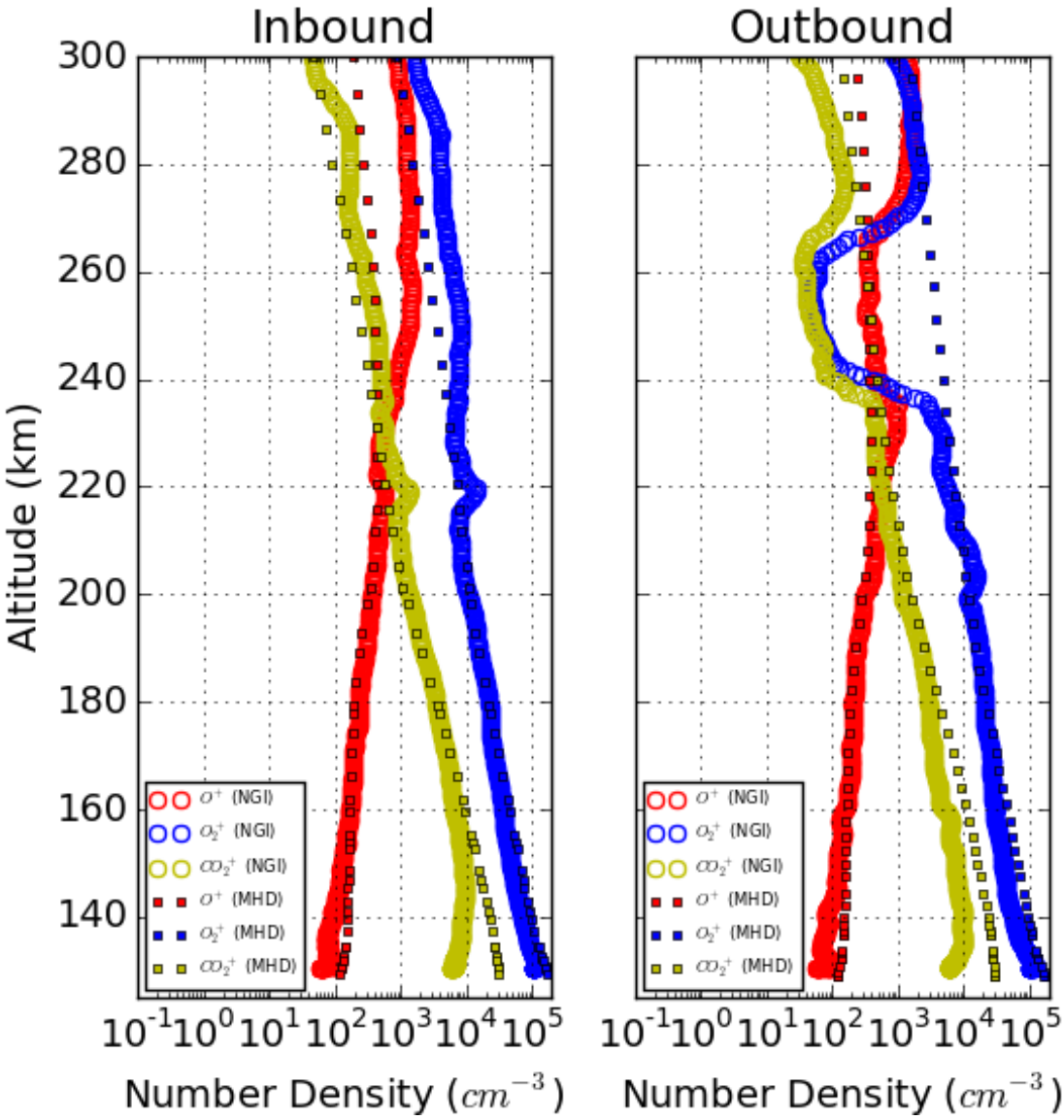

Figure 6.7: Data-model comparison between the NGIMS data and the MF-MHD simulation for orbit 1085 on 22-April-2015. Both the inbound and outbound comparisons are displayed.

These four cases correspond to three major ICME phases: pre-ICME phase (Case 1), sheath phase (Cases 2–3), and ejecta phase (Case 4). Detailed data-model comparisons demonstrate that the simulation results are in good agreement with the MAVEN measurements, indicating that the MF-MHD model can reproduce most of the features observed by MAVEN, thus providing confidence in the estimate of ion escape rates from its calculation. The total ion loss is significantly enhanced by factor of ~ 11, from $\sim 2.05 \times 10^{24}$ s^{-1} (pre-ICME phase) to $\sim 2.25 \times 10^{25}$ s^{-1} (sheath phase), during this time period. The acceleration of O_2^+ ions along the selected day- and nightside ($\mathbf{U}_{O_2^+}$) streamlines demonstrates that the planetary ions escaping from the dayside plume have a higher speed (thus energy) than those escaping from the nightside plasma wake region. Two major ion escape channels are illustrated: accelerated pickup ion loss through the dayside plume and ionospheric ion loss through the nightside plasma wake region.

When solar wind dynamic pressure is increased and the characteristic length (or ion gyroradius in a kinetic description), $L_g \propto u_{sw}/B$, associated with the asymmetry is decreased, the ionospheric ion escaping from the plasma wake is significantly enhanced. Interestingly, by comparing all four simulation results along the same MAVEN orbit, we note that there is no significant variation in the Martian ionosphere (at altitudes $\lesssim 200$ km, i.e., the photochemical region). Finally, both bow shock and magnetic pileup boundary (BS, MPB) locations are decreased from ($1.2\mathrm{R}_M$, $1.57\mathrm{R}_M$) at the pre-ICME phase to ($1.16\mathrm{R}_M$, $1.47\mathrm{R}_M$), respectively, during the sheath phase along the dayside Mars-Sun line.

We also presented a data-model comparison of the Martian ionospheric ion densities between the NGIMS measurements and the MF-MHD simulations during the second MAVEN Deep Dip campaign. Both the inbound and outbound comparisons are displayed. Overall the simulated ion densities reasonably agree with the NGIMS measurements, especially below altitudes of $\sim$220 km where the solar wind-Mars inter-

action does not have a significant effect on the structure of thermosphere/ionosphere.

In Chapter VII (also the last chapter), we will show some preliminary results of the multi-fluid MHD model with separated ion and electron pressure equations. We will also discuss future work that is planned making use of the MF-MHD code in conjunction with MAVEN data analysis activities in the next chapter.

CHAPTER VII

Preliminary results of electron temperature calculation, summary and future work

7.1 Preliminary results from the multi-fluid MHD model with separated ion and electron pressure equations

In this section, we illustrate some very preliminary results from the MF-MHD simulation that includes the electron pressure equation (see Chapter II for the detailed formulation). Figure 7.1 shows the individual ion temperatures, ion temperature and electron temperature. Below certain altitudes ($\sim$ 120 km), all the temperatures have the same value due to the high collision frequency between different particle species. However, the electron temperature deviates from other temperatures and becomes the largest one shortly after it reaches certain altitude. The electron has highest mobility because of its small mass, leading to its highest temperature once electron-ion and electron-neutral collisions are not very frequent. Electrons can gain kinetic energy from the process of photoionization. The ion temperatures become apart from each other at higher altitudes than that of the electrons, which is caused by the ion-ion and ion-neutral collisions.

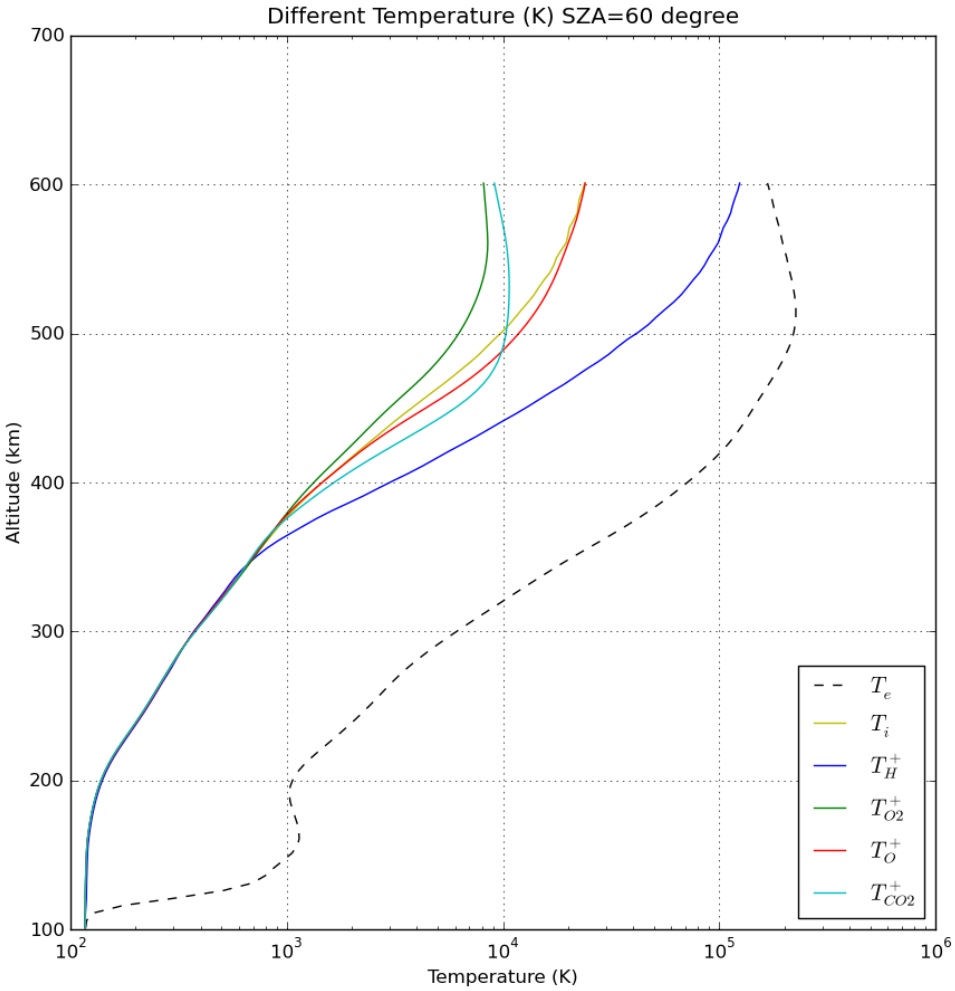

Figure 7.1: The temperatures of individual ion species, total ion and electron.

7.2 Summary: answers to the four main scientific questions

In conclusion, we studied the solar wind interaction with the Martian upper atmosphere at both the current epoch and ancient times. We also investigated the response of Martian upper atmosphere and its space plasma environment to the extreme solar wind conditions (e.g., ICMEs). In Chapter I, we proposed four main scientific questions that are closely related to the primary scientific goals of the MAVEN mission. Now we can answer them one by one:

Question:

1) What are the Martian ion escape rates at the current epoch and ancient times?

Answer:

i) The total ion escape rate is about (1∼10) $\times$ 10^{24} s^{-1} at the current epoch.

ii) The net ion loss at ancient Mars may reach $\sim$ 10^{25} s^{-1} based on the nominal solar wind conditions, which is one order of magnitude larger than the ion loss from the current solar minimum conditions.

Question:

2) What controls the ion escape processes? How are the ion escape variations connected to the solar cycle, crustal field orientation and seasonal variations?

Answer:

i) Different solar cycles can affect the ion loss by a factor of $\sim$ 3.3, while different seasons can vary the ion loss by a factor of $\sim$ 1.3.

ii) The magnetic shielding effect of crustal field are significantly correlated with season, which varies from 1.17 (aphelion) to 1.38 (perihelion) due to the existence of axial tilt (25.2°).

Question:

3) How do the variable 3-D cold neutral thermosphere and hot oxygen corona affect the solar wind-Mars interaction?

Answer:

i) The hot oxygen corona plays an important role in increasing the O^+ ion escape and decreasing the heavy ionospheric ion species (O_2^+ and CO_2^+) loss.

ii) The cold oxygen is the primary neutral source for O^+ ion escape.

Question:

4) How does the Martian atmosphere respond to extreme variations (e.g., ICMEs) in the solar wind and its interplanetary environment.

Answer:

i) The total ion escape rate is increased by an order of magnitude, from 2.05×10^{24} s^{-1} (pre-ICME phase) to 2.25×10^{25} s^{-1} (ICME sheath phase), during the ICME0308 event.

ii) No significant variation is found in the Martian ionosphere at altitudes $\lesssim$ 200 km (photochemical region) during this extreme event.

iii) Both bow shock and magnetic pileup boundary (BS, MPB) locations are decreased from ($1.2R_M$, $1.57R_M$) at the pre-ICME phase to ($1.16R_M$, $1.47R_M$), respectively, during the sheath phase along the dayside Sun-Mars line.

7.3 Future work

On November 18, 2013, NASA launched the Mars Atmosphere and Volatile EvolutioN (MAVEN) spacecraft, and it successfully went into orbit around Mars on September 21, 2014. The MAVEN mission is a NASA Mars Scout mission, selected primarily to determine the importance of the role of escape of volatiles to space on the planet's climatic evolution, i.e., its transition from an environment with sufficient atmospheric pressure and temperatures that liquid water was at least episodically stable, to the low-pressure, cold, arid climate of today. The three primary scientific goals of MAVEN are to 1) determine the structure, composition and dynamics of the Martian upper atmosphere, 2) determine rates of atmospheric escape through various processes at the current epoch and with these answers, 3) estimate the integrated loss

to space that has occurred through Martian history (*Bougher et al.*, 2014; *Lillis et al.*, 2015; *Jakosky et al.*, 2015a). Therefore, MAVEN should be able to determine quantitatively ion escape rates at the current epoch and identify which ion is the dominant escaping species. This knowledge can help to constrain our simulation results and investigate the underlying processes responsible for regulating ion escape rates.

Future work that is planned making use of the MF-MHD code in conjunction with MAVEN data analysis activities includes:

1) As shown by *Brecht and Ledvina* (2014b), the neutral winds can greatly affect the ion escape rate calculations in a global hybrid code. We plan to include the neutral winds from M-GITM in the MF-MHD code to further investigate the ion escape rate and global ionospheric structure. The newly calculated ion escape rate and the ionospheric profile will be used to compare with the current and future MAVEN observations. On the other hand, the disagreement between the MF-MHD ion density calculation and the NGIMS observation, especially above certain altitudes ~ 220 km (Figures 6.6 & 6.7) indicates the necessity to test the actual observed neutral atmosphere profiles in a plasma code.

2) We plan to compare the simulation results from the MF-MHD model with separate electron and ion pressure equations to the Langmuir Probe and Waves (LPW) data (*Ergun et al.*, 2015). The self-consistently calculated charged particle temperatures and densities can also improve the simulation results of M-GITM and M-AMPS. For example, M-AMPS can adopt the ion and electron temperatures and densities from the MF-MHD simulation for its hot coronae calculations.

3) One or two (short) real-time/time-accurate simulations are necessary to study the reversal of the interplanetary magnetic field (e.g., Mars moves across the heliospheric current sheet) and its consequences on the ion escape plume. The study of the ion escape rate variations in a IMF reversal case is crucial because MAVEN has observed a lot of such cases. The effect of IMF reversal on the global ion loss needs

to be interpreted from a global plasma code. The real time study will also allow us to investigate the influence of a IMF reversal on plasma dynamics and magnetic field configurations in the Martian magnetosheath and tail plasma wake region from a global perspective. A large quantity of useful data has been returned from MAVEN for future studies and comparisons to such real-time simulations.

4) The one-way coupling in this thesis is a necessary precursor to future full two-way integration of various models since the two-way integration requires using a combination of both the MF-MHD and M-GITM codes to solve for the overlapping domain (100-220 km). We plan to implement a dynamic two-way coupling between M-GITM and the MF-MHD code in the future. The basic idea to achieve a dynamic two-way coupling in this overlapping (buffer) region is to use M-GITM to solve the ion mass continuity equation and MF-MHD to solve the ion momentum and energy equations, which requires an exchange of fields (i.e., ρ and $\mathbf{u}$) between two models at a certain time frequency. The underlying reasons are that i) M-GITM carries more ion species than the MF-MHD code and has a more detailed ion-neutral chemical scheme; ii) the MF-MHD code self-consistently solves for the time-dependent magnetic field, required when solving for realistic ion velocities. The dynamic two-way coupling has more flexibility to study some extreme events, such as ICMEs/CIRs/SEPs or Martian dust storms. We will also compare the simulation results with both previous calculations from the one-way coupling approach and MAVEN observations, which could help to improve our understanding of the ion escape processes at the current epoch.

BIBLIOGRAPHY

BIBLIOGRAPHY

Acuña, M. H. et al. (1999), Global Distribution of Crustal Magnetization Discovered by the Mars Global Surveyor MAG/ER Experiment, *Science*, *284*, 790–793.

Arkani-Hamed, J. (2001), A 50-degree spherical harmonic model of the magnetic field of Mars, *Journal of Geophysical Research*, *106*, 23,197–23,208.

Barabash, S., A. Fedorov, R. Lundin, and J. A. Sauvaud (2007), Martian atmospheric erosion rates., *Science*, *315*, 501–503.

Bird, G. A., (1994), Molecular Gas Dynamics and the Direct Simulation of Gas Flows, 2nd ed., Clarendon Press, Oxford.

Bollen, J., H. Van de Sompel, A. Hagberg, L. Bettencourt, R. Chute, M. A. Rodriguez, L. Balakireva (2009), Clickstream Data Yields High-Resolution Maps of Science, *PLoS ONE* , *4(3)*, e4803. doi:10.1371/journal.pone.0004803

Bougher, S. W., S. Engel, R. G. Roble, and B. Foster (2000), Comparative terrestrial planet thermospheres 3. Solar cycle variation of global structure and winds at solstices, *Journal of Geophysical Research*, *105*, 17669 –17692.

Bougher, S. W., J. M. Bell, J. R. Murphy, M. A. Lopez-Valverde, and P. G. Withers (2006), Polar warming in the Mars thermosphere: Seasonal variations owing to changing insolation and dust distributions, *Geophysical Research Letters*, *33*, L02,203.

Bougher, S. W., P.-L. Blelly, M. R. Combi, J. L. Fox, I. Mueller-Wodarg, A. Ridley, and R. G. Roble (2008), Neutral Upper Atmosphere and Ionosphere Modeling, *Space Sci. Reviews*, *139*, 107-141.

Bougher, S. W., T. M. McDunn, K. A. Zoldak, and J. M. Forbes (2009), Solar Cycle Variability of Mars Dayside Exospheric Temperatures: Model Evaluation of Underlying Thermal Balances, *Geophysical Research Letters*, *36*, L05201.

Bougher, S.W., T.E. Cravens, J. Grebowsky, and J. Luhmann (2014), The Aeronomy of Mars: Characterization by MAVEN of the Upper Atmosphere Reservoir That Regulates Volatile Escape, *Space Science Reviews*, doi:10.1007/s11214-014-0053-7.

Bougher, S. W., D. J. Pawlowski, J. M. Bell, S. Nelli, T. McDunn, J. R. Murphy, M. Chizek, and A. Ridley (2015a), Mars global ionosphere-thermosphere model (MGITM): Solar cycle, seasonal, and diurnal variations of the Mars upper atmosphere, *J. Geophys. Res. Planets*, *120*, 311–342.

Bougher, S. W., et al., Early MAVEN Deep Dip campaign reveals thermosphere and ionosphere variability, *Science*, doi:10.1126/science.aad0459.

Brain, D.A., F. Bagenal, M. H. Acuña, J. E. P. Connerney (2003). Martian magnetic morphology: Contributions from the solar wind and crust, *Journal of Geophysical Research*, *108*, 1424.

Brain, D., et al. (2010), A comparison of global models for the solar wind interaction with Mars, *Icarus*, *206*, 139–151.

Brain, D., et al. (2012), Comparison of global models for the escape of martian atmospheric plasma, AGU Fall Meeting Abstracts, P13C-1969.

Brain, D.A., J.P. McFadden, J.S. Halekas, J.E.P. Connerney, S.W. Bougher, S. Curry, C.F. Dong, Y. Dong, F. Eparvier, X. Fang, K. Fortier, T. Hara, Y. Harada, B.M. Jakosky, R. Lillis, R. Livi, J.G. Luhmann, Y. Ma, R. Modolo, K. Seki (2015), The Spatial distribution of planetary ion fluxes near Mars Observed by MAVEN, *Geophysical Research Letters*, doi:10.1002/2015GL065293.

Brecht, S. H., and S. A. Ledvina (2012), Control of ion loss from Mars during solar minimum, *Earth, Planets and Space*, *64*, 165–178.

Brecht, S. H., and S. A. Ledvina (2014a), The role of the Martian crustal magnetic fields in controlling ionospheric loss, *Geophysical Research Letters*, *41*, 5340–5346.

Brecht, S. H., and S. A. Ledvina (2014b), Hybrid Particle Code Simulations of Mars: The Role of Assorted Processes in Ionospheric Escape, AGU Fall Meeting Abstracts, P54A-06.

Chamberlin, P. C., T. N. Woods, F. G. Eparvier (2008), Flare Irradiance Spectral Model (FISM): Flare component algorithms and results, *Space Weather*, *6*, S05001.

Connerney, J. E. P., J. Espley, P. Lawton, S. Murphy, J. Odom, R. Oliversen, and D. Sheppard (2014), The MAVEN Magnetic Field Investigation, *Space Science Reviews*, doi:10.1007/s11214-015-0169-4.

Cravens, T. E., T. I. Gombosi, J. Kozyra, And A. F. Nagy (1980), Model Calculations of the Dayside Ionosphere of Venus: Energetics, *Journal of Geophysical Research*, *85*, 7778–7786.

Cravens, T. E., J. U. Kozyra, A. F. Nagy, T. I. Gombosi, and M. Kurtz (1987), Electron impact ionization in the vicinity of comets, *Journal of Geophysical Research*, *92*, 7341–7353.

Curry, S. M., M. W. Liemohn, X.-H. Fang, Y.-J. Ma, J. Espley (2013), The influence of production mechanisms on pick-up ion loss at Mars, *Journal of Geophysical Research*, *118*, 554–569.

Curry, S. M., M. W. Liemohn, X.-H. Fang, Y.-J. Ma, J. Slavin, J. Espley, S. Bougher, and C. F. Dong (2014), Test particle comparison of heavy atomic and molecular ion distributions at Mars, *Journal of Geophysical Research*, *119*, 2328–2344.

Curry, S. M., J. G. Luhmann, Y. Ma, M. W. Liemohn, C. Dong, and T. Hara (2015a), Comparative pick-up ion distributions at Mars and Venus: Consequences for atmospheric deposition and escape, *Planet. Space Sci.*, *115*, 35–47.

Curry, S. M., J. G. Luhmann, Y. J. Ma, C. F. Dong, D. Brain, F. Leblanc, R. Modolo, Y. Dong, J. McFadden, J. Halekas, J.E.P. Connerney, J. Espley, T. Hara, Y. Harada, C. Lee, X. Fang, and B. Jakosky (2015b), Response of Mars O^+ Pick-up Ions to the March 8th, 2015 ICME: Inferences from MAVEN Data-Based Models,, *Geophysical Research Letters*, doi:10.1002/2015GL065304.

de Pater, I., and J. J. Lissauer (2010), Planetary Sciences, 2nd ed., Cambridge Univ. Press, New York, pp 5–6.

Deng, Y., A. D. Richmond, A. J. Ridley, and H.-L. Liu (2008), Assessment of the non-hydrostatic effect on the upper atmosphere using a general circulation model (GCM), *Geophysical Research Letters*, *35*, L01104.

Dong, C. F., M. M. Cowee, and D. Winske (2013), Plasma and wave properties downstream of Martian bow shock: Hybrid simulations, Report No. LA-UR 13-29060, Los Alamos National Laboratory.

Dong, C. F., S. W. Bougher, Y. Ma, G. Toth, A. F. Nagy, and D. Najib (2014), Solar wind interaction with Mars upper atmosphere: Results from the one-way coupling between the multifluid MHD model and the MTGCM model, *Geophysical Research Letters*, *41*, 2708–2715.

Dong,C. F., S. W. Bougher, Y. J. Ma, G. Toth, Y. Lee, A. F. Nagy, V. Tenishev, D. J. Pawlowski, M. R. Combi, and D. Najib (2015a), Solar wind interaction with the Martian upper atmosphere: variable 3-D cold neutral thermosphere and hot oxygen corona, *J. Geophys. Res. Space Physics*, *120*, 7857–7872, doi:10.1002/2015JA020990.

Dong, C. F., S. W. Bougher, Y. Ma, G. Toth, Y. Lee, A. F. Nagy, V. Tenishev, D. J. Pawlowski, M. R. Combi, and D. Najib (2015b), Solar wind interaction with the Martian upper atmosphere: Crustal field orientation, solar cycle and seasonal variations, *J. Geophys. Res. Space Physics*, *120*, doi:10.1002/2015JA020990.

Dong, C. F., Y. J. Ma, S. W. Bougher, G. Toth, A. F. Nagy, J. S. Halekas, Y. X. Dong, S. M. Curry, J. G. Luhmann, D. Brain, J. E. P. Connerney, J. Espley, P. Mahaffy, M. Benna, J. P. McFadden, D. L. Mitchell, G. A. DiBraccio, R. J. Lillis,

B. M. Jakosky, and J. M. Grebowsky (2015c), Multi-fluid MHD study of the solar wind interaction with Mars' upper atmosphere during the 2015 March 8 ICME event, *Geophys. Res. Lett.*, doi:10.1002/2015GL065944.

Dong, Y., X. Fang, D. A. Brain, J. P. McFadden, J. S. Halekas, J. E. Connerney, S. M. Curry, Y. Harada, J. G. Luhmann, B. M. Jakosky (2015d), Strong plume fluxes at Mars observed by MAVEN: An important planetary ion escape channel, *Geophysical Research Letters*, doi:10.1002/2015GL065346.

Dubinin, E., M. Fraenz, A. Fedorov, R. Lundin, N. Edberg, F. Duru, O. Vaisberg (2011), Ion Energization and Escape on Mars and Venus, *Space Science Reviews*, *162*, 173 – 211.

Ergun, R., et al. (2015), Dayside electron temperature and density profiles at Mars: First results from the MAVEN Langmuir probe and waves instrument, *Geophys. Res. Lett.*, doi:10.1002/2015GL065280.

Fang, X., M. W. Liemohn, A. F. Nagy, J. G. Luhmann, and Y. J. Ma (2010), On the effect of the martian crustal magnetic field on atmospheric erosion, *Icarus*, *206*, 130–138.

Fang, X., S. W. Bougher, R. E. Johnson, J. G. Luhmann, Y. J. Ma, Y.-C. Wang, M. W. Liemohn (2013), The importance of pickup oxygen ion precipitation to the Mars upper atmosphere under extreme solar wind conditions, *Geophys. Res. Lett.*, *40*, 1922–1927.

Feldman, P. D., A. J. Steffl, J. Wm. Parker, M. F. A'Hearn, J.-L. Bertaux, S. A. Stern, H. A. Weaver, D. C. Slater, M. Versteeg, H. B. Throop, N. J. Cunningham, L. M. Feaga (2011), Rosetta-Alice observations of exospheric hydrogen and oxygen on Mars, *Icarus*, *214*, 394–399.

Fillingim, M. O., L. M. Peticolas, R. J. Lillis, D. A. Brain, J. S. Halekas, D. L. Mitchell, R. P. Lin, D. Lummerzheim, S. W. Bougher, and D. L. Kirchner (2007), Model calculations of electron precipitation induced ionization patches on the nightside of Mars, *Geophysical Research Letters*, *34*, L12101.

Fillingim, M. O., L. M. Peticolas, R. J. Lillis, D. A. Brain, J. S. Halekas, D. Lummerzheim, and S. W. Bougher (2010), Localized ionization patches in the nighttime ionosphere of Mars and their electrodynamic consequences, *Icarus*, *206*, 112–119.

Gary, S. P. (2005), Theory of Space Plasma Microinstabilities, Cambridge University Press, Cambridge, UK.

Glocer, A., G. Tóth, Y. J. Ma, T. I. Gombosi, J. C. Zhang, and L. M. Kistler (2009), Multifluid Block-Adaptive-Tree Solar Wind Roe-Type Upwind Scheme: Magnetospheric composition and dynamics during geomagnetic storms–Initial results, *J. Geophys. Res.*, *114*, A12203.

Gombosi, T. I. (1994), Gaskinetic Theory, Cambridge University Press, Cambridge, UK.

Haberle, R. M., M. M. Joshi, J. R. Murphy, J. R. Barnes, J. T. Schofield, G. Wilson, M. Lopez-Valverde, J. L. Hollingsworth, A. F. C. Bridger, and J. Schaeffer (1999), General circulation model simulations of the Mars Pathfinder atmospheric structure investigation/meteorology data, *Journal of Geophysical Research*, *104*, 8957–8974.

Halekas, J. S., E. R. Taylor, G. Dalton, G. Johnson, D. W. Curtis, J. P. McFadden, D. L. Mitchell, R. P. Lin, B. M. Jakosky (2015), The Solar Wind Ion Analyzer for MAVEN, *Space Science Reviews*, doi:10.1007/s11214-013-0029-z.

Hanson, W. B., S. Sanatini, and D. R. Zuccaro (1977), The Martian ionosphere as observed by the Viking retarding potential analyzer, *J. Geophys. Res.*, *82*, 4351–4363.

Harnett, E. M., and R. M. Winglee (2003), The influence of a mini-magnetopause on the magnetic pileup boundary at Mars, *Geophys. Res. Lett.*, *30*, 10-1, doi:10.1029/2003GL017852.

Harnett, E. M., and R. M. Winglee (2006), Three-dimensional multifluid simulations of ionospheric loss at Mars from nominal solar wind conditions to magnetic cloud events, *J. Geophys. Res.*, *111*, A09213.

Jakosky, B. M. et al. (2015a), The Mars Atmosphere and Volatile Evolution (MAVEN) Mission, *Space Science Reviews*, doi:10.1007/s11214-015-0139-x.

Jakosky, B. M. et al. (2015b), MAVEN Observations of the Response of Mars to an Interplanetary Coronal Mass Ejection, *Science*, doi:doi:10.1126/science.aad0210.

Johnson, R. E., J. G. Luhmann (1998), Sputter contribution to the atmospheric corona on Mars, *J. Geophys. Res.*, *103*, 3649-3653.

Kharchenko, V., A. Dalgarno, B. Zygelman, and J. H. Yee (2000), Energy transfer in collisions of oxygen atoms in the terrestrial atmosphere, *J. Geophys. Res.*, *103*, 24,899–24,906.

Kim, J., A. F. Nagy, J. L. Fox, and T. E. Cravens (1998), Solar cycle variability of hot oxygen atoms at Mars, *J. Geophys. Res.*, *103*, 29, 339.

Lapenta, G. (2012), Particle simulations of space weather, *Journal of Computational Physics*, *231*, 795–821.

Larson, D.E., Lillis, R.J., Hatch, K., Robinson, M., Glaser, D., Chen, J., Curtis, D.W., Tiu, C., Lin, R.P., Luhmann, J.G., Jakosky, B.M. (2015), The MAVEN Solar Energetic Particle Investigation, *Space Sciences Reviews*, doi:10.1007/s11214-015-0165-8.

Lee, Y., M. R. Combi, V. Tenishev and S. W. Bougher (2013), Hot Oxygen Corona in Mars' Upper Thermosphere and Exosphere: A Comparison of Results using the MGITM and MTGCM, AGU Fall Meeting Abstracts, P21A-1703.

Lee, Y., M. R. Combi, V. Tenishev and S. W. Bougher (2014a), Hot carbon corona in Mars' upper thermosphere and exosphere: 1. Mechanisms and structure of the hot corona for low solar activity at equinox, *Journal of Geophysical Research*, *119*, 905–924.

Lee, Y., M. R. Combi, V. Tenishev and S. W. Bougher (2014b), Hot Carbon Corona in Mars' Upper Thermosphere and Exosphere: 2. Solar Cycle and Seasonal Variability, *Journal of Geophysical Research*, doi:10.1002/2014JE004669.

Lee, Y., M. R. Combi, V. Tenishev, S. W. Bougher, C. F. Dong, and D. Pawlowski (2014c), The Martian Hot Oxygen Corona at Ancient times, Abstract P51G-06, 2014 Fall Meeting, AGU, San Francisco, Calif., 15-19 Dec.

Lee, Y., M. R. Combi, V. Tenishev, S. W. Bougher, and R. J. Lillis (2015), Hot Oxygen Corona at Mars and the Photochemical Escape of Oxygen - Improved Description of the Thermosphere, Ionosphere and Exosphere, *JGR-planets*, doi: 10.1002/2015JE004890.

Lillis, R.J., D.A. Brain, S.W. Bougher, F. Leblanc, J.G. Luhmann, B.M. Jakosky, R. Modolo, J. Fox, J. Deighan, X. Fang, Y.C. Wang, Y. Lee, C. Dong, Y. Ma, T. Cravens, L. Andersson, S.M. Curry, N. Schneider, M. Combi, I. Stewart, J. Clarke, J. Grebowsky, D. L. Mitchell, R. Yelle, A.F. Nagy, D. Baker, and R. P. Lin (2015), Characterizing atmospheric escape from Mars today and through time, with MAVEN, *Space Science Reviews*.

Liu, Y., A. F. Nagy, C. P. T. Groth, D. L. DeZeeuw, T. I. Gombosi, and K. G. Powell (1999), 3D multi-fluid MHD studies of the solar wind interaction with Mars, *Geophys. Res. Lett.*, *26*, 2689–2692, doi:10.1029/1999GL900584.

Liu, Y., A. F. Nagy, T. I. Gombosi, D. L. Dezeeuw, and K. G. Powell (2001), The solar wind interaction with Mars: results of three-dimensional three-species MHD studies, *Advances in Space Research*, *27*, 1837–1846, doi:10.1016/S0273-1177(01) 00301-5.

Luhmann, J. G. (1991), Induced Magnetic Fields At The Surface Of Venus Inferred From Pioneer Venus Orbiter Near-Periapsis Measurements, *Journal of Geophysical Research*, *96*,18,831–18,840.

Luhmann, J. G., W. T. Kasprzak, and C. T. Russell (2007), Space weather at Venus and its potential consequences for atmosphere evolution, *Journal of Geophysical Research*, *112*, E04S10.

Luhmann, J.G., C.F. Dong, Y.J. Ma, S.M. Curry, D. Mitchell, J. Espley, J. Connerney, J. Halekas, D.A. Brain, S.W. Bougher, B.M. Jakosky, J.M. Grebowsky (2015),

Implications of MAVEN Mars Near-Wake Measurements and Models, *Geophysical Research Letters*, doi:10.1002/2015GL066122.

Lundin, R., S. Barabash, M. Holmström, H. Nilsson, M. Yamauchi, M. Fraenz, and E. M. Dubinin (2008), A comet-like escape of ionospheric plasma from Mars, *Geophysical Research Letters*, *35*, L18,203.

Lundin, R., S. Barabash, M. Holmström, H. Nilsson, M. Yamauchi, E. M. Dubinin, and M. Fraenz (2009), Atmospheric origin of cold ion escape from Mars, *Geophysical Research Letters*, *36*, L17202.

Lundin, R., S. Barabash, M. Yamauchi, H. Nilsson, and D. Brain (2011), On the relation between plasma escape and the Martian crustal magnetic field, *Geophysical Research Letters*, *38*, L02102.

Lundin, R., S. Barabash, M. Holmström, H. Nilsson, Y. Futaana, R. Ramstad, M. Yamauchi, E. M. Dubinin, and M. Fraenz, (2013), Solar cycle effects on the ion escape from Mars, *Geophysical Research Letters*, *40*, 6028–6032.

Ma, Y., A. F. Nagy, K. C. Hansen, D. L. De Zeeuw, T. I. Gombosi, and K. Powell (2002), Three-dimensional multispecies MHD studies of the solar wind interaction with Mars in the presence of crustal fields, *J. Geophys. Res.*, *107* (A10), 1282, doi:10.1029/2002JA009293.

Ma, Y. J., A. F. Nagy, I. V. Sokolov, and K. C. Hansen (2004), Three-dimensional, multispecies, high spatial resolution MHD studies of the solar wind interaction with Mars, *Journal of Geophysical Research*, *109*, A07,211.

Ma, Y. J., and A. F. Nagy (2007a), Ion escape fluxes from Mars, *Geophysical Research Letters*, *34*, L08,201.

Ma, Y. J., A. F. Nagy, G. Tóth, T. E. Cravens, C. T. Russell, T. I. Gombosi, J.-E. Wahlund, F. J. Crary, A. J. Coates, C. L. Bertucci and F. M. Neubauer (2007b), 3D global multi-species Hall-MHD simulation of the Cassini T9 flyby, *Geophys. Res. Lett.*, *34*, L24S10.

Ma, Y. J., X. Fang, C. T. Russell, A. F. Nagy, G. Toth, J. G. Luhmann, D. A. Brain, and C. Dong (2014), Effects of crustal field rotation on the solar wind plasma interaction with Mars, *Geophysical Research Letters*, *41*, doi:10.1002/2014GL060785.

Ma Y. J., C. T. Russell, X. Fang, Y. Dong, A. F. Nagy, G. Tóth, J. S. Halekas, J. E. P. Connerney, J. R. Espley, P. R. Mahaffy, M. Benna, J. McFadden, D. L. Mitchell, and B. M. Jakosky (2015), MHD model results of solar wind interaction with Mars and comparison with MAVEN plasma observations, *Geophysical Research Letters*, doi:10.1002/2015GL065218.

Mahaffy P. R. et al. (2014), The Neutral Gas and Ion Mass Spectrometer on the Mars Atmosphere and Volatile Evolution Mission, *Space Science Reviews*, doi:10.1007/s11214-014-0091-1.

Mahaffy P. R., M. Benna, M. Elrod, R.V. Yelle, S.W. Bougher, S.W. Stone and B.M. Jakosky (2015), Structure and composition of the neutral upper atmosphere of Mars from the MAVEN NGIMS investigation, *Geophys. Res. Lett.*, doi:10.1002/2015GL065329.

McClintock, W. E., N. M. Schneider, G. M. Holsclaw, J. T. Clarke, A. C. Hoskins, I. Stewart, F. Montmessin, R. V. Yelle, J. Deighan, The Imaging Ultraviolet Spectrograph (IUVS) for the MAVEN Mission, *Space Science Reviews*, doi: 10.1007/s11214-014-0098-7.

McDunn, T. L., S. W. Bougher, J. Murphy, M. D. Smith, F. Forget, J.-L. Bertaux, and F. Montmessin (2010), Simulating the density and thermal structure of the middle atmosphere (80-130 km) of Mars using the MGCM-MTGCM: A comparison with MEX/SPICAM observations, *Icarus*, *206*, 5–17.

McFadden, J., Kortmann, O., G. Dalton, G.J., R. Abiad, D. Curtis, R. Sterling, K. Hatch, P. Berg, C. Tiu, M. Marckwordt, R. Lin, and B. Jakosky (2014), The MAVEN Suprathermal and thermal Ion Composition (STATIC) Instrument, *Space Sci. Rev.*

Meng, X., G. Tóth, A. Glocer, M.-C. Fok, and T.I. Gombosi (2013), Pressure anisotropy in global magnetospheric simulations: coupling with ring current models, *J. Geophys. Res.*, *118* 5639–5658.

Mitchell, D. L., C. Mazelle, J.A. Sauvaud, D. Toublanc, Thocaven, Rouzaud, A. Federov, E.R. Taylor, M. Robinson, P. Turin, and D.W. Curtis (2015), The MAVEN Solar Wind Electron Analyzer (SWEA), *Space Science Reviews*, submitted.

Modolo, R., G. M. Chanteur, E. Dubinin, and A. P. Matthews (2006), Simulated solar wind plasma interaction with the Martian exosphere: influence of the solar EUV flux on the bow shock and the magnetic pile-up boundary, *Annales Geophysicae*, *24*, 3403–3410.

Modolo, R., G. M. Chanteur, and E. Dubinin (2012), Dynamic Martian magnetosphere: Transient twist induced by a rotation of the IMF, *Geophys. Res. Lett.*, *39*, L01106.

Nagy, A.F., D. Winterhalter, K. Sauer, T.E. Cravens, S. Brecht, C. Mazelle, D. Crider, E. Kallio, A. Zakharov, E. Dubinin, M. Verigin, G. Kotova, W.I. Axford, C. Bertucci, J.G. Trotignon (2004), The plasma Environment of Mars, *Space Science Reviews*, *111*, 33–114.

Najib, D., A. F. Nagy, G. Tóth, and Y. J. Ma (2011), Three-dimensional, multifluid, high spatial resolution MHD model studies of the solar wind interaction with Mars, *Journal of Geophysical Research*, *116*, A05,204.

Nilsson, H., N. J. Edberg, G. Stenberg, S. Barabash, M. Holmström, Y. Futaana, R. Lundin, and A. Fedorov (2011), Heavy ion escape from Mars, influence from solar wind conditions and crustal magnetic fields, *Icarus*, *215*, 475–484.

Ohia, O., J. Egedal, V. S. Lukin, W. Daughton, and A. Le (2012), Demonstration of Anisotropic Fluid Closure Capturing the Kinetic Structure of Magnetic Reconnection, *Phys. Rev. Lett.*, *109*, 115004.

Powell, K. G., P. L. Roe, T. J. Linde, T. I. Gombosi, and D. L. De Zeeuw (1999), A Solution-Adaptive Upwind Scheme for Ideal Magnetohydrodynamics, *J. Computational Phys.*, *154*, 284-309.

Ramstad, R., S. Barabash, Y. Futaana, H. Nilsson, X.-D. Wang, M. Holmström (2015), The Martian atmospheric ion escape rate dependence on solar wind and solar EUV conditions I: Seven years of Mars Express observations, *Journal of Geophysical Research*, doi:10.1002/2015JE004816.

Ridley, A., Y. Deng, and G. Toth (2006), The global ionosphere-thermosphere model, *J. Atmos. Sol-Terr. Phys.*, *68*, 839.

Riousset, J. A., C. S. Paty, R. J. Lillis, M. O. Fillingim, S. L. England, P. G. Withers, and J. P. M. Hale (2013), Three-dimensional multifluid modeling of atmospheric electrodynamics in Mars' dynamo region, *Journal of Geophysical Research*, *118*, 1–13.

Riousset, J. A., C. S. Paty, R. J. Lillis, M. O. Fillingim, S. L. England, P. G. Withers, and J. P. M. Hale (2014), Electrodynamics of the Martian dynamo region near magnetic cusps and loops, *Geophysical Research Letters*, *41*, 1119–1125.

Rubin, M., , et al. (2014), Plasma environment of a weak comet - Predictions for Comet 67P/Churyumov-Gerasimenko from multifluid-MHD and Hybrid models, *Icarus*, *242*, 38–49.

Schunk, R. W., and A. F. Nagy (2009), Ionospheres, 2nd ed., Cambridge Univ. Press, New York.

Shinagawa, H., and S. W. Bougher (1999), A two-dimensional MHD model of the solar wind interaction with Mars, *Earth, Planets, and Space*, *51*, 55–60.

Smith, M. D. (2004), Interannual variability in TES atmospheric observations of Mars during 1999-2003, *Icarus*, *167*, 148–165.

Stockem, A., I. Lerche, and R. Schlickeiser (2006), On the physical realization of two-dimensional turbulence fields in magnetized interplanetary plasmas, *ApJ*, *651*, 584–589.

Tenishev, V., and M. Combi (2008), A global kinetic model for cometary comae: The evolution of the coma of the Rosetta target comet Churyumov-Gerasimenko throughout the mission, *ApJ*, *685*, 659–677.

Terada, N., H. Shinagawa, T. Tanaka, K. Murawski, and K. Terada (2009), A three-dimensional, multispecies, comprehensive MHD model of the solar wind interaction with the planet Venus, *Journal of Geophysical Research*, *114*, A09208. doi:10.1029/2008JA013937

Tóth, G. et al. (2012), Adaptive Numerical Algorithms in Space Weather Modeling, *J. Computational Phys.*, *231*, 870–903.

Valeille, A., V. Tenishev, S. W. Bougher, M. R. Combi, and A. F. Nagy (2009), Three-dimensional study of Mars upper thermosphere/ionosphere and hot oxygen corona: 1. General description and results at equinox for solar low conditions, *Journal of Geophysical Research*, *114*, E11005.

Valeille, A., S. W. Bougher, V. Tenishev, M. R. Combi, A. F. Nagy (2010), Water loss and evolution of the upper atmosphere and exosphere over martian history, *Icarus*, *206* 28–39.

Valentini, F., P. Trávnicek, F. Califano, P. Hellinger, A. Mangeney (2007), A hybrid-Vlasov model based on the current advance method for the simulation of collisionless magnetized plasma, *Journal of Computational Physics*, *225*, 753–770.

Verigin, M. et al. (1991), Ions of planetary origin in the Martian magnetosphere (Phobos 2/TAUS experiment), *Planetary and Space Science*, *39*, 131–137.

Wang, C.-P., (2008), Penetration of the plasma sheet into the ring current region during a magnetic storm, Themis Science Nuggets.

Winske, D., and N. Omidi (1993), Hybrid codes: Methods and applications, in Computer Space Plasma Physics: Simulation Techniques and Software, edited by H. Matsumoto, and Y. Omura, pp. 103–160, Terra Sci., Tokyo.

Winske, D., L. Yin, N. Omidi, H. Karimabadi, and K. B. Quest (2003), Hybrid simulation codes: Past, present and future - A tutorial, in Space Plasma Simulation, edited by J. Buechener, C. T. Dum, and M. Scholer, pp. 140–169, Springer, Germany.

Zhang, T. L. et al. (2012), Magnetic reconnection in the near Venusian magnetotail, *Science*, *336*, 567.